Characteristics of the Ross and Southern McMurdo Ice Shelves as revealed from Ground-based Radar Surveys

A thesis

submitted in partial fulfilment

of the requirements for the Degree

of

Master of Science

in Environmental Science

by

Michelle R. Ryan

Gateway Antarctica

University of Canterbury

2016

ABSTRACT

Ice shelves are an important component of the Antarctic Ice Sheet as they indirectly control sea level rise by regulating mass flux into the ocean. The coupling of ice shelves with the ocean and the atmosphere makes them vulnerable to climate change. With the oceans absorbing most of the energy from global warming, there is an increased interest in understanding ice-ocean interactions. Basal processes are poorly understood as the base of an ice shelf is difficult to measure due to its inaccessibility.

This thesis explores the effect different internal and basal processes have on ice shelves, and their implications for ice shelf stability, using ground penetrating radar (GPR) and a new phase sensitive radar (ApRES). To achieve this, two study sites were visited. A GPR survey was made on the northern grounding line of the stationary Southern McMurdo Ice Shelf (SMIS) in November 2014 to examine deformation of internal layers, measure ice thickness distribution across a grounding zone, and interpret basal topography. In November 2015, 21 sites in the central Ross Ice Shelf (RIS) were measured with ApRES to estimate the distribution and thickness of marine ice, vertical strain and basal melting/freezing.

Ice thickness of the northern SMIS grounding zone is mapped to high resolution and with an uncertainty of <10 m. Ice is thickest near the grounding line (≈250 m) and thins to 200 m within 3 km seaward of the coast. Basal topography and deformation of internal layers reveal basal processes and interactions of the ice shelf with the ocean. Basal crevasses at the grounding line complicate the radar profile and are created as a result of tidal rather than shear stresses. Downwarping and truncation of internal layers just seaward of the grounding line are caused by basal melting. The generated meltwater directly influences basal topography creating stepped features in the ice shelf base which persist for kilometres from the grounding line.

Widespread marine ice at the base of the RIS is revealed by ApRES point measurements. Marine ice thickness could not be estimated due to possible shortcomings in the hydrostatic equilibrium assumption which produces thickness anomalies in the order of 20 m. This indicates that the marine ice layer has a similar thickness to this uncertainty. In this environment it was found that, calculations of vertical strain and basal melting/freezing

made by examining the difference between internal layers with ApRES requires longer than two weeks between repeat visits to measure with sufficient accuracy.

Stationary ice shelves are an ideal location to examine grounding line processes. The ice remains in-situ for sufficient time to deform in response to its extended interaction with these processes. The grounding line of the SMIS has been stable for a long time and is not inherently vulnerable to future warming as it lies on a prograde bed slope. Additionally, the SMIS is buffered from changes in ocean circulation due to its geographical isolation. Despite this, because the SMIS is effectively stationary, any changes at the ice shelf base may lead to thinning at the grounding line or a modification in velocity as ice is limited in its ability to recover.

The relationship between the presence of marine ice and meteoric ice thickness suggests that the distribution of marine ice is primarily controlled by basal topography rather than ocean circulation. Marine ice alters the ice-ocean interaction, and as a result, the RIS will demonstrate a unique response to climate change. The RIS requires further dedicated study in order to examine its stability, and the distribution and thickness of marine ice will play an important role in the initial response it demonstrates to oceanic changes.

This study demonstrates the potential of a phase sensitive and ground penetrating radar to improve knowledge about ice shelf processes. In particular, their ability to reveal complex internal layering and collect high-precision measurements at the ice-ocean interface.

ACKNOWLEDGEMENTS

This thesis has been a part of a long journey at the University of Canterbury and I would like to thank the people that have made this possible and supported me along the way. Firstly I would like to thank my three supervisors: Wolfgang Rack, Heather Purdie, and Oliver Marsh. They have provided so much support and feedback along the way, as well as giving me pushes of encouragement when I needed it the most.

I would also like to acknowledge the people who have assisted in other ways. Firstly, I would like to acknowledge the help of Kurt Joy, whose technical advice prevented me from throwing my computer out the window in frustration with ArcGIS multiple time, and his feedback has greatly improved the quality of my writing. I would also like to thank Nick Key and Justin Harrison from the geography department. Their technical advice and help with field equipment has been invaluable and many things could have wrong without it. The deployment and processing of the phase sensitive radar would not have been possible without the help from Keith Nicholls and Craig Stewart at the British Antarctic Survey. Without their technical advice, MATLAB codes, and help with understanding/interpreting the data this part of my thesis would not have been possible. The help I received in the field from Daniel Price, Christian Wild, Christina Hulbe, Greg Leonard, Marcus Arnold, Ethan Dale and the rest of the K061-15/16 team must also be acknowledged. This group not only helped with data collection, but also provided quality entertainment and conversation in the middle of the ice shelf.

My fieldwork would not have been possible without funding from the New Zealand Antarctic Research Institute and the logistical and technical support from Antarctica NZ. I would not have been able to complete my masters without the financial support provided by the Sir Neil Isaac scholarship from The Isaac Conservation and Wildlife Trust.

I am going to miss the staff and students at Gateway Antarctica. Extra thanks needs to go to my fellow ‘ice nerds’ for our weekly research discussions, many problems were resolved during these meetings and it was always great to have a fresh pair of eyes.

This thesis would not have been possible without the support from my family and friends. They kept me going with their encouragement, and helped keep me sane. A final mention needs to go to my partner Gavin. His patience and support has been invaluable, and his proofreading abilities helped me correct many errors I would have otherwise missed.

TABLE OF CONTENTS

LIST OF FIGURES

LIST OF TABLES

LIST OF ABBREVIATIONS

AIS	Amery Ice Shelf
ApRES	Autonomous phase-sensitive Radio Echo Sounding
BAS	British Antarctic Survey
DVL	Digital Video Logger
EAIS	East Antarctic Ice Sheet
EM	Electromagnetic
ERS	European Remote Sensing
FFT	Fast Fourier Transform
GL	Grounding Line
GPR	Ground Penetrating Radar
GPS	Global Positioning System
GZ	Grounding Zone
HSSW	High Salinity Shelf Water
IDW	Inverse Distance Weighting
IGY	International Geophysical Year
InSAR	Interferometric synthetic aperture radar
ISW	Ice Shelf Water
LSSW	Low Salinity Shelf Water
MEaSUREs	Making Earth System Data Records for Use in Research Environments
MIS	McMurdo Ice Shelf
MDOT	Mean Dynamic Ocean Topography
pRES	phase-sensitive Radio Echo Sounding
RIGGS	Ross Ice Shelf Geophysical and Glaciological Survey
RIS	Ross Ice Shelf
RISP	Ross Ice Shelf Project
SMIS	Southern McMurdo Ice Shelf
SNR	Signal to Noise Ratio
SPOT	South Pole Overland Traverse
TWT	Two-way-travel time
WAIS	West Antarctic Ice Sheet
w.e.	Water equivalent

1 INTRODUCTION

Ice shelves are the floating extension of the Antarctic ice sheet. They are formed when grounded ice flows into the ocean and begins to float, and they move out to sea under their own weight, spreading and thinning to fill embayments. Ice shelves fringe 61% (Bindschadler et al., 2011) of the coastline of Antarctica, with a total area of 1,541,700 km² (11% of the total Antarctic ice sheet area). Ice shelves are an important interface between the Antarctic ice sheet and the Southern Ocean with 80% of all ice passing through an ice shelf before it is lost through melting and calving (Jacobs et al., 1992). Ice shelves are the most vulnerable part of the Antarctic ice sheet as they are in direct contact with both the atmosphere and the ocean. Not only are they threatened by a warming atmosphere, but also a warming ocean. These two processes are themselves intricately linked as oceans absorb 90% of the heat released to the atmosphere (IPCC, 2013).

Within a few ice thicknesses from the grounding line, an ice shelf is in hydrostatic equilibrium (Fricker & Padman, 2006). This is when the gravity force is balanced by the upwards buoyancy force. Similarly to an ice cube in a glass of water, melting of ice shelves does not directly contribute to sea level rise, however, any changes can have major implications for sea level. Ice shelves provide a buttressing force onto the grounded ice which reduces the mass flux across the grounding line (e.g. Dupont & Alley, 2005; Goldberg et al., 2009; Gudmundsson, 2013). The collapse or retreat of an ice shelf reduces this back-pressure which can lead to significant acceleration of tributary glaciers. Following the collapse of the Larsen B ice shelf, glaciers that had previously discharged into the ice shelf experienced significant acceleration, whereas nearby glaciers that remained buttressed by an ice shelf did not (Berthier et al., 2012; Rignot et al., 2004). It is this additional mass flux that ultimately contributes to sea level rise (e.g. De Angelis & Skvarca, 2003; Rignot et al., 2004). Even if an ice shelf does not experience complete collapse/retreat, changes in its thickness can also induce changes in the buttressing force. When thinning (thickening) occurs, the buttressing effect is weakened (strengthened). This is particularly concerning as recent research has revealed that overall the volume loss from ice shelves around Antarctica is accelerating (Paolo et al., 2015). Other impacts of changes in ice shelves include modifications to ocean stratification and bottom water formation (Hellmer, 2004), possibly sea ice thickness and extent (Bintanja et al., 2013), shifts in ecosystems (Gutt et al., 2013), and decreasing planetary albedo.

The processes that contribute to ice shelf retreat/collapse are complicated, interconnected, and inconsistent. For example, a number of ice shelves in the Amundsen Sea sector are currently thinning and the buttressing force they provide has been reduced (e.g. Kim et al., 2015; MacGregor et al., 2012; Rignot et al., 2014; Zhang et al., 2014). As a result, these grounding lines are rapidly retreating at rates of several kilometres per year and in many cases have passed the edge of the retrograde bed basin (where the bedrock gets deeper further inland) (Rignot et al., 2014; Scheuchl et al., 2016). As the ice retreats, more ice becomes exposed to the ocean, thus increasing the melting rates, which causes the ice to retreat at a faster rate. This positive feedback mechanism contributes to the 'marine ice sheet instability' hypothesis. There are no bed obstacles to prevent the ice shelf retreating across the entire basin (Rignot et al., 2014). Therefore, even if ocean warming were to stop immediately, we are committed to the loss of this ice, with further ocean warming only increasing the rate at which this occurs (Rignot et al., 2014). This has global significance as the Amundsen Sea sector alone has enough ice to raise global sea level by 1.2 m if it were all to melt (Rignot, 2008).

In comparison, the rapid collapse of the Larsen B ice shelf in 2002 was mainly caused by atmospheric warming, which led to an increase of surface melt pools across the entire ice shelf, rather than instability at the grounding line (Rebesco et al., 2014). However, it is likely that a combination of glaciological, atmospheric and oceanographic factors ultimately contributed to the disintegration. Prior to its collapse a large rift system (which had only developed in the previous 20 years) became more pronounced creating structurally weakened zones within the ice. The buttressing force was reduced by retreat of the ice shelf front between 1998 and 2000. Warming of both the atmosphere and ocean led to increased surface and basal melting respectively, which caused ice shelf thinning. Changes in the velocity and mass balance of tributary glaciers led to further weakening in the suture zones of different flow units across the ice shelf (Glasser & Scambos, 2008). The interaction between these processes caused a preconditioning of the ice shelf which made it vulnerable to collapse.

There is evidence that significant portions of the West Antarctic Ice Sheet (WAIS) were lost in the past (Naish et al., 2009). Recent models predict a 3.3 m sea level rise if the WAIS were to collapse (Bamber et al., 2009). Modelling of the Antarctic ice sheets showed that the disappearance of the WAIS was correlated with an ocean-driven retreat of ice shelves in the Ross, Weddell and Amundsen seas (Pollard & DeConto, 2009). Current mass loss

from the WAIS ranges from 65-150 Gt yr^{-1} (Helm et al., 2014; Sasgen et al., 2013; Shepherd et al., 2012; Vaughan et al., 2013). Most of this net loss is occurring in the Amundsen Sea sector where glaciers draining the ice sheet are thinning at rates of tens to hundreds of centimetres per year (Pritchard et al., 2009). These large changes have shifted the focus away from the larger Ross and Filchner-Ronne ice shelves, which are currently considered to be more stable, but which drain huge areas of the WAIS.

The WAIS was much smaller in the past when temperatures were comparable to what is expected in the future (Joughin & Alley, 2011). In order to predict the response of the Antarctic ice sheet to future changes in climate it is important to understand both the processes occurring today, and how it has responded to changes in the past. This requires a better understanding of the behaviour and vulnerability of the surrounding ice shelves. Important factors include ice volume (area and thickness), velocity, thermal and mechanical properties (how it responds to stresses), mass balance (accumulation vs ablation), hydraulic connectivity to the oceans, and the characteristics of the grounding zone. A key component to addressing these is the ice shelf base which is the most poorly understood and difficult to measure part of the ice sheet system. The structure, morphology and changes in thickness here provide valuable information about the oceanographic conditions and how seawater interacts with the ice shelf.

The most important source of data for ice shelves are satellite-based instruments. Satellites have the advantage of allowing for widespread coverage so the entire continent can be examined as a whole, and changes in time and space can be tracked easily and at relatively high resolution. There are a number of instruments designed for different purposes, and they are not necessarily limited to taking measurements during summer as with most field-based methods. Despite their advantages, satellites are not as accurate as measurements that can be made in the field and so they still require validation in the form of ground-based studies. As the number of satellites and instruments continue to grow, there is an increased demand for ground validation. Additionally, not all required measurements of ice shelves can currently be made using satellites. While satellite-based remote sensing studies can measure properties such as: changes in ice shelf extent (Miles et al., 2016), thickness away from the grounding line (Griggs & Bamber, 2011), volume change (Paolo et al., 2015), grounding zones (Bindschadler et al., 2011) and velocity (Rignot et al., 2011b); they are unable/limited in their ability to sound the ice shelf base in sufficient detail, measure ice thickness at the grounding line, or examine small variations in strain (Marsh et al., 2014).

Desirable ground truthing methods are fast, portable, multi-dimension, non-invasive, inexpensive, easily replicable, and can make simultaneous measurements of multiple properties. Radio echo sounding or radar has been used extensively in glaciology since the 1950's (Bogorodsky et al., 1985) as a method that meets many, if not all of these factors. Radar uses radio waves to penetrate the surface, the properties of which control the propagation of the energy.

In this thesis, radar technology is used to examine ice shelf properties in the grounding zone of the Southern McMurdo Ice Shelf, and the central Ross Ice Shelf (RIS) that cannot easily be determined from satellite data, such as ice thickness, vertical strain, internal stratigraphy, and basal structure. The main research focus of this thesis will be to identify ice shelf properties and processes in radar data, and to discuss the implications they have on the current status and future stability of the ice shelf.

This research will contribute to the understanding of the response of ice shelves to a changing climate and help forecast the local and global effects. In particular, these results will help answer questions posed by New Zealand Antarctic Research Institute's (NZARI) challenge to understand the vulnerability of the RIS. In addition, it will contribute to models of ice thickness at grounding lines measured by satellites, and spatial variability of basal melting beneath the RIS.

1.1 Aims and Objectives

This thesis will examine ice shelf properties and subglacial conditions using ground penetrating and phase sensitive radar. The northern grounding line of the Southern McMurdo Ice Shelf, and the central Ross Ice Shelf are the two focus areas of this study.

The aims of this research are to;

- Identify and map the ice thickness and basal structures across a grounding zone;
- Interpret variations in ice thickness and reflectivity of the ice-water interface to determine distribution of subglacial melting/freezing;
- Determine how internal layering can improve our knowledge of deformation and accumulation processes.

These aims will be met by achieving the following objectives;

- Ice thickness and basal structures across a grounding zone will be examined using low frequency ground penetrating radar (GPR);
- Vertical strain, subglacial melting and freezing will be investigated using a new phase sensitive radar (ApRES) in combination with satellite measurements;
- Internal layering from GPR and ApRES will be analysed to estimate spatial variability in ice deformation.

2 BACKGROUND INFORMATION AND ICE SHELF PROPERTIES

An ice shelf is more than a floating slab of ice, it is a complex system with mass fluxes in all dimensions. Mass is gained from glacial influx across the grounding line, basal freezing, and snow accumulation. Ablation is controlled by iceberg calving and basal melting. The balance between these processes has a large impact on ice shelf stability. A seemingly simple measurement such as ice thickness is complicated by the location of the measurement area, and the presence of firn or marine ice. Any changes in thickness cannot be directly attributed to melting or freezing without taking surface mass balance and ice flow into account.

This chapter provides a brief introduction to the different components of the ice shelf system which are investigated in this thesis, a justification and summary of the use of radar as a glaciological tool, and introduces a new state-of-the-art phase sensitive radar that was developed specifically for monitoring changes in ice thickness.

2.1 ICE SHELF GROUNDING ZONES

The strongest impact of a warming ocean is expected where continental ice first flows into the ocean and becomes an ice shelf, in an area known as the grounding zone. Long term changes in location of the grounding zone and ice thickness in this area have been identified as key indicators of ice sheet stability (Horgan et al., 2013; Katz & Worster, 2010). Processes in grounding zones, such as surface accumulation, basal ablation and firn compaction, are critical to ice sheet mass balance because they influence the mass flux from grounded to floating ice (Jacobel et al., 2014). Changes in ice flux can have important implications for ice sheet stability and sea level rise.

The grounding zone is defined here as the region between the furthest inland point where tidal bending is observed (point F in Figure 1) and the point where the ice reaches hydrostatic equilibrium and is not subject to tidal flexure (point H) (Fricker et al., 2009). The point where the ice detaches from the bed is referred to as the grounding line (point G). Interactions between basal hydrology, atmospheric pressure, sediment transport and tides can change the grounding line location over various timescales. The location of the grounding line can be identified from satellite imagery as a break in slope (point I_b) (Bindschadler et al., 2011; Scambos et al., 2007). However, this method is not particularly

robust as Ib has been observed several kilometres landward of G and even seaward of H (Fricker & Padman, 2006).

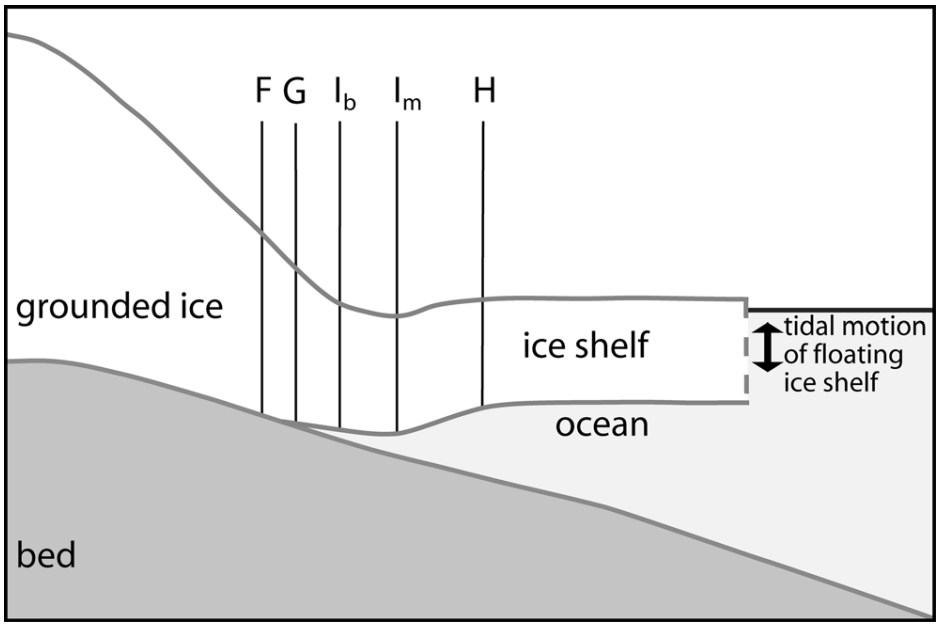

Figure 1. *Schematic of the common characteristics of the grounding zone (GZ). F is the landward limit of tidal flexure, and H is the point at where the ice shelf reaches hydrostatic equilibrium. The GZ is defined as the region between F and H and typically extends many kilometres wide. G is where the ice comes afloat (the grounding line), I_b is the break in surface slope, and I_m is the local elevation minimum (Fricker et al., 2009).*

Other methods of locating the grounding line involve measuring tidal flexure with tiltmeters (Riedel et al., 1999; Stephenson et al., 1979; Wild et al., 2016), Global Positioning System (GPS) (Riedel et al., 1999; Vaughan, 1994), laser altimetry (Fricker & Padman, 2006) or interferometric synthetic aperture radar (InSAR) (Goldstein et al., 1993; Marsh et al., 2014; Rack et al., 2016; Rignot et al., 2011a). A problem with these methods is that they rely on an interpretation of the surface expression of the grounding zone which can be heavily influenced by the characteristics at the base of the ice. In order to assess the accuracy of these methods, direct field measurements of the grounding line are required where properties at the ice base can be linked to their expression at the surface. Radar imaging is commonly used for this purpose (section 2.4).

2.2 Ice Shelves in Hydrostatic Equilibrium

Once the ice has passed through the grounding zone and is in hydrostatic equilibrium it becomes freely floating. Rather than bending, the ice is free to move vertically in response to the tides. While understanding the processes at the grounding line is important for determining the mass flux from land into the ocean, the behaviour of the freely floating ice shelf is also important for ice shelf stability.

The highest rates of basal melting are found near the grounding line, however, the contribution from the FF part of the ice shelf should not be overlooked for two reasons. Firstly, the size of the FF ice shelf compared to the grounding zone means that while melt rates per area may be low, the total contribution can be significant. Secondly, basal melting/freezing beneath the FF part of the ice shelf leads to mass redistribution which can have implications for ice shelf stability (section 2.3.3). Changes in the characteristics (e.g. surface accumulation, thickness, area, surface and basal crevasses) of the FF part of the ice shelf can indicate changes in ice shelf stability (e.g. Glasser & Scambos, 2008; McGrath et al., 2012; Paolo et al., 2015).

2.3 Ice Thickness

The volume of an ice shelf can be described by its area and thickness. While the area of an ice shelf can be accurately measured using satellite imagery, measuring ice thickness is not as straightforward. When an ice shelf is in hydrostatic equilibrium, the gravity force is balanced by the upwards buoyancy force. The height of the ice that floats above sea level (h), called the freeboard, can be measured by satellites which can be converted to total ice thickness (Z) using;

$$Z = \frac{h\rho_w}{\rho_w - \rho_i} \tag{2.1}$$

Where ρ_i and ρ_w are the densities of ice and seawater respectively. In contrast, ice near the grounding line accommodates the differential movement between grounded ice which is not affected by tides, and the floating ice shelf which is. In this region the hydrostatic equilibrium assumption cannot be used to derive ice thickness from freeboard.

Boreholes provide an accurate measurement of ice thickness, but currently the cost and logistics involved with drilling through the ice shelf means that this is a method which is not readily available unless a suite of other measurements are also planned (e.g. Craven et al., 2005; Engelhardt, 2004; Engelhardt & Determann, 1987; Hubbard et al., 2013). Other disadvantages include that neither changes over longer periods of time, or the spatial variability (which can be significant over small areas) can be captured.

Ice penetrating radar is a common glaciological method of measuring ice thickness (section 2.4). While radar is technically a form of remote sensing, in this study the radar used are

ground-based and a general definition of remote sensing to be any non-ground-based measurements (for example satellites and airborne) is adopted hereafter. Using radar as a geophysical tool combined with careful processing and adequate knowledge of the local environment can allow for information on basal ice properties to be derived.

Regardless of the method, there are a number of complexities that arise when measuring ice thickness. If the ice column has a layer of snow and firn (see section 2.3.1) on the upper surface or marine ice (section 2.3.4) at the base, then corrections or assumptions need to be applied to account for this. In addition, changes in thickness over time may not exclusively be a result of mass gain/loss but can be due to changes in the stress regime or accumulation rate causing compression or extension of the ice column (section 2.3.5).

2.3.1 Snow, firn and ice

Freshly fallen snow is subject to metamorphosis, and processes such as wind redistribution and compaction, can change the snow morphology and rapidly increase the snow surface density ($\rho_s \approx$ 300-350 kgm^{-3}). Snow which has survived one summer season and has begun the transformation to ice is called firn. Densification of firn is largely controlled by temperature, accumulation, external stresses, and melting, with density normally ranging from ≈400-830 kgm^{-3} (Cuffey & Paterson, 2010).

The transition between firn and glacial ice occurs at a density of ≈830 kgm^{-3} when air becomes trapped as isolated bubbles. The depth at which this occurs is often used to calculate air layer thickness in firn correction calculations (section 4.2.2). Below this depth, the density of ice increases by compaction of these air bubbles due to creep until it reaches the density of pure ice (917 kgm^{-3}) (Cuffey & Paterson, 2010).

2.3.2 Basal crevasses/cracks

Basal crevasses are cracks which penetrate upwards from the base of the ice shelf. They form through a process called hydro-fracturing where seawater at pressure can enter the base of the ice shelf, normally in an existing zone of weakness, and propagate upwards until the stress at the tip of the crevasse is exceeded by the fracture strength of the ice. Under certain conditions, basal crevasses can penetrate more than half the ice thickness with a theoretical maximum penetration depth of $\pi H/4$, where H is the ice thickness (Weertman, 1973). However, field measurements of basal crevasses have found that they can be much smaller than predicted, possibly due to the back stress of the ice shelf (Jezek, 1984).

Large basal crevasses have been identified in radar signatures from Antarctic ice shelves (Jezek et al., 1979; Luckman et al., 2012; McGrath et al., 2012; Vaughan et al., 2012) and beneath a tabular iceberg calved from the Ross Ice Shelf (Peters et al., 2007).The initiation of basal crevasses is common in, but not restricted to, the grounding zone. As the base of the ice flows across the grounding line it moves through a changing stress field. This can lead to brittle deformation and the formation of small cracks, which can result in the creation of basal crevasses through the process of hydro-fracturing described above. Once a crevasse is formed its evolution is controlled by ductile deformation and ice-ocean interactions. A crevasse can be widened when the longitudinal tensile strength is greater than the gravitational restoring force. This process is called necking and can result in a depression forming at the surface (Bassis & Ma, 2015). A reduction of the buttressing force provided by ice shelves may increase the size to which basal crevasses can form (Jezek, 1984).

Crevasses increase the area of the local ice-ocean interface and act as preferential freezing or melting conduits. A crevasse can be filled by marine ice forming in cold ocean water, or is further eroded if the ocean is warm. In the context of global climate change, ocean warming may lead to the input of more warm water into the sub ice shelf cavity which not only promotes increased basal melting but also facilitates the growth of basal crevasses that leads to structural weakening of the ice shelf which can be a prelude to disintegration (Vaughan et al., 2012). Basal crevasses can advect downstream and the largest ones can persist to the calving front (Wesche et al., 2013). The size, orientation and abundance of basal crevasses can also assist in determining the local stress state (Jacobel et al., 2014).

Despite their predicted abundance (Shabtaie & Bentley, 1982), the implications of basal crevasses on ice shelf stability are not well known. Although basal crevasses were not directly linked to the collapse of the Larsen A and Larsen B ice shelves, it has been suggested that they were important for preconditioning making the ice more vulnerable to disintegration (McGrath et al., 2012). There is some evidence which suggests that basal crevasses lead to structural weakening of ice shelves and the subsequent lowering of the ice surface creates areas where meltwater is likely to accumulate which only further exacerbates ice shelf vulnerability (McGrath et al., 2012).

Unlike surface crevasses, basal crevasses are not easily visible in satellite imagery unless they are of significant size to have a surface expression. Even if a surface trough exists, its

depth is influenced by a number of factors including the size of the crevasse, the density profile of the ice column, surface accumulation (which may be higher within the depression), and the presence of marine ice (Luckman et al., 2012). Therefore, surface trough dimensions are not a good proxy for basal crevasses. Even though they are often interpreted as surface crevasses in satellite imagery, the formation of surface crevasses is very different to that of basal crevasses. Incorrectly classifying features in satellite imagery can result in an inaccurate understanding of the structural properties of ice (Luckman et al., 2012).

Many basal crevasses are not wide or deep enough to create a surface depression so the identification of these is limited to ground-based methods such as ice penetrating radar. This is especially important in grounding zones where they can be relatively small in size but exist in abundance (van der Veen, 1998). The presence of basal crevasses can have a significant impact on ice properties such as elasticity and strength which can alter the apparent ice thickness (Vaughan, 1995). This can indirectly influence tidal flexure patterns, which are a common method of identifying the grounding line (Rosier et al., 2016).

2.3.3 Basal melting/freezing

Basal melting is the dominant way that ice shelves lose mass, exceeding losses by calving (Rignot et al., 2013). Basal melting occurs when water above the seawater freezing temperature is in contact with the base of the ice resulting in a net upwards heat flux. High rates of basal melting occur at the grounding line of ice shelves (Marsh et al., 2016), where the pressure melting point is depressed (i.e. as the pressure increases the seawater freezes at a lower temperature), and also near the calving front (Arzeno et al., 2014).

Variation in basal melting and freezing occurs at different spatial scales from across the entire ice shelf because of ocean circulation to smaller local areas with rough basal topography where thicker is preferentially melted and marine ice accumulates under thinner ice. Basal melting can also be concentrated in channels that may be related to subglacial drainage beneath the ice sheet (Alley et al., 2016; Le Brocq et al., 2013; Marsh et al., 2016). These processes lead to uneven melt and freeze distribution which can have implications for total mass loss, buttressing, and ice dynamics (Millgate et al., 2013; Stanton et al., 2013). However, not all meltwater contributes to total mass loss as some is refrozen as marine ice to the base of the ice shelf.

2.3.4 Marine ice

Meltwater generated at the grounding line ascends beneath the ice shelf as a water mass called ice shelf water (ISW). As ISW ascends the pressure decreases, and eventually the water reaches the pressure freezing point where frazil ice crystals can form. These ice crystals buoyantly rise and attach to the base of the ice shelf. Over time these crystals become compacted as new crystals grow underneath and eventually consolidate into a layer of marine ice. Marine ice formation can significantly influence the total basal mass loss. On the Amery Ice Shelf (AIS) 25% of melted water is thought to refreeze as marine ice (Galton-Fenzi et al., 2012). Extensive layers of marine ice, hundreds of metres thick, have been recorded under several major Antarctic ice shelves including the Filchner-Ronne Ice Shelf (Oerter et al., 1992) and the AIS (Fricker et al., 2001) which are the second and third largest Antarctic ice shelves respectively. Marine ice can be important features for the structure and stability of an ice shelf. The layer underneath the AIS is up to 190 m thick and accounts for ≈9 % of the ice shelf volume (Fricker et al., 2001).

Marine ice is distinct from meteoric ice for a number of reasons including its mode of formation, physical and chemical properties, and response to external stresses. Marine ice is formed from the freezing of seawater, and so it contains brine channels and pockets (Craven et al., 2009; Zotikov et al., 1980). Oerter et al. (1992) report marine ice salinities of 0.1 ‰ on the Filchner-Ronne Ice Shelf which is an order of magnitude above meteoric ice but much less than that of seawater (3-10 ‰). As marine ice ages and thickens, its salinity decreases by brine rejection. On the AIS salinities of 0.03 ‰ near the meteoric/marine ice interface increase to 0.56 ‰ at 120 m below the boundary (Craven et al., 2009). Marine ice has a temperature similar to the sub-ice shelf ocean water (-2 °C to -1.5 °C) so is warmer and softer than the meteoric derived ice shelf (Dierckx & Tison, 2013). As a result, marine ice deforms more readily than meteoric ice under the same stress conditions and it is less prone to elastic fracture (Jansen et al., 2013). As ice has a low thermal diffusivity, the contrast in temperature (and thus rheology) between marine and meteoric ice can persist along the entire ice shelf (Craven et al., 2009). Marine ice has shown to be an important factor in increasing ice shelf stability (Kulessa et al., 2014; McGrath et al., 2014).

Understanding the processes that control the formation and distribution of marine ice is therefore important to understanding the ice shelf system and its interaction with the oceans. The presence of marine ice indicates the presence of a significant ISW layer which

can insulate the ice shelf base from melting. Changes in marine ice can be linked to changes in ocean circulation and grounding line processes. Many oceanographic measurements (such as temperature, salinity, and current) are made at the front of the ice shelf from which the conditions in the sub-ice cavity are inferred (Arzeno et al., 2014). If the distribution, thickness, or growth and melt rates of marine ice are better understood, measurements of ISW can be used to calculate basal melting in more defined areas such as within the grounding zone or near the ice shelf front.

2.3.5 Strain thinning/thickening

The dimensions of an ice shelf are heavily influenced by the geometry of the coastline. Ice spreads and thins to fill embayments, or is thickened when ice streams converge or the ice shelf is compressed between pinning points. The change in ice thickness as a result of this is known as strain thinning or thickening.

Strain is the deformation of a material in response to a stress, and in the case of an ice shelf the stress is either extensional (tensile) or compressional. As the ice shelf surface is very flat and the ocean does not exert basal friction, shear stress is insignificant. In simple one-dimensional cases strain can be calculated using $\frac{L_f - L_i}{L_i}$, where L_f and L_i are the deformed and un-deformed length of the object respectively. However, ice shelves are three dimensional and processes such as accumulation, firn densification, and basal melting/freezing can make strain more complicated to calculate.

Vertical strain describes where and how the ice shelf is thinning (negative values of strain) and thickening (positive strain), and is opposite in sign to horizontal strain, (i.e. when an ice shelf is laterally spreading it is simultaneously thinning). Traditional methods of calculating vertical strain commonly involve the conversion of horizontal strain measured at the surface to vertical strain. This can be achieved by installing a strain network which is a series of stakes/stations (Crary et al., 1962a; Jenkins & Doake, 1991; Makinson et al., 2012), or measuring ice velocity (Treverrow et al., 2010; Young & Hyland, 2002) from which horizontal strain in two orthogonal directions can be derived (section 4.2.4.1).

While useful as an approximation, there are a number of uncertainties and limitations associated with this indirect method of measuring vertical strain on ice shelves. Firstly, if there is a firn layer, it is assumed that this will respond in the same way to applied stresses as the ice underneath. Secondly, it assumes that the strain rate is constant with depth (which

is valid on the freely floating part of the ice shelf (Sanderson & Doake, 1979) but not within the grounding zone (Jenkins et al., 2006)). Thirdly, installation of a strain network and carefully repeated measurements are time consuming and do not capture the temporal variability in strain that can be associated with tidal motion. Other methods of calculating vertical strain involve drilling boreholes (Craven et al., 2009; Paterson, 1976), but unless there is a borehole being drilled for other purposes this method is not commonly used as it is expensive and time consuming. Long term monitoring of vertical strain would require the borehole to be kept open for an extended period of time.

Measurements of strain have previously been used to examine ice shelf stability and vulnerability by linking horizontal strain to surface features (Corr et al., 1998; Kulessa et al., 2014). The rapidly increasing interest in basal melting/freezing processes and its effect on ice shelf stability, in conjunction with the availability of satellite data, has led to an increased demand for spatially extensive mapping, modelling and monitoring of basal melting/freezing. Accurately measuring these processes using changes in freeboard (which is proportional to ice thickness) requires an accurate understanding of the other processes that contribute to thickness change (e.g. vertical strain, accumulation and firn densification). Thus, there is a demand for measuring vertical strain more efficiently and cheaply than these established methods (stake networks and boreholes) have offered.

2.4 RADAR IN GLACIOLOGY

Radar (RAdio Detection And Ranging) was first successfully used in Antarctica in 1957 and has since become a standard glaciological tool in modern polar research (Bogorodsky et al., 1985). Radar sounding is an active-sensing method; radio waves are directed down into the surface and the reflection off inhomogeneities in the ice is measured at the surface. Snow and ice have electrical properties which make them ideal for radar sounding (section 4.1.1). There are many advantages to using radar in glaciology; it is non-invasive so the subsurface can be examined in great detail without disturbing it; most systems used for glaciology are portable and can be deployed on the ground, or on an aircraft or satellite; it is a quick way to collect data and has wide ranging applications.

Many of the earliest studies (e.g. Bailey et al., 1964; Walford, 1964) were focused on collecting ice thickness data with airborne radar, which has the advantage of allowing large areas to be covered in a short space of time. Although airborne studies still remain common (e.g. Bingham et al., 2015; Karlsson et al., 2009; Peters et al., 2005) they are becoming

increasingly supplemented by ground-based studies (e.g. Arcone et al., 2005a, 2005b; Kruetzman et al., 2011). The advantage of a ground-based system is that a smaller area can be examined in more detail, which allows for the closer examination of the nature of the base of the ice, and internal layers which provide information about snow accumulation (e.g. Eisen et al., 2008; Kruetzman et al., 2011; Rotschky et al., 2006), stratigraphy (e.g. Catania et al., 2005), internal ice properties (e.g. Drews et al., 2012), subglacial conditions (e.g. Horgan et al., 2013) and ice flow (e.g. Bingham et al., 2015).

In this study, two different types of radar are used, each of which are designed for different purposes. Ground penetrating radar, which is a well-established glaciological tool, is used to measure ice thickness, internal stratigraphy, basal structures and grounding zone conditions. And a newly developed phase-sensitive radar is used to examine vertical strain, ice thickness, basal melting/freezing and the distribution of marine ice.

2.4.1 Phase sensitive radar

In order to address the need for more accurate methods for measuring changes at the ice shelf base, the British Antarctic Survey (BAS) have developed a phase-sensitive radar (pRES) for measurement of basal mass balance and vertical strain (Corr et al., 2002). The technology is still improving but has successfully been used to measure basal melt rates (Corr et al., 2002; Marsh et al., 2016), vertical strain rates (Jenkins et al., 2006; Kingslake et al., 2014; Nicholls et al., 2015), and ice rheology properties (Gillet-Chaulet et al., 2011) on both ice shelves and ice sheets. The most recent version of pRES, called autonomous pRES (ApRES), is used in this study and is a robust, inexpensive system designed for long term monitoring of ice-shelf and ice-sheet thickness changes (Brennan et al., 2014). Its low power consumption means that it can be left unattended in the field for long periods of time taking multiple measurements per day. The system is tolerant to temperatures down to -40 °C giving it the ability to capture data during the polar winter. ApRES is portable enough that it can be used at many sites during a single field campaign. In addition, ApRES has the ability to measure the vertical variability in strain to very high accuracy.

3 STUDY AREA

To examine both the freely floating ice shelf and the grounding zone, and to fully address the research objectives two separate field areas were investigated. These two areas, the Southern McMurdo Ice Shelf (SMIS) and the Ross Ice Shelf (RIS), were visited in November 2014 and November 2015 respectively as part of two Antarctica New Zealand events (K053 and K061).

3.1 THE SOUTHERN MCMURDO ICE SHELF

This section is an introduction to the geographic and climatic characteristics of the SMIS. Key place names are defined and a review of the available literature is presented. A description of the field site across the White Island grounding line is also included.

3.1.1 Location

The McMurdo Ice Shelf (MIS) is a small ice shelf (≈5000 km^2), which occupies the southern area of McMurdo Sound and is adjacent to the RIS. It is separated from the RIS by a 25 km wide shear zone which extends from the tip of Minna Bluff, past the eastern edge of White Island to Cape Crozier (Figure 2). The MIS is bounded in the north by McMurdo Sound and Ross Island, and by Minna Bluff to the south. The glaciological differences of the MIS compared to the adjacent larger RIS were first discussed in 1961 (MacDonald & Hatherton, 1961). Ice velocity is much slower and in a different direction to that of the RIS, with a significantly thinner calving front (MacDonald & Hatherton, 1961). The SMIS is the part of the MIS which extends south of Black and White Islands to Minna Bluff (Figure 2). Both parts of the MIS (north and south) are characterised by surface ablation to the west and accumulation towards the east. An abundance of marine fossils and muds on the ice shelf surface in the ablation area led to the conclusion that the western area of the MIS is balanced by basal freezing. The upwards propagation of these marine horizons by surface ablation is termed the 'Debenham Mechanism' (Debenham, 1920). In contrast, the eastern MIS receives 18 cm water equivalent (w.e.) accumulation, but is subject to basal melting of up to 0.73 ma^{-1} w.e. (Stuart & Bull, 1963). On the SMIS the ablation area is a band north of Minna Bluff which extends south-east of Black Island through Moraine Strait.

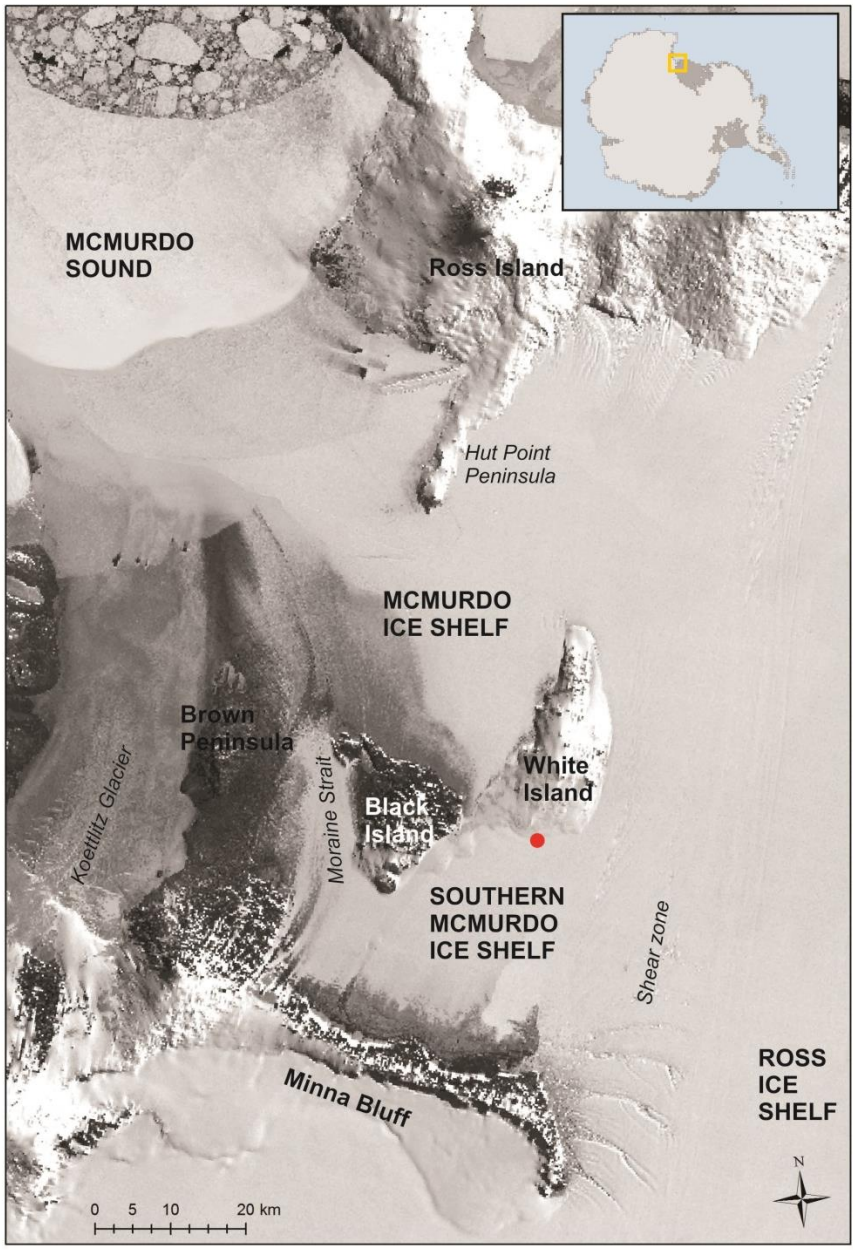

Figure 2. *The Southern McMurdo Ice Shelf with surrounding region and features. The red dot is the location of the field camp. Scott Base is on the southern tip of Hut Point Peninsula.*

3.1.2 Climatic setting

McMurdo Sound lies at the confluence of three distinct air masses: very cold, dry air draining off the East Antarctic Plateau; cold southerly air from the Ross Ice Shelf; and moist, relatively warm maritime air from the Ross Sea in the north (Monaghan et al., 2005). These combine to form complex weather and climatic patterns which are further modified by orographic influences on the near surface winds due to the Transantarctic Mountains. Monaghan et al. (2005) used twice-daily forecasts from the 3.3 km resolution domain

Antarctic Mesoscale Prediction System (AMPS) to study the climate of the McMurdo area from June 2002 to May 2003. They find that average annual accumulation across the White Island grounding zone is approximately 0.20 ma^{-1} w.e. and average temperature is -18 °C to -20 °C, with a general eastwards decrease in both (Monaghan et al., 2005).

3.1.3 Previous studies on the SMIS

The first comprehensive glaciological survey of the MIS was conducted by Swithinbank (1970) during 1960-1962 (Figure 3). Ice thickness was measured using radio echo sounding (RES), and ice shelf velocity was derived from stake surveys, however, the focus of this study was the northern MIS and Moraine Strait. The only measurements made on the SMIS were between Black Island and Mt Discovery (Figure 3). Only four ice velocity measurements were made here, and they were considered the hardest to survey due to difficult terrain (Swithinbank, 1970). The estimated movement rates are 0.5-2 ma^{-1} but these have a large associated error (15%). This zone was also where the majority of RES ice thickness measurements were conducted on the SMIS with values varying between 70 – 105 m. There was one isolated measurement made to the east of Brown Peninsula of 20 m (Swithinbank, 1970).

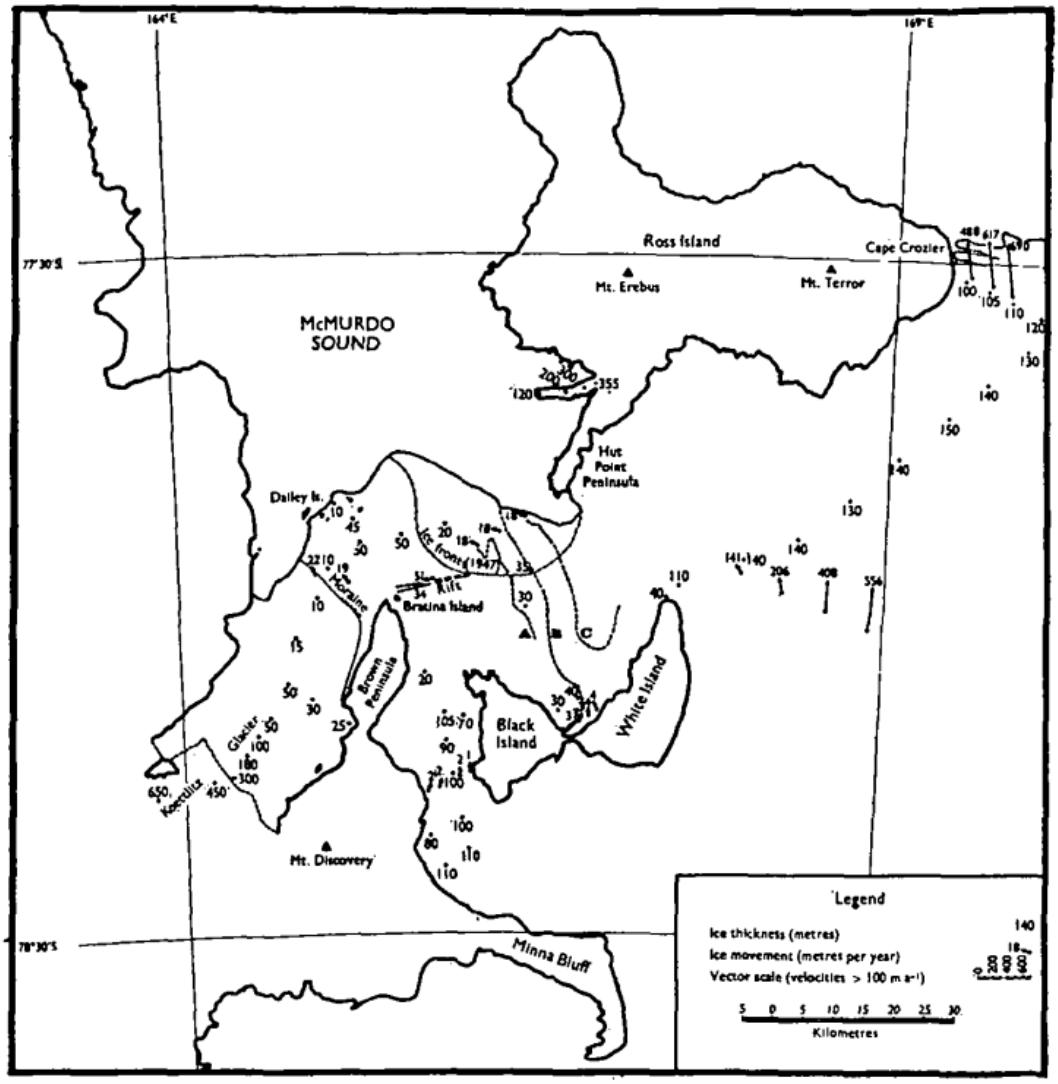

Figure 3. *Ice thickness and velocity measurements of the McMurdo Ice Shelf (Swithinbank, 1970).*

The first dedicated study of the SMIS was conducted during the 2002/03 – 2004/05 austral field seasons (Clifford, 2005). Ice motion was measured using a series of stakes (Figure 4), and surface features were described from field observations, and radar and satellite imagery. This work revealed that; the SMIS is an independent ice shelf which is separated from the RIS and rest of the MIS by the shear zone and a subglacial isthmus between Black and White Islands; surface processes are driven by local katabatic winds, causing surface ablation near Minna Bluff and Moraine Strait where winds are the strongest, and accumulation near the south-eastern edge of Black Island and southern edge of White Island; horizontal ice velocities (2-7 ma^{-1}) are two orders of magnitude lower than that observed on the adjacent RIS and MIS, with negligible ice input from these larger ice shelves. Instead ice moves primarily as a result of gravitational creep due to decreasing ice thickness and surface slope from the accumulation area in the south-west towards the

ablation area and through Moraine Strait. It was also identified that the SMIS will respond differently to climate change than other ice shelves surrounding the continent. Although it is sensitive to changes in sea level and ocean temperature/ circulation, it is buffered from collapse by the surrounding land masses and the MIS (Clifford, 2005).

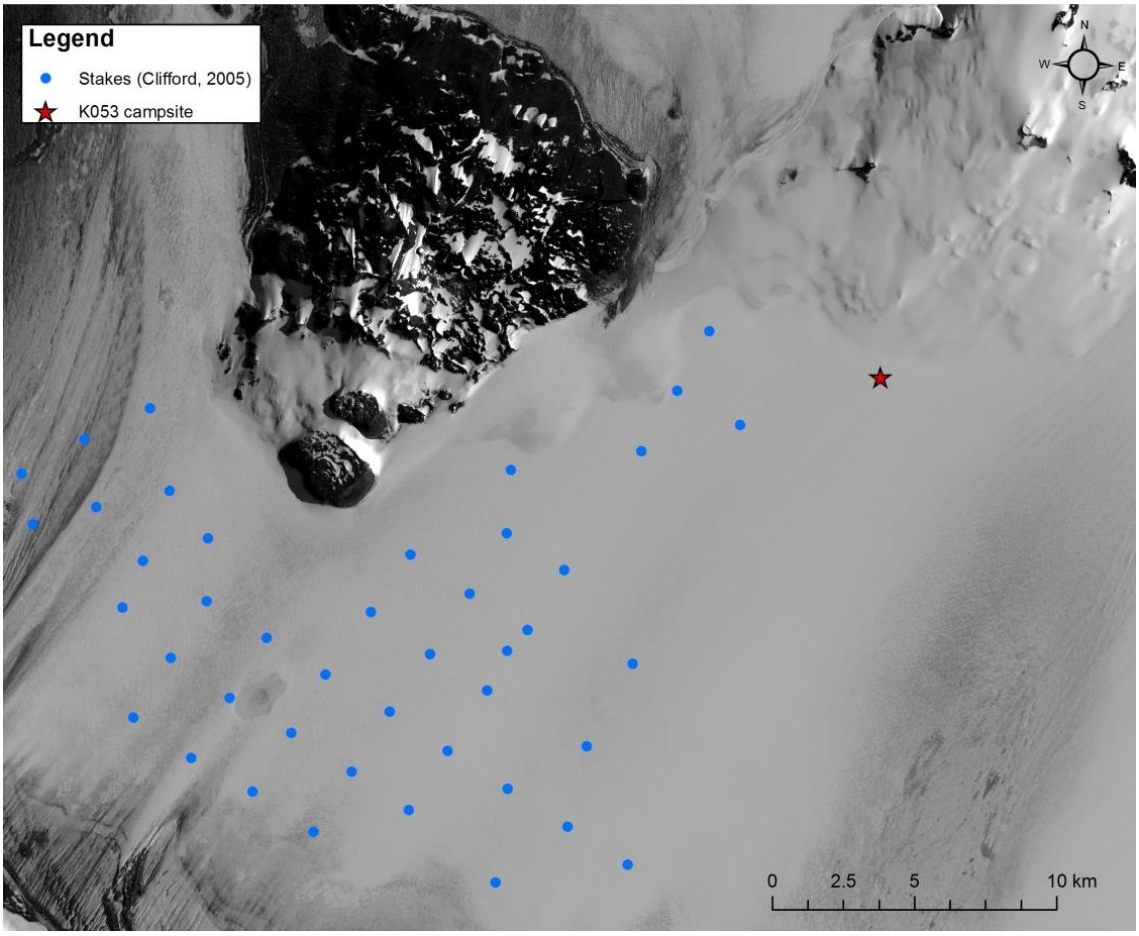

Figure 4. *Location of measurement stakes on the SMIS from Clifford (2005) in blue. The red star is the field site for this study.*

While this study hugely increased the knowledge about the SMIS, it too was focused primarily on the ablation area between Black Island and Minna Bluff.. More recent studies of the SMIS have also been focused on the surface ablation area (e.g. Fitzsimons et al., 2012; Glasser et al., 2006; Glasser et al., 2014; Koch et al., 2015) or have been collected remotely (e.g. Rignot et al., 2011b). Therefore, there is a lack of direct measurements and information about the surface accumulation region of the SMIS which is likely to have different properties and behaviours to the ablation zone.

3.1.4 Description and rationale of the SMIS field site

The SMIS field site is approximately 50 km south-east of Scott Base in the southern White Island grounding zone (Figure 2). The area studied is a rectangular grid with transects

roughly perpendicular and parallel to the grounding line (section 5.1.1.3). A first estimate of the grounding line location was made using differential InSAR satellite analysis (W. Rack, personal communication, October, 2014). This matches with the surface features in LANDSAT satellite imagery that Clifford (2005) interpreted as the grounding line on Black Island. At the surface the grounding line is difficult to discern, characterised only by a subtle increase in slope from the flat ice shelf to the grounded ice on White Island.

The SMIS near White Island is an ideal site for examining characteristics of an ice shelf across a grounding line such as ice thickness, basal crevassing and internal layering because;

- There is no information about ice thickness or basal topography and only modelled accumulation in this area;
- Low velocities means that horizontal shearing at the grounding line is minimal, so this is a rare example of a 'stationary' ice shelf and therefore ice shelf properties are related to local processes;
- It provides an easily accessible and safe field site to study grounding zone behaviour.

3.2 The Ross Ice Shelf

The Ross Ice Shelf (RIS) is the largest ice shelf in the world and its vulnerability to a warming climate has global importance due to its contribution to global ocean circulation, albedo, and the buttressing effect it has on a large number of ice streams and outlet glaciers which indirectly affect the rate of sea level rise.

3.2.1 Location

The RIS is located in the Ross Sea, with an area (≈490,000 km^2) similar to that of France. It is bounded by the Transantarctic Mountains to the west, Marie Byrd Land to the east, and the Ross Sea to the north (Figure 5). The ice front extends for almost 800 km from Ross Island to Edward VII Peninsula. Ice thickness varies from approximately 750 m at the grounding line to 100 m at the ice edge.

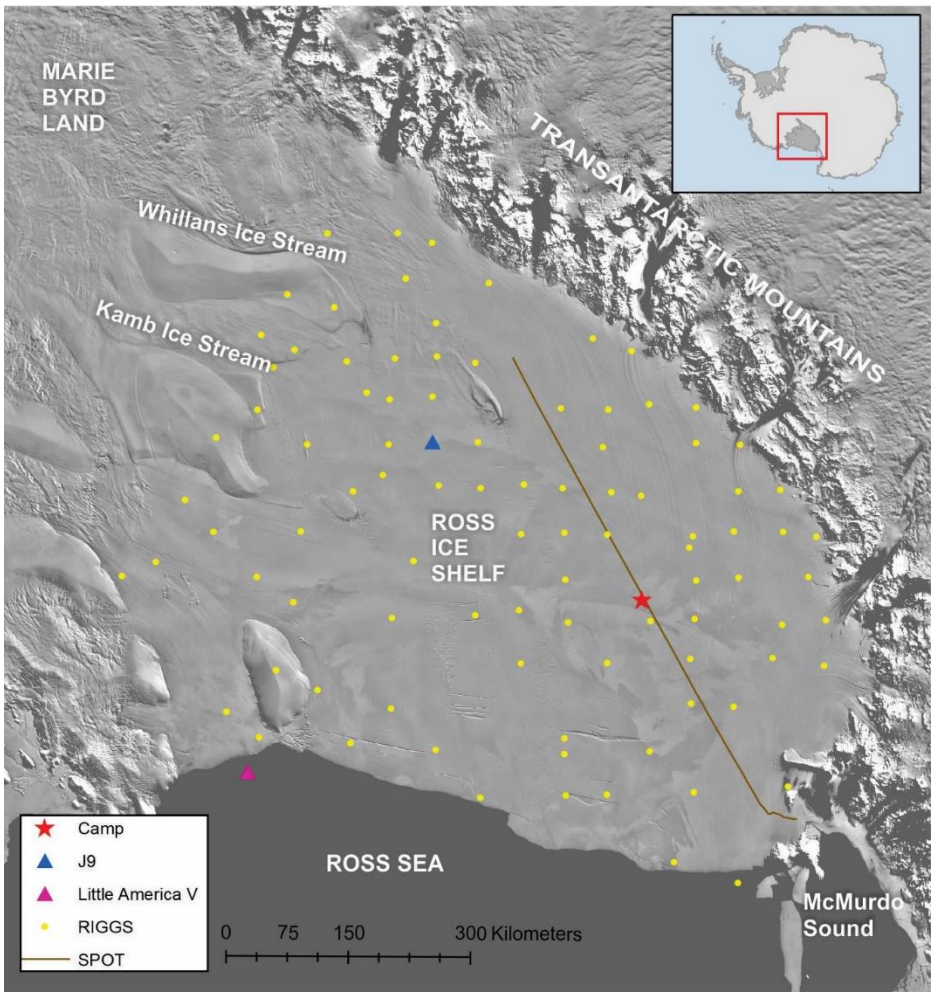

Figure 5. *The RIS, surrounding areas, and the location of previous ground-based glaciological studies. Yellow dots represent sites from the RIGGS survey (Bentley, 1984), the pink triangle is the location of the Little America V site before that section of the ice shelf calved off (Ragle et al., 1960), the blue triangle is the J9 drill site (Clough & Hansen, 1979), the brown line represents part of the South Pole Overland Traverse route across the RIS, and the red star indicates the location of the field camp which is the centre of the study area.*

3.2.2 Oceanic setting

There are very few direct oceanographic measurements beneath the RIS (Clough & Hansen, 1979), so most of the information about the circulation, salinity and temperature has been gathered from modelling (Holland et al., 2003; Reddy et al., 2010) or inferred from measurements along the ice shelf front (Arzeno et al., 2014; Smethie & Jacobs, 2005).

The Ross Sea continental shelf is one of two major sources of Antarctic Bottom Water (AABW) supplied to the deep Southern Ocean, which in turn is a major factor in global thermohaline circulation. AABW is formed by cooling of water in polynyas and beneath ice shelves. High Salinity Shelf Water (HSSW) flows into the RIS cavity along the sea floor in the western Ross Sea (Jacobs et al., 1979). HSSW, and Low Salinity Shelf Water (LSSW) are formed when brine is rejected during the formation of sea ice during winter. When warm HSSW contacts the ice shelf base it is transformed into Ice Shelf Water (ISW), which is colder than the sea surface freezing point and has a lower density so is buoyant compared to the higher salinity HSSW (Figure 6). ISW flows out of the cavity at a longitude of ≈180°, but also further east, and to the west of Ross Island into McMurdo Sound (Holland et al., 2003). The modelled mean temperature (-2.04 °C) and salinity (34.67 ‰) in the cavity closely matches that which was measured at the J9 borehole (section 3.2.4) in 1978 (-2.01 °C and 34.62 ‰) (Holland et al., 2003). The model indicates that there is a seasonal variability in the outflow of ISW. Measurements of basal melting made along the ice front also suggest a strong variability across different timescales; however observations were limited to a two month period starting in November 2010 (Arzeno et al., 2014). The variance in sub-ice shelf currents is greatest in winter when stratification in the Ross Sea Polynya is weakest. Overall there is net basal melting, with melting near the ice front up to 10 times higher than ice shelf average due to seasonally warmer upper ocean water in the RIS when the Ross Sea Polynya is free of sea ice (Arzeno et al., 2014).

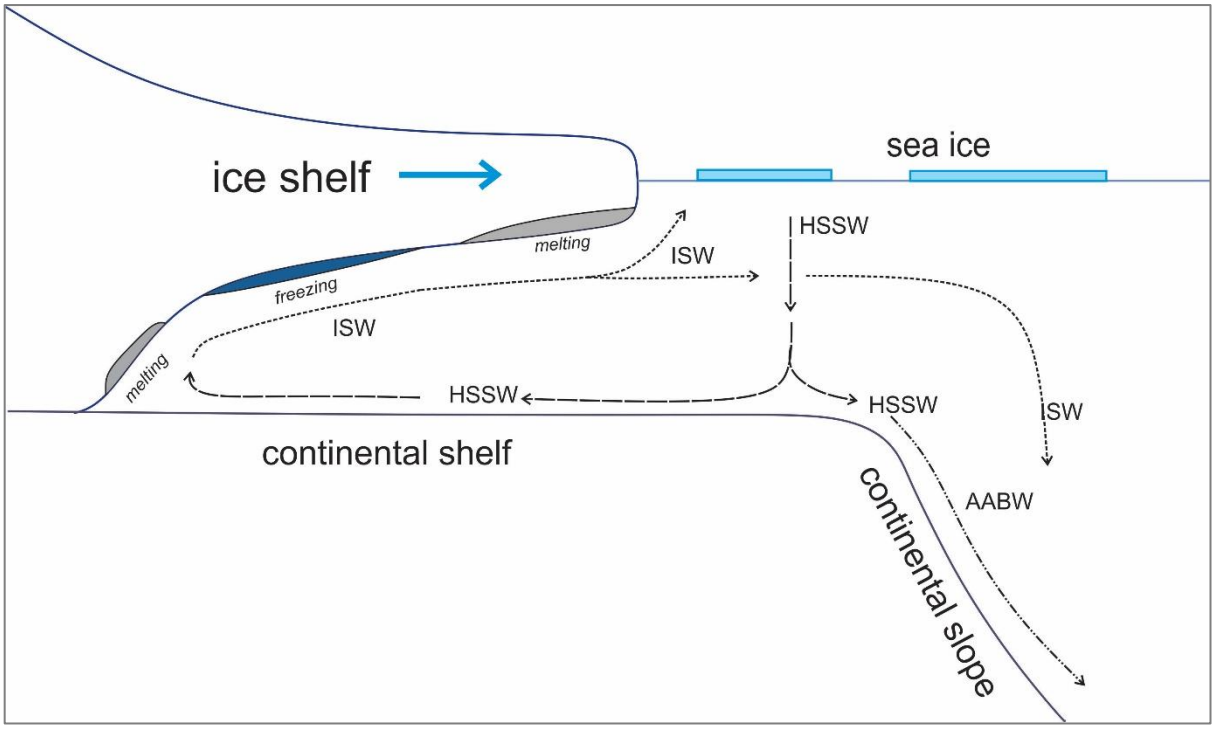

Figure 6. *Schematic of a cross section showing the regional ocean circulation beneath the RIS. HSSW is high salinity shelf water, ISW is ice shelf water, AABW is Antarctic bottom water (adapted from (Jacobs et al., 1992)).*

3.2.3 Glaciological setting

The RIS drains much of the West and East Antarctic Ice Sheet (WAIS and EAIS respectively). The EAIS feeds the RIS by glaciers which flow through the Transantarctic Mountains, and ice streams drain the WAIS across the Siple Coast. Ice flows north through the RIS at rates of 100-1000 ma^{-1} (Rignot et al., 2011b). Flowlines, clearly visible in satellite imagery, allow ice to be traced back to its grounding line source. This reveals that most of the RIS is sourced from ice flowing from the WAIS. Much of the bedrock beneath the WAIS is grounded below sea level, and so the buttressing force provided by the RIS is an important factor in the stability of the WAIS (Pollard & DeConto, 2009).

3.2.4 Relevant previous studies of the RIS

Due to its size and importance, the RIS has received significant scientific interest with a number of large studies focusing on quantifying its glaciological properties. The major projects that have led to advances in our knowledge of the ice shelf since the 1970s are discussed below with respect to their main aims and results.

Dedicated scientific investigation of the RIS began during the International Geophysical Year (IGY, 1957-1958). A party of scientists circumnavigated the RIS taking measurements of elevation, seismic reflection, gravity, magnetism, snow temperature and density (Crary et al., 1962b). Also during the IGY, the ice shelf was drilled at the Little

America V site, less than 3km from the ice front, and an ice core was extracted. The density and structure of the ice was examined and layers of volcanic ash were identified. No saline ice was found at the base of the core indicating that the bottom layer of the ice shelf was melting at this site (Ragle et al., 1960).

The first comprehensive, ice shelf wide study was the Ross Ice Shelf Geophysical and Glaciological Survey (RIGGS) which was conducted over the 5 year period from 1973-1978 (Bentley, 1984). Measurements of accumulation rate, strain rate, ice thickness, subglacial water depth, temperature, and surface movement rates were made at 200 sites on a grid with roughly 55 km spacing. In addition, 13 500 km of airborne radar soundings were made from which ice thickness was calculated at 1 km intervals (Bentley, 1984). The strength of the radar reflection was used to produce a map of predicted marine ice extent (Neal, 1979).

One of the initial aims of the RIGGS survey was to find the optimal site for a drill hole as part of the Ross Ice Shelf Project (RISP), which was achieved in 1973-74. The project was then extended to cover the entire RIS after the importance of such a survey was recognised. The objectives of the RISP were to investigate the physical, chemical, biological and geological properties of the ice shelf, the water beneath the ice and the seafloor to examine the present and past conditions of the RIS (Clough & Hansen, 1979). The drill site for RISP, named ‘J9’, was approximately 450 km from open sea (Figure 5). A hole was drilled through the ice shelf in December 1977 and was kept open for a three week period of sampling. Oceanographic sampling revealed a layer of cold fresh water near the ice shelf base, and a relatively warm saline layer near the seabed suggesting that melting rather than freezing was occurring at the bottom of the ice shelf at this location (Clough & Hansen, 1979).

These early studies were mainly focussed on characterising the ice shelf with little emphasis on the stability of the ice shelf in response to different climatic forcing. It has only been in recent decades that the history and vulnerability of the RIS has become a focus for research. The stability of the RIS remains poorly understood but a number of studies have begun to reveal the complexities associated with the interactions between the ice shelf, ice sheet and the underlying ocean.

In 1983 the Siple Coast Project was started with the aim of investigating the behaviour and interaction of ice streams B and C (since renamed the Whillans and Kamb Ice Streams

respectively, Figure 5) with the RIS (Bindschadler, 1993). These two adjacent ice streams were displaying contrasting behaviours with Ice Stream B speeding up and thinning, while Ice Stream C had stopped flowing in the last few centuries and had started thickening. These changes are not accounted for in the ice shelf buttressing model. This is an important result as it indicates that the WAIS is currently responding to changes from the last global glaciation ~10 000 years ago, as well internal instabilities which are independent of modern climate change (Bindschadler, 1993).

Sediments beneath the ice shelf contain information about the past extent of both the ice shelf and ice sheet. A sediment core extracted from the MIS as part of the ANDRILL project revealed that the ice shelf/sheet has periodically collapsed and re-advanced during orbital cycles (Naish et al., 2009). A borehole was also drilled near the grounding line of the Whillans Ice Stream during the 2014/15 season as part of the WISSARD (Whillans Ice Stream Subglacial Access Research Drilling) project and a sediment core was recovered in addition to the deployment of oceanographic, biological and geological instruments, collection of water samples and ice cores.

Basal channels near the grounding line of the Whillans Ice Stream have been shown to be created by basal melting influenced by subglacial drainage (Marsh et al., 2016). This indicates that ice shelf stability may be influenced by subglacial hydrology and drainage of meltwater from beneath the ice sheet. Studies on other ice shelves have shown that basal melting and channels do not only occur near the grounding line due to the influx of warm HSSW water, or from subglacial drainage, but can also form further out on the ice shelf where oceanographic conditions have changed (Alley et al., 2016).

In the last two decades, satellites have provided wide coverage of ice shelves and allow for changes to be monitored. This has enabled high resolution, ice-shelf wide data sets to be created. Griggs and Bamber (2011) used altimetry measurements from the European Remote Sensing (ERS-1) satellite to create the first Antarctic-wide map of ice shelf thickness. Interferometric synthetic aperture radar data acquired from a number of satellites during 2007-2009 has been used to create a high resolution map of ice velocity of the Antarctic Ice Sheet and adjacent ice shelves (Rignot et al., 2011b). A comparison of surface velocities, from the RIGGS survey and satellite feature tracking, across the entire RIS over a 30 year period revealed widespread slowing with localised areas of acceleration. This, combined with changes in ice thickness are used in an ice shelf model to show that modern

changes in ice flow are dominated by the stagnation of the Kamb Ice Stream (Ice Stream C) 160 years ago, and changes in basal drag on the Whillans Ice Stream ice plain (Hulbe et al., 2013).

During the 2015/16 Antarctic season the ROSETTA-ICE project began an airborne survey over the RIS to help answer questions about the stability of the RIS. A suite of gravity, magnetics, radar, LIDAR and imagery instruments are installed on an aircraft which will be flown over the RIS during two field seasons. This data will be used to measure and map ice thickness, structure, crevassing, channels, surface accumulation, and marine ice distribution over the entire ice shelf. The data collected for this thesis will complement and may be used to help validate these airborne measurements.

3.2.5 Rationale for field site on the RIS

As discussed in section 3.2.2, few direct observations of the oceanography beneath the RIS have been made in the past. Measurements of the ice shelf base provide valuable information about the interaction of seawater with the ice shelf. This understanding is important for estimating patterns of basal melting and freezing. Current measurements are limited to the frontal edge (Arzeno et al., 2014; Smethie & Jacobs, 2005; Stuart & Bull, 1963), the J9 borehole on the eastern region of the ice shelf (Clough & Hansen, 1979), and at the Whillans grounding line (Marsh et al., 2016). There is a clear lack of information about the basal properties of the RIS from the western area which may exhibit different responses as this ice is sourced from the colder, thicker EAIS.

In addition, with remote sensing based studies becoming more prevalent, and the stability of the RIS being recognised as having global impact, modern ground-based measurements in this area will be important in the future for validating models and interpreting airborne or satellite data.

3.2.6 Description of the RIS field site

The field camp is located near the confluence of ice originating from the EAIS and WAIS, and is approximately 350 km southeast of Scott Base along the South Pole Overland Traverse road (SPOT) (Figure 5). The primary area of interest is within a 30 km radius of the field camp, with additional measurements made along the route between Scott Base and this site. Additional observations made in the field are described in (section 5.2.3.2) and a map of the measurement sites is in (section 5.1.2.2).

4 GEOPHYSICAL AND GLACIOLOGICAL METHODS

This chapter provides a description of the basic properties of radar wave propagation in ice, and the glaciological measurements made in this study.

4.1 RADAR

Many different types of radar exist for glaciological applications. The basic principles of electromagnetic (EM) wave propagation are identical for every system, but they are uniquely designed for their particular purpose. This section will describe the principles of EM wave propagation in ice and then discuss GPR and ApRES radar, and how they are used in this study, in more detail.

4.1.1 Electromagnetic wave propagation in ice

The propagation of EM waves at radio frequencies (f) through a material depends on its electrical properties, specifically the relative permittivity (ε_r) and electrical conductivity (σ) (Table 1). EM waves attenuate rapidly in materials with high conductivity such as seawater which is opaque to radar waves. Pure ice and snow has negligible conductivity so provides an ideal medium for radar sounding.

Table 1. *Relative permittivity, conductivity, velocity and attenuation for a variety of materials found in glacial environments.*

Material	**Relative permittivity ε_r**	**Conductivity σ (mS/m)**	**Velocity v (m/ns)**	**Attenuation α (dB/m)**
Air	1	0	0.300	0
Pure ice	3.15	0.01	0.169	0.01
Fresh water	80	0.5	0.033	0.1
Sea water	80	$3x10^3$	0.010	10^3

A common configuration of a radar system consists of two antennas; one transmitting and the other receiving. These can be two separate antennas (bistatic), or the same antenna which transmits a signal then switches to receiving mode (monostatic). In this study the radars used have a bistatic arrangement. The shape of the antenna controls the radiation

pattern which is carefully designed to ensure that maximum power is directed towards the target.

In the case of ice-penetrating radars, the transmitting antenna emits an EM wave directed downwards into the surface. The velocity (v) of the wave depends on the relative dielectric permittivity (ε_r) of the medium through which it travels;

$$v = \frac{c}{\sqrt{(\varepsilon_r)}} \tag{4.1}$$

Where c is the speed of radar in a vacuum (0.3 m/ns), and $\varepsilon_r = \varepsilon/\varepsilon_0$ where ε is the permittivity of the ice and ε_0 is the free space dielectric constant. In the case of snow and ice the relative permittivity is related to density (ρ) by the equation (Kovacs et al., 1995);

$$\varepsilon_r = (1 + 0.000845\rho)^2 \tag{4.2}$$

Density contrasts in snow, firn and ice can be used to identify internal layers which are formed during accumulation, redistribution, and melting events. Annual layers may also be identifiable as there can be significant changes in firn density during the summer melt season. Layers can also be caused by a change in chemical composition (e.g. a volcanic ash layer increasing the acidity), or crystal orientation (Siegert, 1999). As all of these events occur at specific times, layering within the ice column normally represent isochrones.

When the radar wave encounters a change in permittivity, some of the energy is reflected back to the surface and is recorded by the receiving antenna (Figure 7). The power of the reflected signal depends on the reflection coefficient which is the ratio between the amplitude/power of the reflected and incident waves at the boundary. This is typically of the order -2 dB for the ice shelf base, and in the range -60 to -90 dB for internal layers (Brennan et al., 2014). The reflections from the upper layers are the strongest and can over-saturate the receiver which results in a clipped signal which cannot be interpreted. The extent of this clipping largely depends on the antenna frequency. As the wave propagates downwards the wavefront spreads out so the energy of the signal which is travelling directly downwards decreases. As a result, the reflected signal becomes weaker and is eventually exceeded by the background noise associated with the receiver. The signal-to-noise ratio

(SNR) is a measure of the signal power compared to the background noise and can be used to determine the maximum depth to which the radar can successfully sound.

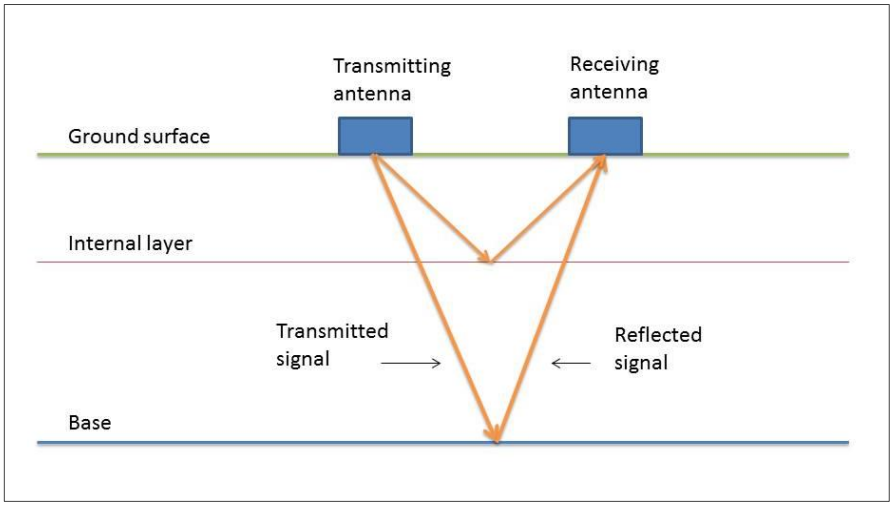

Figure 7. *The basic principles of ice penetrating radar on an ice shelf. A transmitter sends a signal into the ice which is reflected off internal layers and the base of the ice shelf. The reflected signal is recorded by the receiver. Close to the surface the radar wave has travelled on an angular path from the transmitter to the receiver, however, at depths greater than a few antenna separations the received signal is assumed to have come from a radar with both antennas located at the midpoint between the actual antenna positions.*

The energy (E) of the transmitted wave depends on the output power (P) and pulse duration (t);

$$E = Pt \tag{4.3}$$

Most ground-based radar have low radiated power as they are constrained by international regulations, such as those developed for GPR by the European Telecommunications Standard Institute.

The recorded radar signal is generally a function of two-way-travel time (TWT), which is the time it takes for the signal to propagate down to the target and back to the receiver at the surface, and amplitude which is a measure of the received power. TWT is converted to depth (d) by using the velocity of EM waves in the subsurface which depends on the material properties. In pure ice v=0.169 mns^{-1} but in fresh snow and firn, which has significantly lower densities, the velocity is approximately 0.22 mns^{-1}.

$$d = \left(\frac{TWT}{2}\right) v \tag{4.4}$$

To accurately calculate depth either a variable velocity model or correction for the velocity in firn needs to be applied, both of which require an understanding of the density profile and depth to the firn-ice layer.

The standard range resolution (ΔR) is the minimum vertical distance between two targets for the radar to be able to resolve them as separate objects and can be calculated from;

$$\Delta R = \frac{c}{2B\sqrt{\varepsilon_r}} \tag{4.5}$$

Where B is the radar bandwidth. From equation (4.1) this can be expressed as;

$$\Delta R = \frac{v}{2B} \tag{4.6}$$

In practice, there is a deviation from the theoretical resolution of a factor of approximately 1.39 which has been derived empirically (Jol, 2009).

4.1.2 Ground Penetrating Radar

There are two main categories of ground penetrating radar (GPR): impulse and continuous wave. Most GPR systems, including those used in this study, are based on the impulse technique. In this thesis the term GPR applies to the impulse radar which was used on the SMIS.

Impulse GPR is a type of ultra-wideband radar where pulses, with a central frequency (f_c), are transmitted with a very short duration to obtain a large bandwidth. For most GPR systems $B = f_c$, and from equation (4.6) the range resolution is;

$$\Delta R = \frac{v}{2f_c} \tag{4.7}$$

Which, using the relationship; $v = f\lambda$, can be rearranged as;

$$\Delta R = \frac{\lambda}{2} \tag{4.8}$$

The short pulse duration means that GPR is ideal for collecting line data where the radar is travelling across the surface while simultaneously taking measurements called 'traces'. GPR is mainly used in this manner to image the subsurface as a 2 dimensional 'slice' by aligning traces next to each other to create a 'radargram'.

The depth to which the signal can penetrate is controlled by transmitted energy and the attenuation (α). As the average power is low and pulse duration is short (approximately 1/f), to obtain a large bandwidth, GPR signals are of relatively low energy. Total attenuation is the sum of scattering attenuation and ohmic attenuation ($\alpha_{\text{total}} = \alpha_{\text{scattering}} + \alpha_{\text{ohmic}}$). Ohmic attenuation is a property of the medium which depends on the dielectric permittivity, conductivity, and magnetic permeability (μ);

$$\alpha_{ohmic} = \frac{1}{2}\sigma\sqrt{\frac{\mu}{\varepsilon}} \tag{4.9}$$

Scattering attenuation is caused by small heterogeneities which lead to a decrease in the electric field (E) with distance (r); $E = E_0 e^{-\alpha_s r}$ where the scattering attenuation coefficient $\alpha_s \propto f^4$. In snow and ice, ohmic attenuation is low (Table 1) and the total attenuation is dominated by scattering attenuation (Jol, 2009). As a result, the penetration depth is strongly influenced by the frequency. Attenuation increases (and as a consequence, penetration depth decreases) with frequency but range resolution decreases. Operating frequency is a trade-off between these factors and must be carefully chosen. High frequency radar (100's-1000's MHz) are commonly used to examine near surface features such as internal layers in the firn, and low frequency (<100 MHz) for measuring ice thickness.

4.1.3 Autonomous phase sensitive radar principles

As discussed in section 2.4.1, ApRES is a high accuracy radar under development by the BAS. ApRES radar is based on frequency modulated continuous wave (FMCW) radar which has been successfully used in snow research for over 30 years (Marshall & Koh, 2008).

Unlike GPR which transmits a pulsed signal at a single frequency, ApRES transmits a sinusoidal tone (chirp) that linearly sweeps from 200 MHz to 400 MHz during a 1 second interval. The reflected signal is received a short time later so its frequency is always lower than what is being simultaneously transmitted (Figure 8).

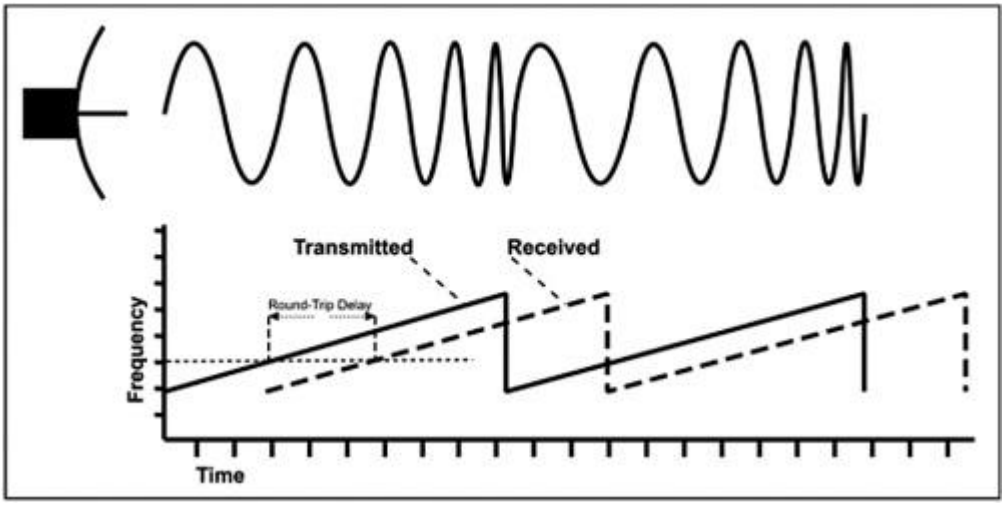

Figure 8. *Basic schematic of ApRES operation. The ApRES emits a chirp with increasing frequency over one second, while simultaneously recording the reflected signal which will have a slightly lower frequency.*

The difference in frequency is linearly dependent on the depth to the reflector. The influence of the transmitted signal can be removed from the received wave and the resulting de-ramped, frequency difference signal can be recorded. The de-ramped frequency (f_d) is given by;

$$f_d = \frac{2BR\sqrt{\varepsilon_r}}{Tc} \tag{4.10}$$

where B is the frequency bandwidth (200 MHz), R is the range to the target in metres, T is the pulse duration (1s) and ε_r and c are the relative dielectric permittivity (typically 3.15 in ice) and the speed of light (0.3 m/ns) respectively (Brennan et al., 2014).

The standard range resolution from equation (4.6) is approximately 43 cm, however, the phase of the transmitted wave is also carefully measured and can be tracked through phase sensitive processing techniques which increases the resolution to millimetre precision (Brennan et al., 2014). It is with this high precision that ApRES can be used to measure the range to layers with very high accuracy which allows it to be used for measurements of strain and basal melting which can be on the order of mm/yr.

The ApRES has a constant power output of 100 mW, which integrated over the one second chirp gives the total energy transmitted per chirp of 0.1 J which is significantly higher than that of the GPR. The SNR is directly proportional to the chirp length and transmitted power, and inversely proportional to the noise factor associated with the receiver, which is low for the ApRES (Brennan et al., 2014). In addition, by taking the average of many chirps per

measurement (also called a ‘burst’) the SNR is further improved. Due to a much higher output energy and larger SNR, ApRES can penetrate significantly further than GPR operating at a similar frequency. The theoretical maximum range to which the ApRES can reliably measure is 2 km in pure ice (Brennan et al., 2014), and it has successfully measured ice thickness up 1940 m on the Rutford Ice stream (Jenkins et al., 2006).

The long measurement duration means that ApRES is not an efficient way to capture line surveys, rather it is designed to take repeated stationary point measurements. This can either be achieved by leaving the ApRES in the field to capture a time series, or taking an initial measurement and returning to the same spot a period of time later and taking a repeat measurement allowing for multiple sites to be visited with one radar system.

4.2 Glaciological Measurements made with Radar

In this thesis, radar were used to investigate a number of ice shelf properties that are described in this section.

4.2.1 Ice thickness

Ice thickness is measured in two ways; along crossing grid lines on the SMIS using GPR, and at single points on the SMIS and RIS with ApRES. To remain consistent, TWT is converted to depth using the velocity of radar in pure ice and then a firn correction is applied for both radar types.

The reflection of the ice shelf base is easily identifiable as the dielectric contrast between ice and sea water greatly exceeds that between layers of ice. In both GPR and ApRES radargrams it is clearly visible as a large peak in the received power.

4.2.2 Firn correction

The velocity of radar waves through ice is directly related to its density (section 4.1), however, the conversion of TWT (equation (4.4)) to depth usually only takes a single radar velocity value (normally that in pure ice ($v=0.169$ ms^{-1})) which underestimates the true ice thickness. To compensate for this, a radar firn correction is applied. Using climate modelling to estimate the value of the firn correction requires knowledge of many different parameters which change over spatial and time scales. Often these parameters are difficult to constrain and the resulting errors can dominate the uncertainty. If an in-situ density profile can be obtained (e.g. from a snowpit or firn core), additional data (e.g. accumulation, weather, and temperature) is not required as the density profile will better reflect all local processes which influence firn density.

When an ice shelf consists of a mixture of pure ice, snow crystals and air, as is commonly the case, it is plausible to imagine that if the firn were compressed to the density of pure ice, the ice thickness (Z) would then be represented by a column of ice (with thickness Z_i) and an air thickness layer (Z_{air}). This can be expressed as;

$$Z = Z_i + Z_{air} \tag{4.11}$$

It is easier to apply a firn correction using air layer thickness than it is to apply a radar velocity derived from average density. Most of the air is present in the upper firn layers, so

Z_{air} depends largely on accumulation and densification. The mean density not only relies on firn processes but on ice thickness as well. In addition, the radar velocity calculated for uncorrected ice thickness, must then also be corrected for the modified thickness. Strictly speaking, if the ice column does not consist of pure ice and air only, then Z_{air} is only an apparent air layer thickness (Z_{air}'). For example, if there was a layer of marine ice with thickness Z_{mar} and $\rho_{mar} > \rho_{ice}$ present, the apparent air thickness is;

$$Z'_{air} = Z_{air} + Z_{mar} \tag{4.12}$$

However, the average density of marine ice is approximately 925 kgm^{-3} (Horwath et al., 2006) so only slightly exceeds that of pure fresh ice (ρ_i=917 kgm^{-3}). Thus, $Z_{mar} \approx 0.02\ Z_{air}$ so only becomes significant when the marine ice layer is 100s' of metres thick. Therefore, in this study, the influence of the marine ice on the air layer thickness is assumed negligible given that the maximum expected marine ice thickness is on the order of tens of metres (Neal, 1979).

Air layer thickness derived from modelling or a snowpit is then used to calculate the radar firn correction (ΔZ) to account for the changing velocity in the ice column using;

$$\Delta Z = \left(\frac{n_i - 1}{n_i}\right) Z_{air} \tag{4.13}$$

Where, the pure ice refractive index n_i=1.78 (Jenkins and Doake 1991).

In the case where density in the firn layer is known, and a steady state density profile is assumed, an exponential model of the form;

$$\rho(z) = \rho_i - (\rho_i - \rho_s)e^{-Cz} \tag{4.14}$$

can be fitted to the data with local surface snow density ρ_s, and densification parameter C (Cuffey & Paterson, 2010). The resulting air layer thickness is estimated using;

$$z_{air} \approx \frac{\rho_i - \rho_s}{\rho_i C} \quad (4.15)$$

In this study, multiple radar firn corrections are calculated using the methods outlined above and are compared with one another in order to apply the best correction to the different field areas.

4.2.2.1 Firn correction using modelled air layer thickness

In order to remain consistent between ice thickness measurements, a firn correction based on the same air layer thickness (Ligtenberg et al., 2011) as that used by Griggs & Bamber (2011) is applied to the ApRES sites on the RIS. By using the same firn correction, any discrepancies in ice thickness are not a result of variations in the firn models. This correction uses an expression for firn densification that is tuned to fit observations. The model was forced by the output of surface mass balance, surface temperature and wind speed from a regional climate model (RACMO2/ANT) during the 30 year period from 1979 to 2009 (Ligtenberg et al., 2011). It was run with a horizontal resolution of 27 km. The thickness of the firn column, taken to be the depth to pore close-off at ρ=830 kgm^{-3}, is around 40-50 m on the RIS (Ligtenberg et al., 2011), which is equivalent to 16 m of air if the firn column was compressed to the density of ice.

4.2.3 Marine ice thickness

The strength of the reflection of a radar wave at a dielectric boundary is largely dependent on the magnitude of the permittivity contrast. Strong reflections indicate a sharp contrast between layers. Weak reflections represent subtle changes in permittivity. In this case this indicates a transition zone between the ice shelf and the ocean. This may be the result of entrainment of sediment in the lower ice shelf; or indicates the presence of a marine ice layer. Radar waves are unable to penetrate a marine layer due to its salinity, causing high absorption of energy. Therefore, radar systems can only detect the boundary between meteoric and marine ice, which may not be representative of the true ice thickness.

While radar cannot directly measure marine ice thickness, freeboard measurements derived from satellite altimetry can be converted to ice thickness using the assumption that the freely floating ice is in hydrostatic equilibrium. The surface height relative to sea level, Z, is related to ice thickness, H, using the equation:

$$Z = \frac{H(\rho_w - \rho_i)}{\rho_w} \tag{4.16}$$

Where ρ_w and ρ_i are the average densities of seawater and ice respectively. The standard density of pure meteoric ice is 917 kgm^{-3} with impurities causing variations of ±5 kgm^{-3} (Fricker et al., 2001).

A layer of marine ice contributes to ice thickness by increasing the buoyancy force and thus the freeboard. In this case, thickness derived from freeboard will be greater than that measured with radar. Following Fricker et al. (2001), the marine ice thickness can be calculated by subtracting the radar thickness from the freeboard thickness. An ice shelf thickness map derived from data collected by the radar altimeter on the ERS-1 satellite between 1994-95 (Griggs & Bamber, 2011) that is the basis of the widely recognised ice shelf thickness for BEDMAP-2 (Fretwell et al., 2013) is compared to thickness measured with the ApRES on the RIS.

4.2.4 Strain thinning/thickening

As described in section 2.3.5, strain is an important component of understanding the mass balance of an ice shelf. Making high accuracy measurements of basal melting requires knowing the strain rate to an equivalent accuracy. Here, vertical strain is calculated on the RIS from satellite derived velocity data and also measured directly with ground-based ApRES radar.

There are a number of assumptions that can be made when calculating vertical strain;

(a) Ice is incompressible in ice shelves (Cuffey & Paterson, 2010). This does not apply to firn but, as will be shown, the ApRES operates below the firn layer and thus this assumption holds valid;
(b) Ice shelves deform uniformly in the vertical domain by compression and thinning in response to pure shear, such that the velocity is constant through the ice column (Cuffey & Paterson, 2010);
(c) Any effects of confining forces at the sides and changes in the stress regime where flows converge and diverge are reflected in the ice velocity which is used to calculate strain in the middle of the ice shelf;

(d) The ice shelf has constant density. While this is not entirely accurate, as will be shown, the uncertainties derived from using satellite velocity measurements are far greater than those that contribute from the firn. Measurements of strain made with radar are made below the firn layer where the density changes gradually with depth and the variation in velocity is a maximum of 4.3% from that in pure ice.

4.2.4.1 Vertical strain from velocity

Following from assumption (b) above, the velocity of the ice at the surface is representative of the motion of the ice in the column directly beneath. Thus, if surface velocity is known it can be used to calculate vertical strain using the method described below.

A block of ice moving in an ice shelf flows with velocity **u** which has three components (**u**, **v**, **w**). The spatial change in velocity determines the rate of deformation, otherwise known as the strain rate (ε̇). The strain rate has nine individual components given by;

$$\dot{\varepsilon}_{jk} = \frac{1}{2}\left[\frac{\partial u_j}{\partial x_k} + \frac{\partial u_k}{\partial x_j}\right] \tag{4.17}$$

Where j and k stand for x, y, or z; and $x_x = x,\ x_y = y,\ x_z = z$. Thus, for example,

$$\dot{\varepsilon}_{xy} = \frac{1}{2}\left[\frac{\partial u}{\partial y} + \frac{\partial v}{\partial x}\right] \tag{4.18}$$

$$\dot{\varepsilon}_{xx} = \frac{\partial u}{\partial x} \tag{4.19}$$

The components $\dot{\varepsilon}_{xx}, \dot{\varepsilon}_{yy}, \dot{\varepsilon}_{zz}$ quantify the stretching or compression parallel to the x, y and z axis respectively. The first invariant of the strain rate is symbolized $\dot{\varepsilon}_I$ and is the fractional rate of the volume change of the deformed ice;

$$\dot{\varepsilon}_I = \dot{\varepsilon}_{xx} + \dot{\varepsilon}_{yy} + \dot{\varepsilon}_{zz} = 0 \tag{4.20}$$

In the case of ice $\dot{\varepsilon}_I = 0$, as ice is incompressible. Therefore, strain rate in one axis can be calculated providing velocity is known along the other axes.

In this thesis, vertical strain is calculated from horizontal velocity measured by satellites for NASA's MEaSUREs (Making Earth System Data Records for Use in Research Environments) program (Rignot et al., 2011b). This is the first high-resolution mosaic of ice motion in Antarctica. Velocity is calculated in both east-west (x) and north-south (y) directions from multiple interferometric synthetic-aperture radar systems. Most of the data were collected during the International Polar Year (2007-2009) and have 900 m horizontal resolution (Rignot et al., 2011b).

4.2.4.2 Vertical strain from phase sensitive radar

The phase sensitivity of the ApRES means that it can detect internal layers with a very high accuracy, which allows it to be able to directly measure vertical strain. A detailed description of the phase processing of ApRES data to calculate strain rate and basal melting is given in Brennan et al. (2014). Here only the background theory and basic concepts are discussed.

Phase sensitive radar can be used to measure strain and melting by considering the mass balance of the column of ice directly beneath the radar. The mass balance equation can be expressed as;

$$\nabla \cdot \boldsymbol{u} - \dot{m}_s \frac{\partial}{\partial z}\left(\frac{1}{\rho}\right) = 0 \tag{4.21}$$

Where **u** is the three-dimensional velocity vector (u, v, w), $\dot{m}_s$ is the surface mass flux, and ρ is the firn/ice density (Jenkins et al., 2006). Integrating this equation between an internal reflector and the ice shelf base gives;

$$\frac{DH_e}{Dt} + H_e\left(\frac{\partial \bar{u}}{\partial x} + \frac{\partial \bar{v}}{\partial y}\right) - \frac{\dot{m}_s}{n_i}\left(\frac{1}{\rho(h_u)} - \frac{1}{\rho_i}\right) - \frac{\dot{m}_b}{\rho_i} = 0 \tag{4.22}$$

Where H_e is the effective ice thickness from converting TWT to depth using the radar velocity in solid ice, the unknown basal mass flux is $\dot{m}_b$, t represents time, $n = \sqrt{\varepsilon_r}$ is the refractive index which is directly proportional to density (equation (4.2)). Overbars indicate the depth averaged, and the subscript 'i' refers to solid ice. The term $\rho(h_u)$ is the density at the depth of the internal reflector. If this lies in solid ice the third term on the left, which

is firn compression, is zero and the change in effective thickness is simply a combination of strain thinning/thickening and basal melting/freezing (Figure 9).

This same equation can be applied to two internal reflectors below the firn layer. In this case the third and fourth terms are zero which gives an expression for strain thinning/thickening (Jenkins et al., 2006);

$$\left(\frac{\partial \bar{u}}{\partial x} + \frac{\partial \bar{v}}{\partial y}\right) = -\frac{1}{H_e}\frac{DH_e}{Dt} \tag{4.23}$$

Which combined with equation (4.22) gives a vertical strain rate of;

$$\varepsilon_{zz} = \frac{1}{H_e}\frac{DH_e}{Dt} \tag{4.24}$$

Strain can be calculated from strain rate by fitting a model to strain rate with depth. On ice shelves with flat topography and far from the grounding line the strain rate is constant with depth (Nicholls et al., 2015), so a linear strain model is fitted through the ice column.

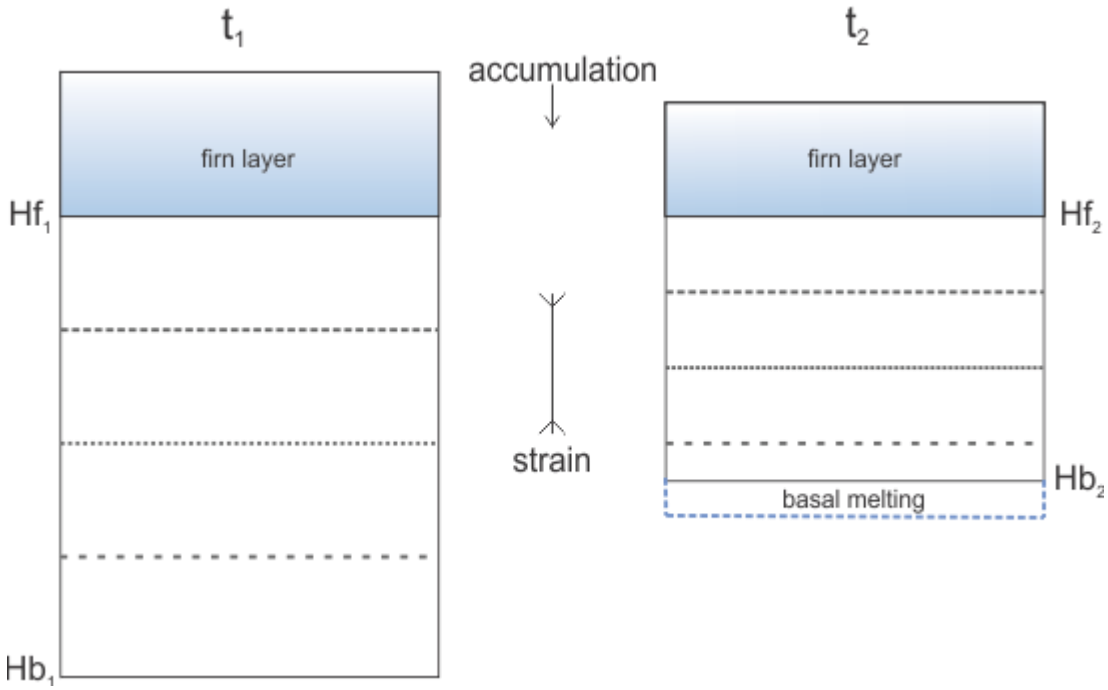

Figure 9. *Schematic of a cross section of an ice column at two times (T1 and T2). The distance between Hf and Hb are measured at both times with ApRES. The difference is a result of strain thinning/thickening and basal melting/freezing. Strain is calculated by comparing the relative motion between internal layers (grey dotted lines) from which basal melting can be deduced. Any processes that influence the firn are neglected as the radar identifies layers beneath the firn layer.*

4.2.5 Basal melting/freezing from radar

By using equation (4.22) the basal melt rate can be derived by taking repeat radar measurements at the same location and removing the strain component from ice thickness changes. If multiple internal reflectors in the solid ice are not clearly identifiable, strain can be determined from other methods and manually defined in the basal melting equations. Further detail about the processing of ApRES radar to calculate basal melting can be found in Brennan et al. (2014).

5 FIELD METHODS AND DATA PROCESSING

This chapter is split into two sections. The first describes the set-up and data acquisition with the GPR and ApRES radar at both field sites, and the second is a description of other measurements made in the field which were used to help interpret and analyse the radar data.

5.1 RADAR MEASUREMENTS

5.1.1 Ground Penetrating Radar

In this research a commercial PulseEKKO PRO GPR system is utilised (https://www.sensoft.ca/products/pulseekkopro/overview/). This instrument is capable of operating at nominal frequencies between 12.5 MHz and 1 GHz, with varying vertical resolutions, for deep ice and shallow reflectors in snow. GPR data is collected on the SMIS using three antennae sets at frequencies of 25, 500 and 1000 MHz For this work, the GPR system operating at 25 MHz is used to map the ice shelf base and measure ice thickness, whereas the two higher frequency radar are used to examine internal layers in the firn.

There are a number of system parameters which need to be defined for data acquisition (Table 2);

- Time window: How long a single trace will be measured for. The longer the time window the deeper the radar will 'see';
- Depth to measure: An approximate value based on the time window and the velocity of the radar wave in ice (0.169 m/ns) for the 25 MHz and in snow (≈0.22 m/ns) for the 500/1000 MHz radar. This has to be chosen carefully to ensure that it is sufficiently long to capture reflections, but not too long in order to maintain efficiency in data collection;
- Sampling rate: The GPR samples the received signal at a given temporal sampling interval so that the recorded signal is amplitude at equally spaced time intervals. This is set to a default value depending on the frequency to avoid over and under-sampling;
- Antenna separation. The distance between the two antennae as they are moved along the survey line;

- Step size. The distance between traces, which is estimated based on the velocity at which the radar is moved along the surface and the time window. More accurate distances are provided by the GPS positions;
- Trigger method determines how often the transmitter will be triggered to emit a signal.

Table 2. *The values of the parameters used for GPR data acquisition. Trigger method is set to free run which means that the system collects data continuously. This method is best used when data is either collected at a constant velocity or a GPS is used to capture positional information as is the case here.*

Frequency (MHz)	**25**	**500**	**1000**
Time window (ns)	4960–6000	320	108
Depth (m)	420–508	35	12
Sampling interval (ns)	3.2	0.2	0.1
Antenna separation (m)	3	0.225	0.15
Step size (m)	1	0.05	0.05

The physical set-up and operation of the high and low frequency radar during data acquisition are described separately below.

5.1.1.1 25 MHz GPR set-up and operation

The two 4 m long 25 MHz antennas are placed parallel to each other in a purpose-built sledge with a horizontal separation of 3 m. To minimise external interference, the GPR sledge is attached to a wooden sled which is towed slowly behind a snowmobile with the antennae moving parallel to the direction of travel (Figure 10).

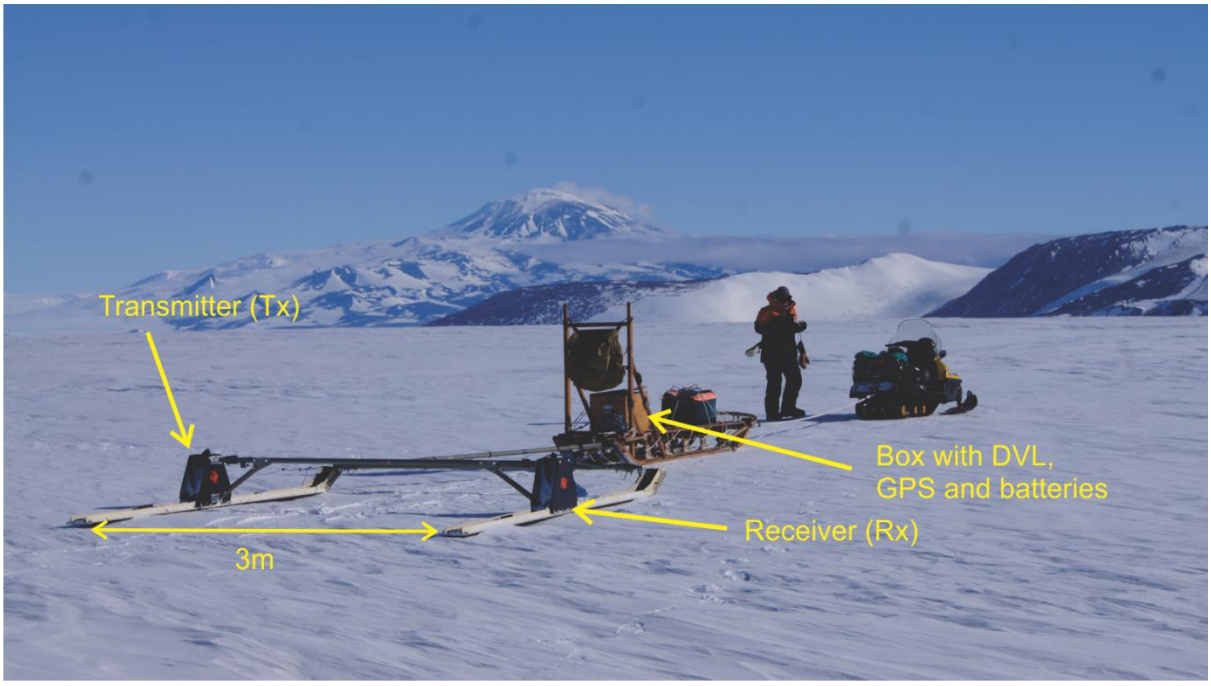

Figure 10. *Set up of the 25 MHz GPR system. The digital video logger (DVL) and a Trimble GEO-XH GPS system are mounted on the wooden sled in a box, with the batteries to power the DVL. There is a horizontal offset of 5.75m between the GPS and the middle of the two antennae (Rx and Tx) which are connected to the DVL with fibre optic cables.*

5.1.1.2 500/1000 MHz GPR set-up and operation

The high frequency antenna requires a smaller and more compact GPR set-up. The antenna footprint is 0.15 m x 0.15 m, and 0.08 m x 0.08 m for the 500 MHz and 1000 MHz systems respectively. These are shielded to avoid external interference and are designed to ensure that maximum power is directed downwards. In this configuration, the radar is dragged behind an operator on skis (at approximately 4 km/hr) with the DVL, battery and GPS in a backpack (Figure 11).

Figure 11. *Set up of the 1000/500 MHz GPR. The two antennae are the yellow boxes on the sled which is connected directly to the DVL with coaxial cables. The entire system is powered with a single 12V battery.*

5.1.1.3 *Data acquisition*

To examine ice thickness and morphology, the 25 MHz radar was dragged on a grid which extended across the SMIS grounding zone at the southern edge of White Island in November 2014 (Figure 2). The grid is separated into two zones: central and outer. The central zone is the main focus of this study and has gridline spacing of 250 m. This central zone is 2 km wide and up to 4.5 km long, with the long axis orientated transverse to the grounding line (Figure 12). The outer zone has 1 km grid spacing and extends 13 km along the grounding zone; however, technical difficulties meant that data acquisition is sporadic in this zone (Figure 12). A travel speed of ≈15 km/hr allowed traces to be collected approximately every metre with accurate location simultaneously being recorded with the GPS. In total, ≈70 km of 25 MHz GPR traces were collected.

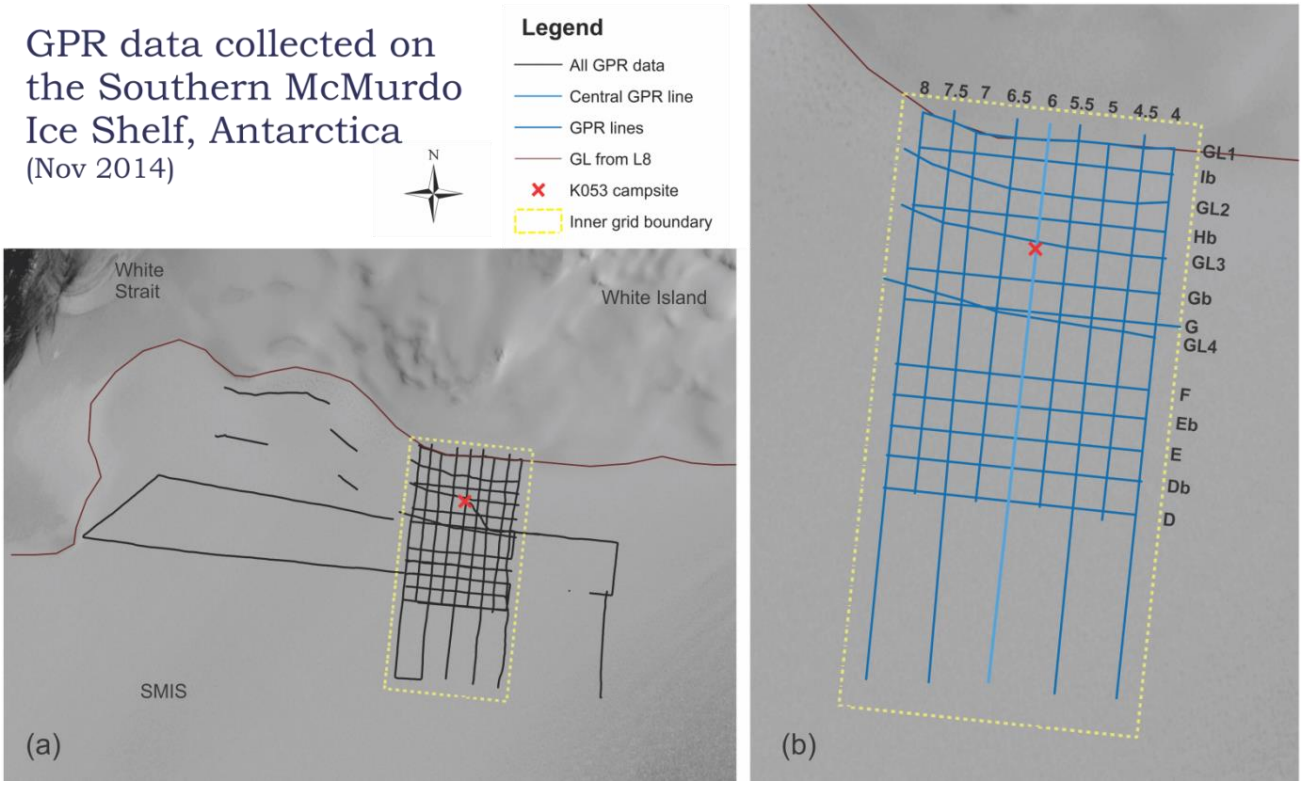

Figure 12. *Map showing all of the GPR traces collected on the SMIS (a), and those collected within the 'central' grid (b). 25 MHz data were collected on all the lines displayed, but 500/1000 MHz data were only collected along line 6 (light blue in (b)). The labelling of traces is identical with that used in the field and this nomenclature is consistent throughout this thesis. Gaps in the data are due to faulty equipment. The lines GL1, GL2, GL3 and GL4 are based on interferometric fringes. The line GL1 also corresponds to the grounding line picked out from the break in slope (point Ib in Figure **1**) visible in the LANDSAT 8 (L8) base image.*

To examine internal structure within the upper firn layers, high frequency data were only collected along the central north-south line in the inner zone (line 6 in Figure 12). These lines extended 3 km from the grounding zone and are taken along the same track as the equivalent 25 MHz line.

5.1.1.4 GPR data processing

All GPR data processing is performed in the commercial seismic and GPR software package Reflexw (http://www.sandmeier-geo.de/reflexw.html). To ensure consistency, the same sequence of processing steps is used for all profiles (Figure 13), but is applied manually to account for variations between profiles.

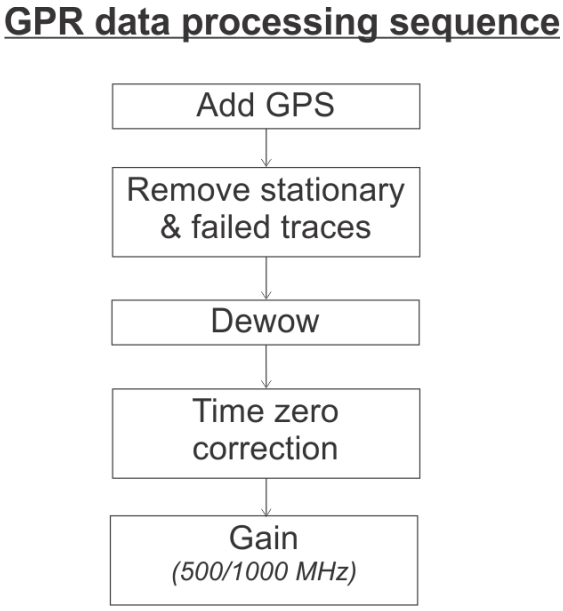

Figure 13. *The sequence of steps used during processing of the GPR data.*

The first step is to incorporate the GPS data into each radar trace in Reflexw. The second step is to remove traces where the receiver failed to record a signal or when multiple identical traces were recorded while the GPR was stationary. The 'dewow' tool was used with a 2 period time window to remove the low frequency oversaturation signal near the surface. This is followed by a shift in time zero so that the first reflection is aligned with the surface.

A gain function is not applied to the 25 MHz frequency data as the base reflection is sufficiently strong to be easily identified. Gain is applied to the high frequency radar data to enhance reflectors at depth. Due to the range spreading loss the power per unit area decreases at a rate of $\frac{1}{d^2}$, where d is the depth from the surface. As power is proportional to amplitude squared, the decrease in amplitude with depth is corrected by applying a linear gain.

The base of the ice shelf is identified in Reflexw using the 'pick' tool and is exported to allow for spatial analysis and visualisation in ArcGIS. Picking of layers is done manually

by selecting the first strong return from the base. This is to remain consistent with the time-zero correction which was also applied using the arrival of the first reflection.

5.1.2 Phase sensitive radar data acquisition and set up

The ApRES system has a simple and lightweight set-up. There are two identical antenna of the skeleton design described by Nicholls et al. (2015). During operation one acts as a transmitter and the other as a receiver and they have a separation of ≈9.5 m. The configuration is designed in such a way that the maximum power is directed downwards (K. Nicholls, personal communication, September 16, 2015) (Figure 14).

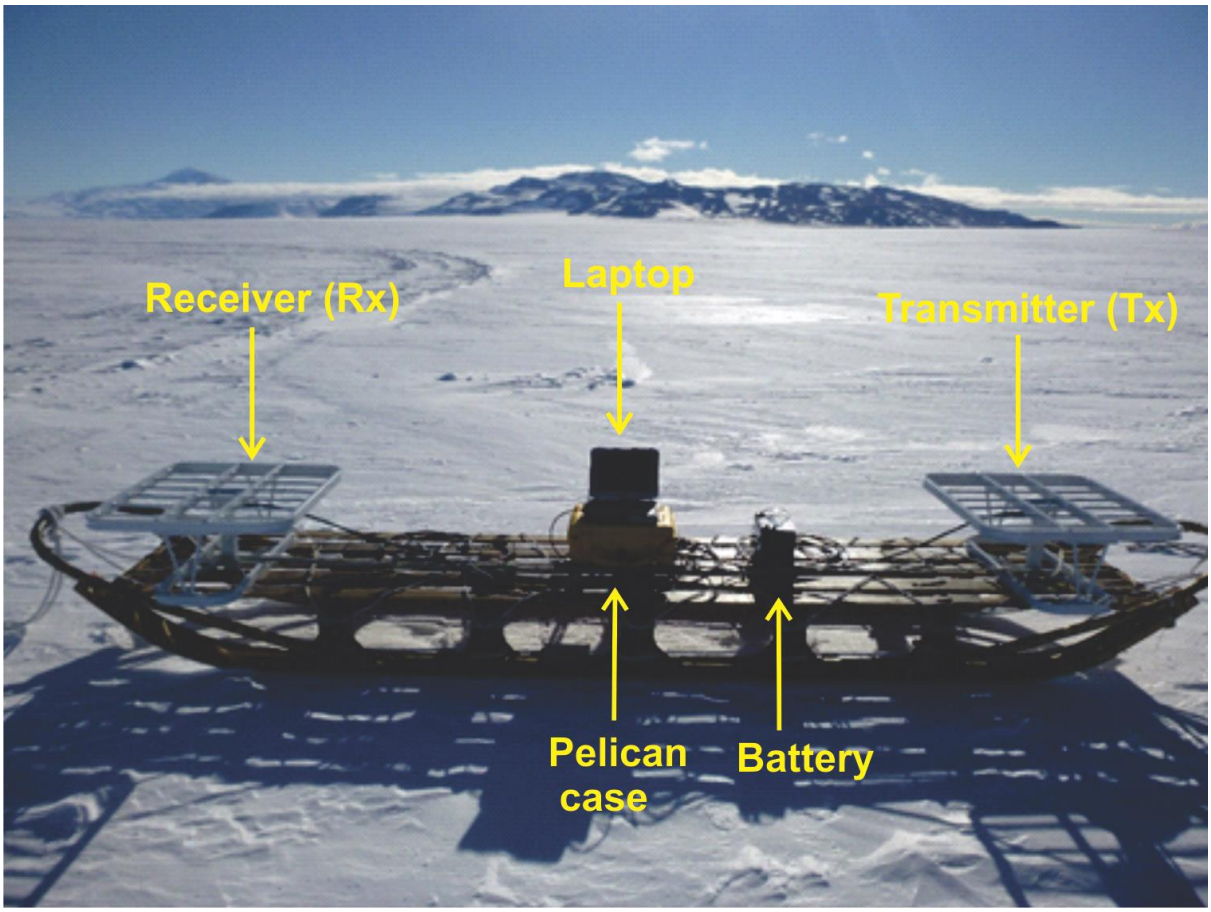

Figure 14. *The set up of the ApRES system. The electronics and GPS are housed in the pelican case. The laptop is used to control the radar via a web browser in attended mode. To take a measurement the two antenna are placed on the ground in the orientation shown. Position is recorded using an internal GPS. The entire system is powered with a single 12 V battery.*

There are two modes of ApRES operation: attended and unattended. In attended mode the user communicates with the radar via an Ethernet cable. Operation of the radar is then controlled through a web browser interface where the user can manually adjust survey parameter values to ensure that the system runs optimally. In this mode, data can be downloaded directly onto the computer in conjunction with saving it to an internal SD card.

In unattended mode, the radar operates automatically, with settings defined through a configuration file on the SD card. In this study all measurements are made in attended mode.

The transmitted wave has a constant amplitude and power (100 mW), but a combination of an adjustable attenuator in the receiver and low frequency gain amplifier ensures that the recorded signal is sufficiently strong without exceeding the thresholds of the circuit (Nicholls et al., 2015). Attenuation and gain are defined manually by the user and vary based on the environment in which measurements are being made. The other parameter which is also user defined is the number of chirps per burst, where a burst is a single measurement and is the average of multiple sub-measurements called chirps. A description of the sites that were measured and the values of these parameters are in appendix B.1. Other operational parameters are defined in the configuration file and were kept at their default values.

5.1.2.1 ApRES on the Southern McMurdo Ice Shelf

In order to compare and contrast thickness measurements between the ApRES and 25 MHz GPR radar, a number of ApRES measurements were made along the central grid profile on the SMIS. In total 25 points were measured at roughly 100-150 m intervals along this line (Figure 15). These measurements were not repeated, so strain and melt cannot be calculated from them.

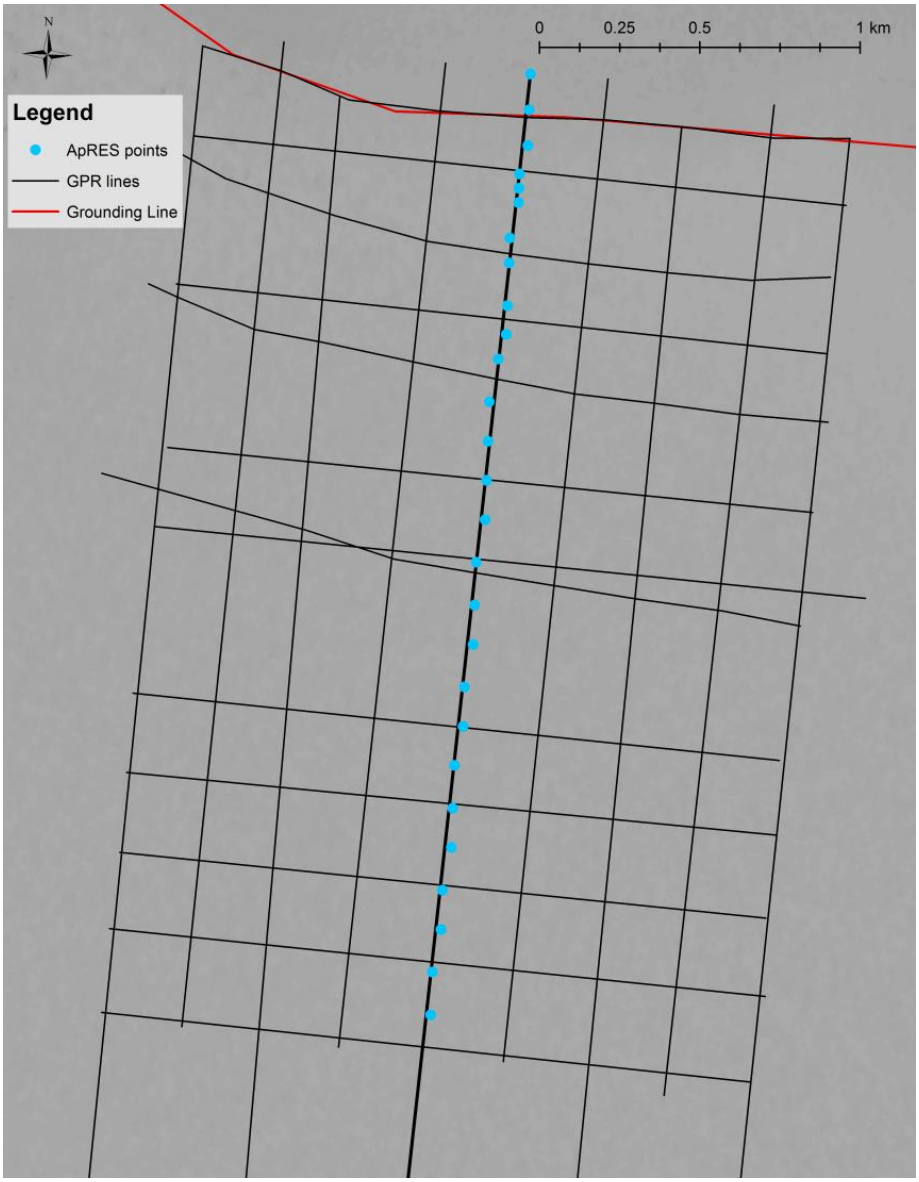

Figure 15. *Distribution of ApRES points (blue) on the SMIS relative to the GPR traces (black lines).*

5.1.2.2 ApRES on the Ross Ice Shelf

Phase sensitive radar data was collected on the RIS during November 2015 during Antarctica New Zealand event K061. The field camp was located approximately 350 km south of Scott Base along the South Pole Overland Traverse (SPOT) road (Figure 16).

In total 21 sites were selected for repeat ApRES measurements; eleven measurements were made approximately every 25 km along the SPOT road; and 10 sites within a 20 km radius of the camp were visited (Figure 16). Two measurements were made at each site at the beginning and end of the field campaign, with the time between measurements ranging from 5.8 to 14.9 days. See Appendix B.1. for further information.

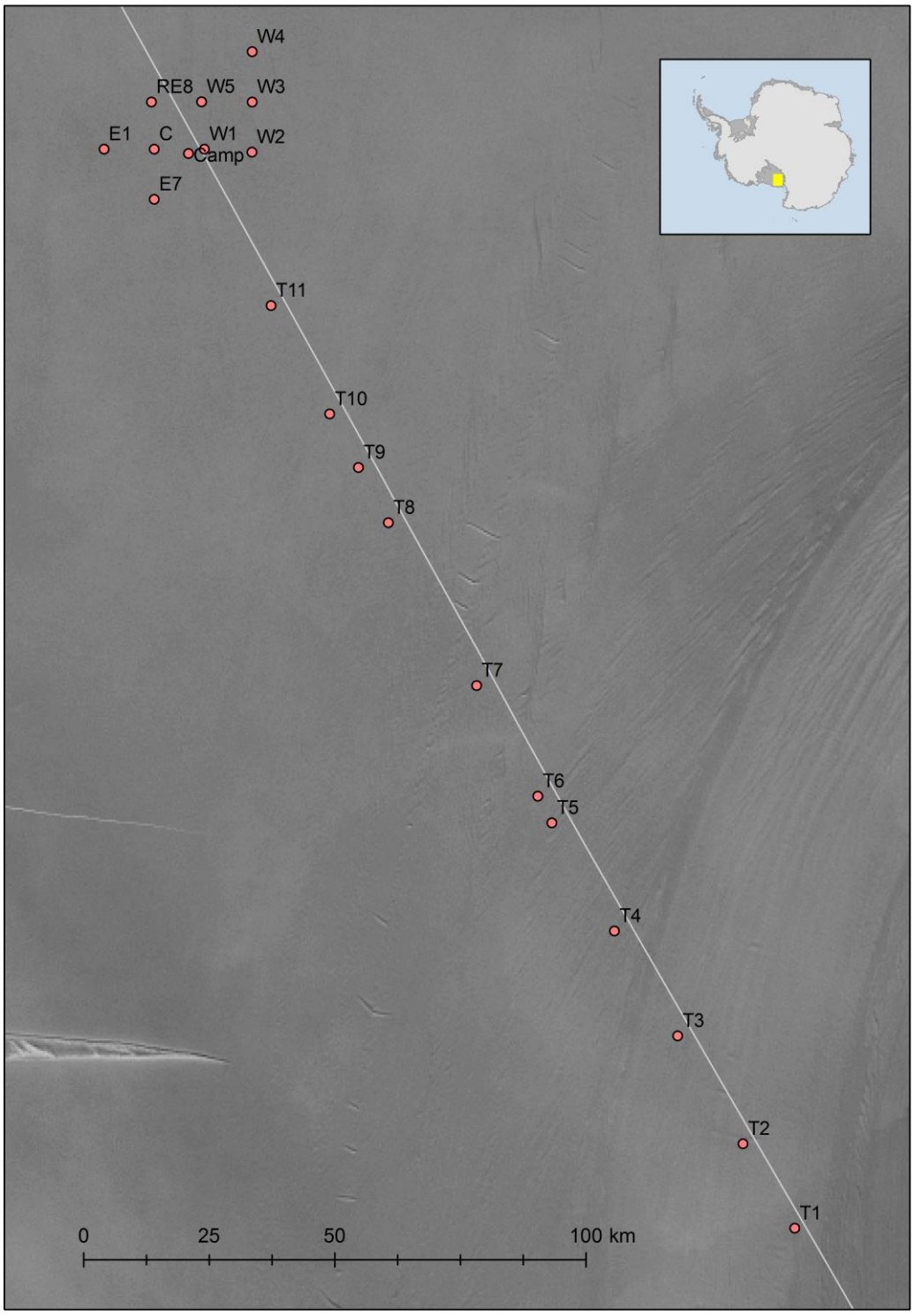

Figure 16. *The names and locations of the 21 ApRES sites visited on the RIS. The white line is the South Pole Traverse Route. The map is orientated towards the south so the Transantarctic Mountains are to the right (west) of the sites.*

The ApRES was configured manually for site in order to optimise the signal-to-noise ratio. Identical settings were used for the repeat measurements to ensure data are comparable. The received signal of the second measurement at T3 was significantly lower in power than

the first, which was likely the result of a loose cable connection. Therefore, this site was disregarded for melt and strain calculations.

5.1.2.3 ApRES data processing

ApRES data is processed in MATLAB using code developed by the BAS. For simple data processing, three main scripts are needed to plot the data as a function of amplitude against depth (*fmcw_plot.m*), a processing configuration file which defines the parameters used (*fmcw_process_config.m*) for the vertical strain and basal melt calculations (*fmcw_melt.m*). The inputs defined in the processing configuration file are:

- The range (in metres) where the bed reflection is searched in, and the method for identifying the bed in that range (default is maximum amplitude). These require prior knowledge of the approximate depth and nature of the base which is found by plotting the trace using *fmcw_plot.m*;
- The thickness of the firn layer. Above this depth layers are subject to deformation and cannot be used to calculate strain;
- The range over which layers are to be matched to calculate vertical strain. This needs to be between the firn layer and the base.

Other parameters which can be changed are;

- The frequency range to be examined. This is set to the entire frequency spectrum by default but can be altered;
- Whether or not basal melting is calculated using the strain value derived from the ApRES or from another method (which then need to be defined manually in the script);
- And other parameters such as the minimum coherence and noise limit for strain calculations.

As calculating basal melting requires the use of parameters that are unique to each site, the processing cannot easily be done automatically and in this case with only 21 sites (each with two measurements) the codes are run manually. The output values are imported into GIS software in order to do further calculations and map/investigate the spatial distribution.

A common issue that can occur during data collection is signal clipping. This occurs when the power of the received signal exceeds the threshold that can be measured by the radar.

Clipping can be avoided by increasing the attenuation of the received signal, but in some environments the maximum attenuation (31 dB) built into the ApRES is not sufficient to prevent the signal from being clipped. Clipping effectively truncates the received sine wave into a square wave. The conversion of the measured frequency to depth requires a fast Fourier transform (FFT), which, when applied to a square wave introduces odd harmonics which appear as false returns at a depth greater than the internal layer. For shallow reflectors, these false returns are superimposed on deeper internal layers and thus cannot be used for calculating strain. As the basal reflector is both the strongest and deepest 'true' reflector it can still be picked out accurately as the odd harmonics created by the FFT of the basal reflector will appear below this depth, and the basal signal will not be obscured by the false returns of the much weaker internal reflectors (C. Stewart, personal communication, February 17, 2016).

5.2 Additional Field Measurements

Density and snow depth measurements are also made in the field to compliment and assist in the interpretation of radar.

5.2.1 Firn cores and snow density

Firn cores provide valuable information about the density profile in the upper layers of an ice shelf. Direct measurements reflect the variety of processes which contribute to snow and firn density (such as temperature, wind, accumulation, and sub-surface densification). Although firn cores represent these processes at a single point and can take a long time to retrieve, they do provide ground validation for models of surface density, density profiles and firn depth.

Density was derived by weighing a section of core with known volume. An exponential model (equation (4.14)) was fitted using the curve fitting toolbox in MATLAB.

5.2.1.1 Firn cores on the RIS

Two firn cores were drilled 30 km apart on the RIS, at points W3 and C (Figure 16). Cores are drilled from the bottom of a snow pit which was 134 cm and 118 cm deep at points W3 and C respectively. A Kovacs ice drill was used to drill to greater depths, with the length of the core drilled at W3 exceeding 14 m, and that at C reaching a depth of 16 m.

Density measurements are taken in the snow pit with a TOIKKA snow fork (http://www.toikkaoy.com/) at 3 cm intervals and by weighing snow samples. Density from

the firn core was derived by weighing sections of core with known volume. At site C, the firn core was cut into 2-3 cm thick slices and a section with a diameter of 3.56 cm was extracted from the middle using a hollow cylinder. This method introduced large errors as the extracted section would often fracture along the edges and the resulting slice was not perfectly cylindrical. To avoid this problem, density of the core taken at site W3 was measured from slices with the full diameter of the core that was removed from the barrel and a thickness of 4.9 cm.

Uncertainty in the density arises from measurement errors in the mass and volume. The mass was derived by using a digital scale which had a precision of 0.1 g. The digital scales were compared to high precision spring scales and the masses were the same to within 0.4 g. Thus, a 0.4 g uncertainty is applied to all mass measurements although this is insignificant compared to thickness uncertainties.

Measurements of cylinder diameter and thickness are the two contributors to ice volume uncertainty. The error in thickness is 0.1cm for slices and is the same for all slices; however the average relative uncertainty at C (19.25%) is significantly different higher than at W3 (5.45%). Sampling at a high resolution allows for more data to be collected, but this increases the relative error in the measurements.

Despite large errors in individual measurements, the firn corrections derived from the two cores are consistent (section 5.2.1.3). Uncertainties are not incorporated when fitting the density curve as the natural variability usually exceeds the measurement uncertainty. The fitted curve approximates average density with depth and thus any natural variability is smoothed out in the process.

5.2.1.2 Firn core on the Southern McMurdo Ice Shelf

A 9 m firn core was drilled on the SMIS. Density is measured by cutting the core into 5-10 cm slices and weighing them using a spring scale. The top of the core was 49 cm below the snow surface. Due to inconsistencies between sites in the approach of measuring density, it is difficult to say which site exhibits the most natural variation. As expected, due to its closer proximity to the coastline, the depth to the firn-ice transition layer on the SMIS is less than on the RIS due to increased densification (Table 3).

5.2.1.3 Firn correction from firn cores

The density models fitted to the three firn cores (Figure 17) are summarised in Table 3. Assuming that this relationship is representative of density to the firn-ice transition ($\rho \approx 830$ kgm^{-3}), the depth to this layer is estimated and is also included in Table 3.

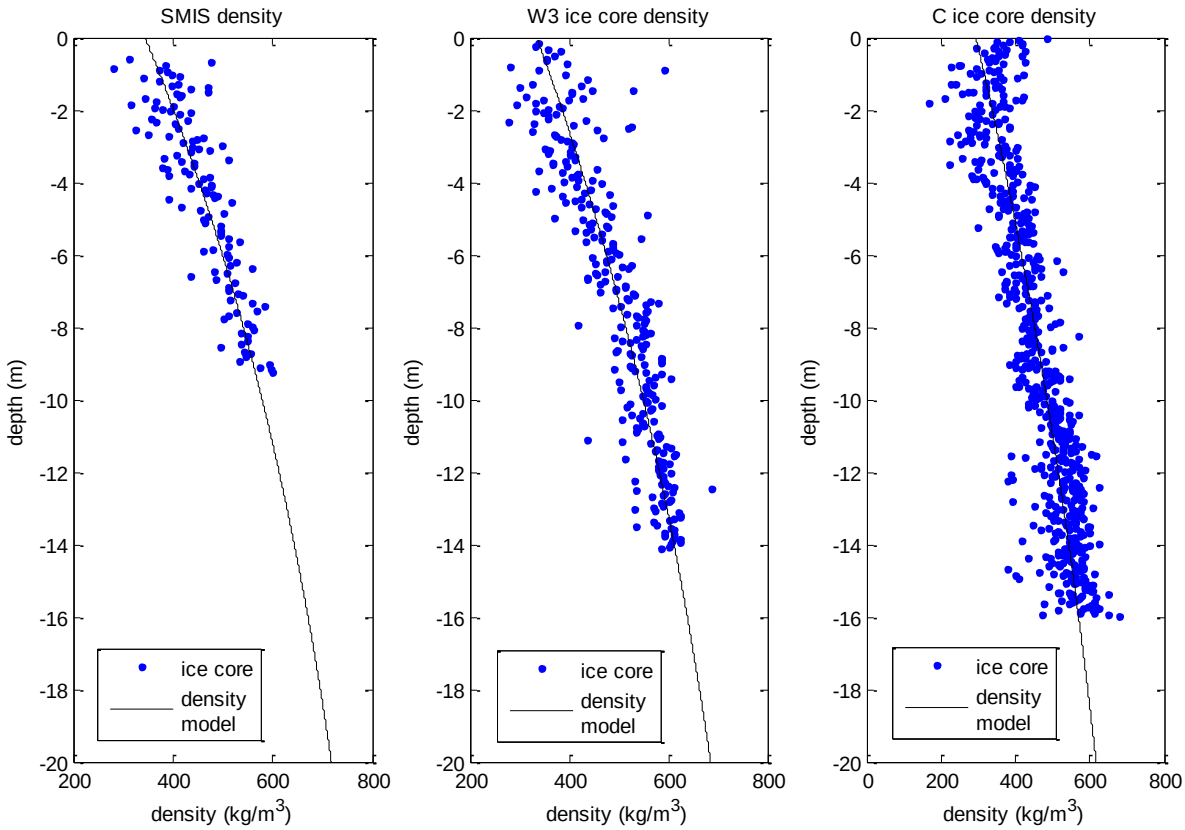

Figure 17. *Density measured from firn cores on the SMIS and the RIS (W3 and C). The black line is the fitted density profile (Table 3).*

The term in the exponential is the densification factor C which is used to calculate the air layer thickness, which is then used to derive the radar firn correction (section 4.2.2) (Table 3).

Table 3. *The firn correction calculated for all three firn core sites and compared to the modelled correction calculated using modelled firn air layer (Ligtenberg et al., 2011).*

Site	**SMIS**	**RIS - W3**	**RIS - C**
Firn density profile	$917\text{-}573e^{(-0.0529z)}$	$917\text{-}582e^{(-0.0461z)}$	$917\text{-}623e^{(-0.0366z)}$
Surface density ρ_s (kgm^{-3})	344	335	294
Depth to firn layer (m)	36	41	61
Densification factor (C)	0.0529	0.0461	0.0366
Firn air layer from firn core (m)	11.8	13.7	14.7
Radar firn correction from firn core (m)	5.2	6.0	6.5
Modelled firn air layer (m)	15.7	16	16
Modelled radar firn correction (m)	6.9	7	7

In the region of the W3 and C firn cores, the firn corrections calculated from the cores are comparable to that derived from the modelled air thickness (Ligtenberg et al., 2011). These results suggest that the modelled firn correction is a good approximation for the entire RIS field area. On the SMIS there is a difference of 1.7 m in the radar firn corrections, however, the modelled firn air layer has a resolution of 27 km (with some of the cell lying over White Island which has a different accumulation regime) so is unable to capture the spatial variability of the firn layer within the field area. As a result the radar firn correction derived from the firn core is applied to the GPR data as it better represents in-situ conditions. Due to the higher accumulation near the grounding line (section 5.2.2) it is likely that the firn layer is deeper in this area, however, further than 600 m seaward from the grounding line this firn correction is a good approximation as the internal stratigraphy is flat (section 6.1.1).

5.2.2 Snow accumulation on the SMIS

In order to examine the spatial variability of snow accumulation the thickness of the top snow layer on the SMIS was measured along the central grid line. The depth to the first icy layer, which is assumed to represent the surface of the previous summer melt season, was

measured using stakes and snowpits. The measured accumulation, using this technique, represents approximately nine months of the year over winter. As the absolute age of the snow layer cannot be deduced, it is impossible to know if these interpretations are correct, but the measured accumulation (Figure 18) is reasonably consistent with that modelled by (Monaghan et al., 2005). Regardless of the age of this layer, important information about the snow distribution is revealed. The area of highest accumulation is where there is a change in surface slope across the grounding line. This increased accumulation is a result of wind redistribution rather than direct precipitation.

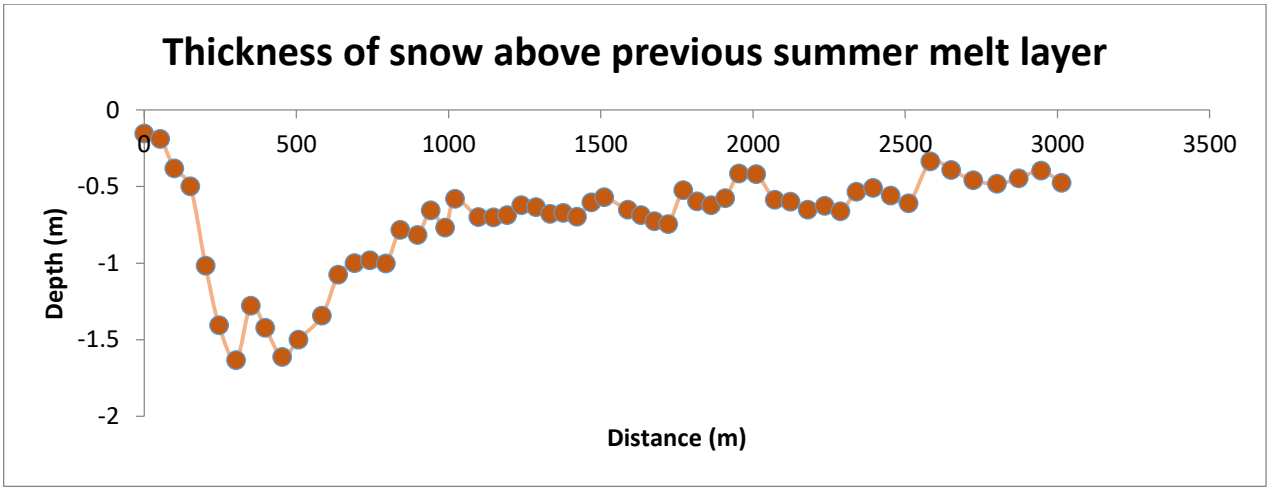

Figure 18. *The thickness of snow along the central line of the SMIS from north (grounding line) to south (freely floating).*

5.2.3 Other field observations

5.2.3.1 Southern McMurdo Ice Shelf

The surface of the field area on the SMIS was generally very smooth and characterized by small undulating wind dunes which did not exceed 30 cm in height or 3 m in length. These features have a north-south alignment which is consistent with the southerly prevailing wind direction (Monaghan et al., 2005), however, the predominant wind direction observed during the field campaign was from the north-west and coincided with a period of fine weather.

Numerous ice lenses were present in the snowpack beneath the upper layer. These are formed during melt-refreeze events and indicate that liquid water is sometimes present. This has implications for firn densification as the melt-refreeze process increases the firn density and thus the rate of densification also increases. These lenses were mostly small (<1 cm thick) and were less than 1 m in diameter.

5.2.3.2 Ross Ice Shelf

The surface of the RIS was also characterised by windblown features but, the nature of these changed regularly across all the sites in terms of feature size, crystal size and shape. Between the two firn cores there was a change in the morphology of the snow with depth hoar present in the core at C which was not encountered at W3 in any significant volume. Due to the relatively close proximity of these firn cores, these variations are most likely due to local redistribution of snow by the wind rather than from different regional weather patterns (M. Arnold, personal communication, September 5, 2016).

6 RESULTS AND INTERPRETATION OF RADAR

This chapter presents the results and interpretation of the radar field studies and the ice shelf properties described in section 4.2. It is structured so that the results of the GPR survey on the Southern McMurdo Ice Shelf (SMIS) are presented first, followed by the ApRES survey on the Ross Ice Shelf (RIS).

6.1 GROUND PENETRATING RADAR ON THE SMIS

During data processing, features in the radargrams (e.g. internal layers, ice shelf base) are 'picked' semi-manually in the Reflexw software package. As these features are not represented by a single peak in amplitude but as a waveform, the location of each feature is defined as the maximum amplitude of this waveform. The range is the distance between the start and end of the waveform and represents the apparent thickness of a feature (Figure 19).

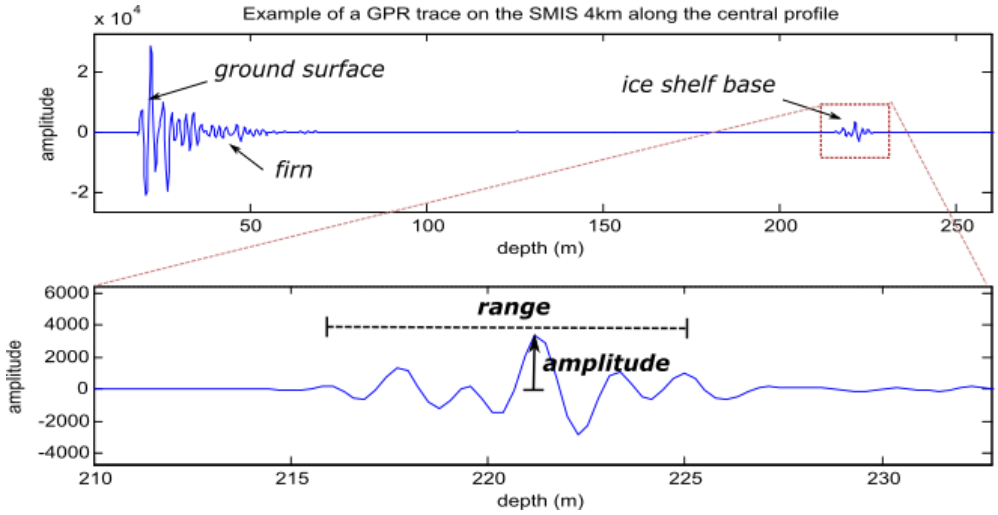

Figure 19. *An example GPR trace from the SMIS. The top panel shows the entire trace and the bottom is just focused on the ice shelf base. In this case, range is defined as the distance between the first and last peaks of a feature and amplitude is the maximum amplitude within this range.*

6.1.1 Internal stratigraphy from GPR

Internal layers are visible in all radar profiles (Appendix A.1.) and the common assumption that they are isochrones is made. These layers are mostly parallel to one another as would be expected for annual layering, but, there was nothing found in the firn core, such as a dust or ash layer, which could be used as a reference for dating. Therefore, we cannot say with any certainty which layers represent an annual or seasonal cycle, and changes in accumulation patterns cannot be assessed.

Although the data appears to be noisy, on closer inspection some of this ‘noise’ indicate small areas of higher amplitude reflections that are aligned with the internal layers. These anomalies are most likely caused by ice lenses that form during summer melt seasons. Ice lenses were observed near the surface in the field, and as there is no evidence to suggest that the climatic conditions in this area have changed significantly in the past few decades, it is assumed that these anomalous reflectors at depth are consistent with features seen at the surface. The presence of ice lenses is an important feature as they reveal that this part of the ice shelf is not in the dry snow zone and is subjected to summer surface melting, which can have important implications for the densification of firn. These ice lenses are not further discussed but it is important to note that processing steps to reduce noise need to be applied carefully as to not remove important information about the ice.

In the north-south orientated radar profiles there is a clear dip in the internal layers near the grounding line forming a synclinal feature (Figure 20). The deepest layers are truncated at the base. There are two possible explanations for the dipping of internal layers; an accumulation anomaly or downwarping due to basal melting. Accumulation is highest in this area due to a change in surface slope across the grounding zone as shown by measurements of snow depth, but this is only of the order of 1-2 m (Figure 18). This is not sufficient to explain why these layers are up to 10’s of metres thicker than on the freely floating ice shelf, and why the amplitude of the dip of these layers increases with depth.

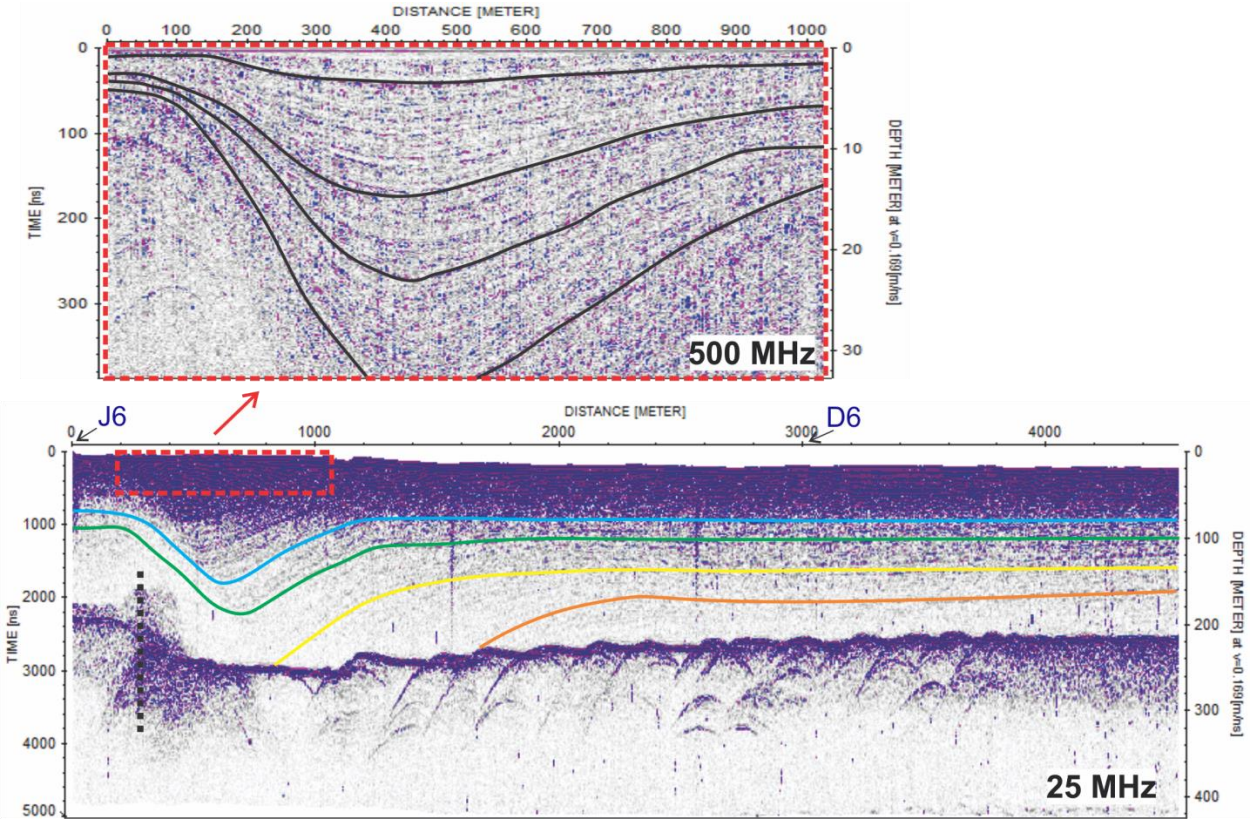

Figure 20. *Internal layers visible in the central radar profile in both firn (500 MHz) and ice (25 MHz). There is a clear dip in layers seaward (right) of the grounding line (dotted black line), which increases with depth (insert). At depth the layers (represented by the yellow and orange lines) are truncated at the ice shelf base.*

The other possible explanation is due to 'downwarping' of internal layers in response to basal melting near the grounding line (Catania et al., 2006). As the base is melted away in this area, the ice shelf responds hydrostatically by lowering its surface, dragging these layers downwards. This phenomenon has previously been observed at the grounding line of Siple Dome and Roosevelt Island (Catania et al., 2010).

On the freely floating part of the ice shelf the layers are flat and parallel throughout the entire ice column. While this is expected for layers close to the surface which have formed in-situ by snow accumulation and densification, this reveals that the ice at depth has not been previously been deformed as would be the case if it had been subject to a major changing stress field such as the RIS shear zone. Layers in the 1000 MHz data appear much rougher than the equivalent layers in the 500 MHz data. This is consistent with field observations of snow that had been redistributed by the wind, however, the data are not of sufficient quality to clearly distinguish buried surface features, the size and orientation of which could yield possible information about changing wind strength and directions.

6.1.2 Basal topography

As there is a large contrast in the dielectric permittivity of ice and seawater, the reflection at the ice shelf base is expected to be strong and no reflections are expected to originate from below this interface. Nevertheless, the receiver does not only record reflections from directly beneath the radar (nadir), but also from the sides. GPR are designed in such a way that most power is transmitted downwards and the strongest signal is usually from a nadir reflector, however, the pattern of the radiated power is not published for the PulseEKKO PRO GPR system. As the shortest distance for the radar wave is the nadir reflection, the first strong reflection is interpreted as the ice shelf base directly below the radar. Any reflections beneath that are from off-nadir targets such as crevasses. Instead it is the pattern of the reflected wave off that feature. As the radar approaches the target, some of the energy is reflected back to the receiver. As the radar gets closer, the path-length decreases and the received signal appears closer to the surface. Eventually the radar is at its closest point to the target, and as it moves beyond it the reflection dips downwards forming the other half of the hyperbola. For point targets, the reflected signal is a simple hyperbola, but for two and three dimensional features such as lines and crevasses the reflection pattern is increasingly more difficult to interpret. The shape of a hyperbola can reveal information about the shape of that feature and its orientation relative to the radar profile.

The basal reflectors in the radar profiles display many distinct hyperbolic features. The peaks of some of these hyperbolas do not intersect the ice shelf base as they are caused by features to the side that are not crossed by the radar profile. In contrast, profiles which are parallel to the grounding line have either; no hyperbolic features, half hyperbolas, or very wide hyperbolas.

The basal topography of the profiles perpendicular to the grounding line can be separated into five distinct zones based on their morphology. These zones are described in further depth below and an interpretation of the basal conditions is made.

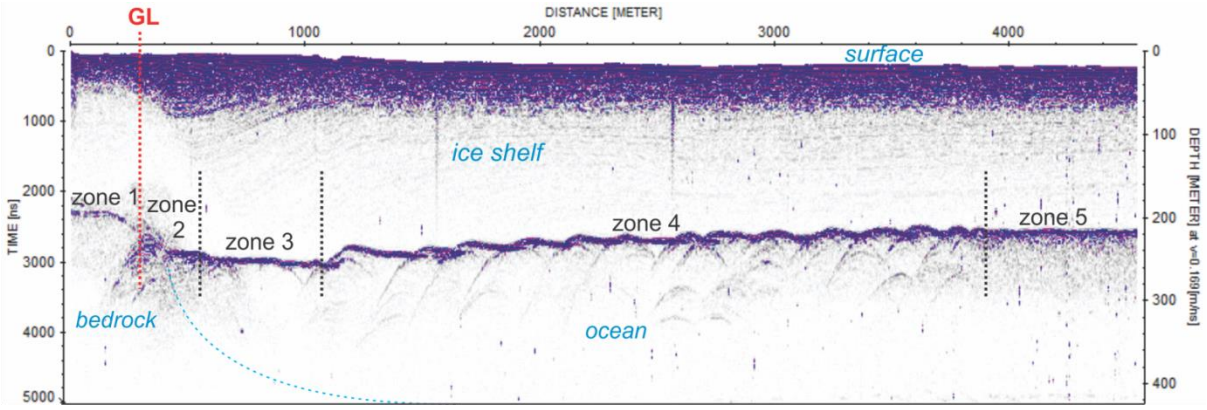

Figure 21. *The five basal zones in the radar profile along the central line. The grounding line position is interpreted as the boundary between zones 1 and 2. The surface has been topographically corrected. The depth (right axis) is not firn corrected and assumes a radar wave velocity of 0.169 m/ns. Note that the blue dashed line, which indicates the bedrock-ocean boundary, is for schematic purposes only as this interface is not visible in the radargrams.*

Viewed from a bird's eye perspective (Figure 22), the grounding line from the GPR closely matches that from satellite imagery. However, the distribution of zones 2-5 do not reflect the geometry of the grounding line indicating that the processes that create these zones are mostly independent of the grounding line configuration.

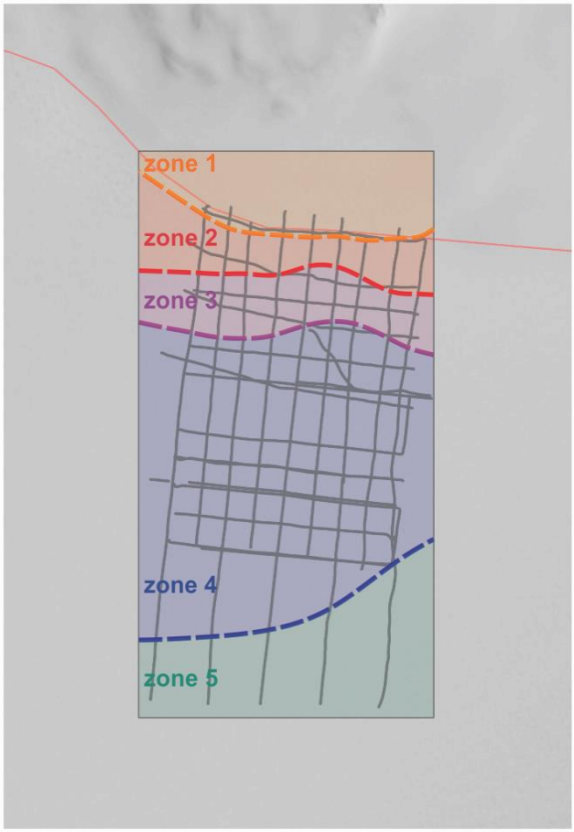

Figure 22. *The five basal zones viewed from a bird's eye perspective. The thin red line is the grounding line from the InSAR flexure profile. The thick orange line represents the grounding line from the GPR profiles.*

The ice-bedrock interface is distinguished from the ice-water interface by a simple amplitude analysis. Within each zone, 20 traces are selected at regular intervals. For each trace, the maximum amplitude of the basal reflector, and the range (Figure 19) over which the reflector appears is manually determined. The range is converted to thickness using radar velocity in ice (Figure 23).

There are two factors that normally need to be taken into account in order to use this method to classify unknown reflections. Firstly, the range (thickness) of the reflector is defined by manually picking out the start and finish of the basal signal. This can be heavily influenced by the contrast between the signal and the background noise. Secondly, the amplitude should be gain corrected to account for power attenuation with depth. In this case (Figure 23), the amplitude of the ice-water interface is significantly greater than that of the ice-bedrock boundary despite the greater depth (zones 3-5, see below). Applying a gain would only enhance these stronger reflectors, therefore, amplitude was not corrected for depth as it is not required to distinguish between different reflection types.

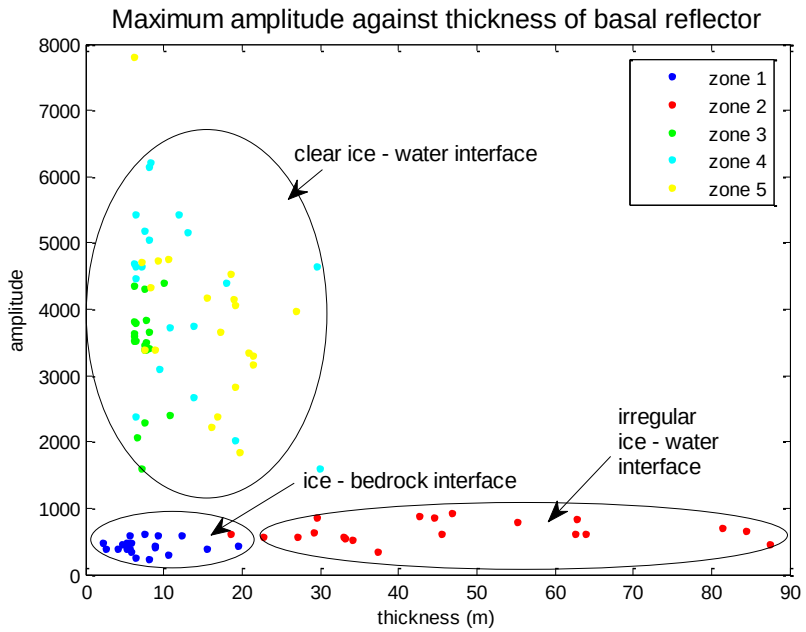

Figure 23. *A comparison between the maximum amplitude (y axis) and the apparent thickness (x axis) of the basal reflector. There are three distinct classes of points which combined with the interpretation of the radar represents the different interface properties; smooth ice–water interface (large amplitude, thin reflection), rough ice–water interface (smaller amplitude, thicker and more variable), and smooth ice–bedrock interface (small amplitude but thin reflection). Note that as amplitude is not corrected for depth, the values plotted are not a true representation of the amplitude value.*

Zone 1.

In this region the ice shelf base appears smooth and is dipping downstream. Amplitude analysis shows that this is a moderate strength reflector. In conjunction with these

observations, this region is upstream of the grounding line inferred from interferometry. Therefore, the ice is grounded in this area and the sharp nature of the reflection shows that there is most likely bedrock rather than sediment underlying the ice.

Zone 2.

This zone is characterised by a large number of hyperbolas that create a diffuse reflection from which it is difficult to identify the base. The maximum amplitude of these hyperbolas is comparable to the ice-bedrock interface in zone 1, which is an order of magnitude less than in zones 3-5, but the apparent thickness of the reflector is significantly greater. This is interpreted to be where the ice has just become afloat and the hyperbolas are basal crevasses that are caused by a changing stress field. It is possible that these crevasses are filled with marine ice or diluted seawater.

The grounding line is interpreted to be at the boundary between zones 1 and 2. As this may not be a static position (section 2.1), however, here the term is used to define the grounding line at the time the radar measurement was made.

Zone 3.

The ice shelf base is flat and featureless in this region. This is where the ice is the thickest in the radar profiles. The amplitude of the basal reflection in this region is significantly greater than in zone 1 which confirms this to be an area where the ice is in contact with the seawater. The apparent thickness of the reflector is the most uniform in this zone.

Zone 4.

The base in zone 4 is characterised by 'half hyperbola' reflections and extends to the outer limit of the flexure zone. These features are spaced at semi-regular intervals of 200 ± 50 m, apart from the first two at the grounding line edge of this zone which are about 360 m apart. Most of these features have a height of approximately 10 m in the radargram.

This profile is similar to features seen near the grounding line of both the Darwin-Hatherton glacier (Riger-Kusk, 2011) and Ice Stream C (Peters et al., 2005). Peters et al. (2005) interpreted these reflections to represent jumbled blocks of ice as a result of cracks and crevasses induced by tidal flexure. Internal ice layers near the base on the SMIS do not show features of deformation which would support this hypothesis. Other explanations include: sudden vertical changes in basal topography creating a stepped base, crevasses

with an axis at an angle (Catania et al., 2010), or rough walled bottom crevasses (Clarke & Bentley (1994) as cited in Riger-Kusk (2011)).

The 2-dimensional radargram does not represent the true geometry of a 3-dimensional feature. Therefore, the stepped appearance of this zone is not necessarily caused by a stepped ice shelf base. In order to determine whether or not this may be the case, a simple model of a stepped ice shelf base and the equivalent reflection profile were simulated in Reflexw (Figure 24). The model consisted of five steps with varying geometries (A-E). The slope of the reflection closely matches that of the model, with the only issues arising where there is a sharp vertical change (a step up) in the base. The resulting modelled reflection profile closely matches that observed in zone 4, which has characteristics of all steps A to E across the different profiles (Appendix A.1). The modelling function in Reflexw did not allow for the simulation of a radargram for crevasses tilted at an angle. Based on the results from the step model (Figure 24), it would be expected that thinner crevasses would produce resulting hyperbolas with a much steeper angle than what is observed. It is impossible to know with absolute certainty the base geometry without direct observations, but according to the model results the ice shelf base in zone 4 is most likely characterised by a series of steps with a vertical height identical to what is observed in the radar.

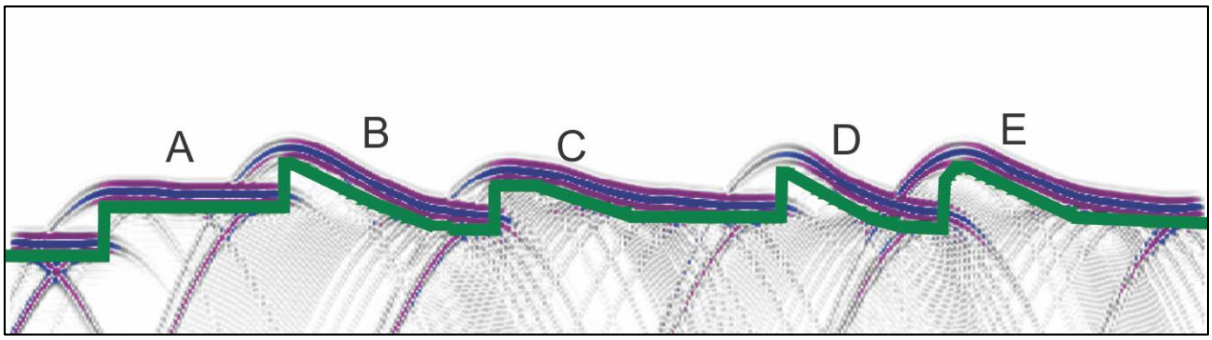

Figure 24. *The basal step model (green) and the simulated GPR profile (blue and purple). The letters A-E represent different step geometries. The step height and widths are modelled to match observations (horizontal and vertical axis are not shown).*

Zone 5.

The stepped features in zone 4 smooth out into zone 5. Zone 5 is downstream of the flexure zone where the ice is in hydrostatic equilibrium. The base is flat and featureless but the interface is not as specular as in zones 3 and 4. It is possible that marine ice has started to accumulate or that the ice shelf base is slightly rougher. Basal freezing is an important contributor to the mass balance of the SMIS, especially in the ablation area to the north of

Minna Bluff where marine ice is revealed at the surface (Clifford, 2005), so towards this region it is expected that the radar reflection would become weaker.

6.1.3 Basal crevasses and steps

The alignment of basal crevasses (zone 2) and steps (zone 4) has been investigated using adjacent and crossing profiles. The common GPR processing step of migration was not applied to the data as it failed to sufficiently collapse the hyperbolas. It is likely that migration does not work in this case as it is best suited to the reduction of hyperbolas from point features, whereas the reflection from a three dimensional object, such as a crevasse, is much more complicated.

These basal features are much wider in the east-west profiles which reveal that they are aligned more parallel than perpendicular to the grounding line (Appendix A.1). In the N-S profiles the full hyperbolas are fairly symmetrical which indicates the crevasse axis is nearly vertical. The general pattern is of a series of basal crevasses (in zone 2) and steps (zone 4) which are aligned nearly parallel to the grounding line. Assuming that the peak of the hyperbola corresponds to the tip of the crevasse, they do not penetrate further than 20 m into the ice shelf with most being less than 10 m high.

6.1.4 Ice thickness from GPR

The strong reflections at depth are from the ice shelf base. In many cases there are a number of strong reflections layered vertically but the first one is picked for calculating ice thickness as this is the nadir return. Anything else is off nadir, with exceptions possible near the grounding line where if nearby crevasses are large enough, the reflected radiation from them can arrive first. As discussed in section (6.1.2), this area is very difficult to interpret due to the nature of the bed. The corresponding perpendicular GPR profile (Figure 25) does not display a clear signal for the ice shelf base and therefore ice thickness is not picked for this line.

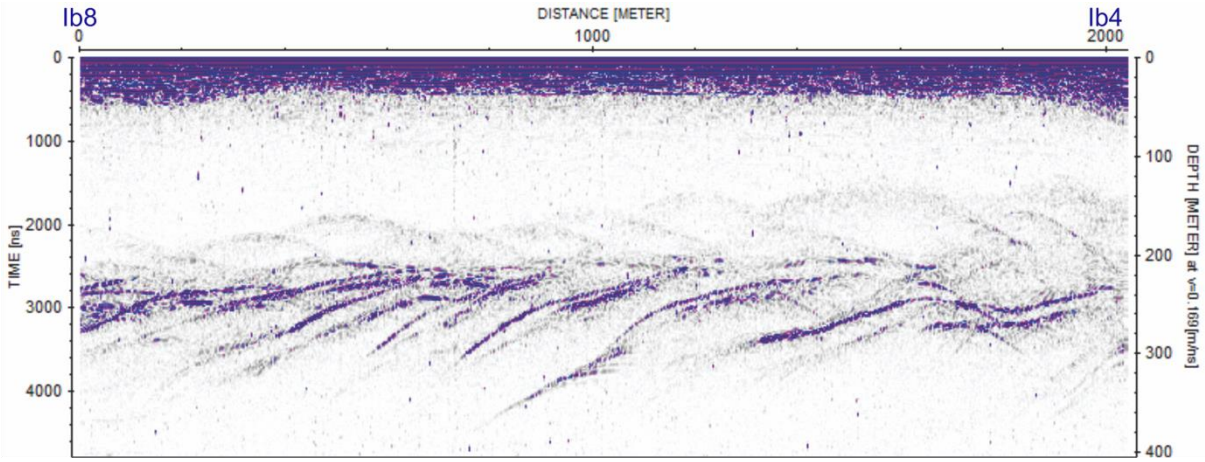

Figure 25. *The GPR profile for line Ib which lies in a zone of significant basal crevassing. These crevasses cause a complicated reflection from the base of the ice shelf. For this reason, the bed was not picked out as it is not possible to validate its location as the reflection at the corresponding crossing points are equally complicated.*

Ice thickness (Z) is determined by converting the TWT output from the picking process to ice thickness using the equation;

$$Z = \frac{TWT}{2} * v - \Delta z$$

Where v is the radar velocity in pure ice, and Δz is the firn correction derived from the firn core (section 4.2.2). This corresponded to a firn correction of 5.2 m. The final ice thickness has a corresponding radar wave velocity of 0.173 m/ns which is identical to that used by McGrath et al. (2012).

The measured ice thickness is resampled to smooth the thickness along profiles which removes any sudden 'jumps' or gaps in the data which result from the 'picking' step in Reflexw. A horizontal resolution of 10 m was chosen as this did not remove the characteristics unique to each basal zone while adequately smoothing the profile. Resampling was achieved by calculating the average thickness within each 10 m interval.

6.1.4.1 Cross-over analysis of ice thickness

To evaluate the accuracy of the ice thickness, a cross-over analysis of ice thickness is conducted. The resampled thickness of two profiles are interpolated at their intersection point and ice thicknesses are compared. The median difference in ice thickness at crossing points is 1 m and the greatest discrepancies are found near the grounding line where the radar profiles are the hardest to interpret as discussed in section 6.1.2.

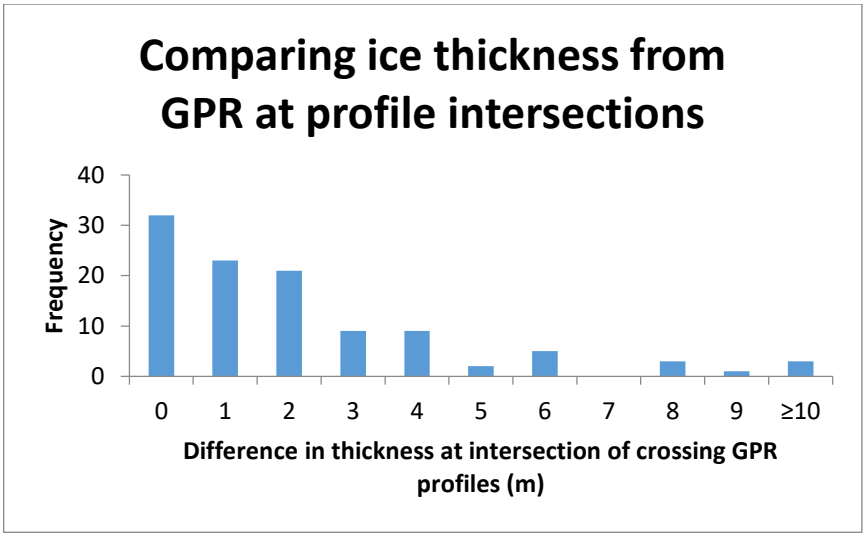

Figure 26. *Difference (in metres) of ice thickness at the point where two GPR profiles cross.*

The distribution of this error is largely skewed towards well matched thicknesses (Figure 26). No significant relationship was found between the orientation of a GPR profile and its thickness relative to the crossing one. Further information can be found in appendix A.2.

6.1.4.2 Ice thickness map

The ice thickness between measurement profiles is interpolated using ArcMAP. This is achieved using inverse distance weighting (IDW) which linearly weights points depending on their proximity. The value for a cell is determined by averaging the weighted points found within a search neighbourhood. Points which are closer to the cell are weighted higher as it is assumed that they have more influence on the cell than points further away.

One limitation of IDW is because it calculates averages it cannot reproduce ridges or valleys, unless these features are sufficiently sampled. In this case, as the cross section of basal crevasses cannot be accurately determined the ice thickness through this region is picked as a line rather than a series of hyperbolae. The resulting interpolated ice thickness produced by the IDW algorithm will be unable to accurately reproduce the presence of crevasses. Similarly, the steps that are present in zone 4 will also not be reproduced as the neighbourhood radius needs to be large enough to successfully interpret between GPR lines and the averaging of the points within this neighbourhood smooths these features out.

An IDW interpolation with a horizontal resolution of 250 m is applied over a region which encompasses all the GPR data. This is followed by a bilinear resampling interpolation to smooth out the appearance of the map (Figure 27.a), however, the western area of the study area has a blocky appearance. This is not caused by physical features of the ice shelf, but

is rather an artefact of the interpolation due to the low density of GPR data available in this area. Overall, ice thickness has the expected pattern of thinning at distance from the grounding line.

In order to create a higher resolution map of ice thickness, IDW interpolation is applied to the central region of GPR data with a resolution of 100 m, and then resampled to 10 m to match the resolution of along-profile GPR points (Figure 27.b). This two-step process was required as applying an IDW interpolation at a higher resolution created stripes between the GPR traces due to a lack of data in this dimension.

The pattern of ice thickness change is very clear in Figure 27.b. The ice is thickest approximately 750 m seaward of the grounding line. The ice thins from approximately 255 m at its thickest part to 195 m where it is thinnest (at the north and south extremes of the map). The gradient of ice thickness from where it is thickest across the grounding line is much higher than in the opposite direction (i.e. thinning 60 m over 750 m horizontal distance compared to 60 m over 3500 m). This rate of thinning cannot be used to extrapolate further upstream as ice thickness is likely to be affected by the bedrock topography of White Island. The subtle 'checkerboard' pattern which is visible in the southern half of the map is a result of the stepped base in zone 4. This is partly caused by large gaps between traces where these features may terminate which is not captured within the data, but there are also a number of cases where step geometry can create this pattern. In particular are examples where ice thickness decreases in steps, but then increases slightly before the next step (similar geometry to steps B, C and D in Figure 24).

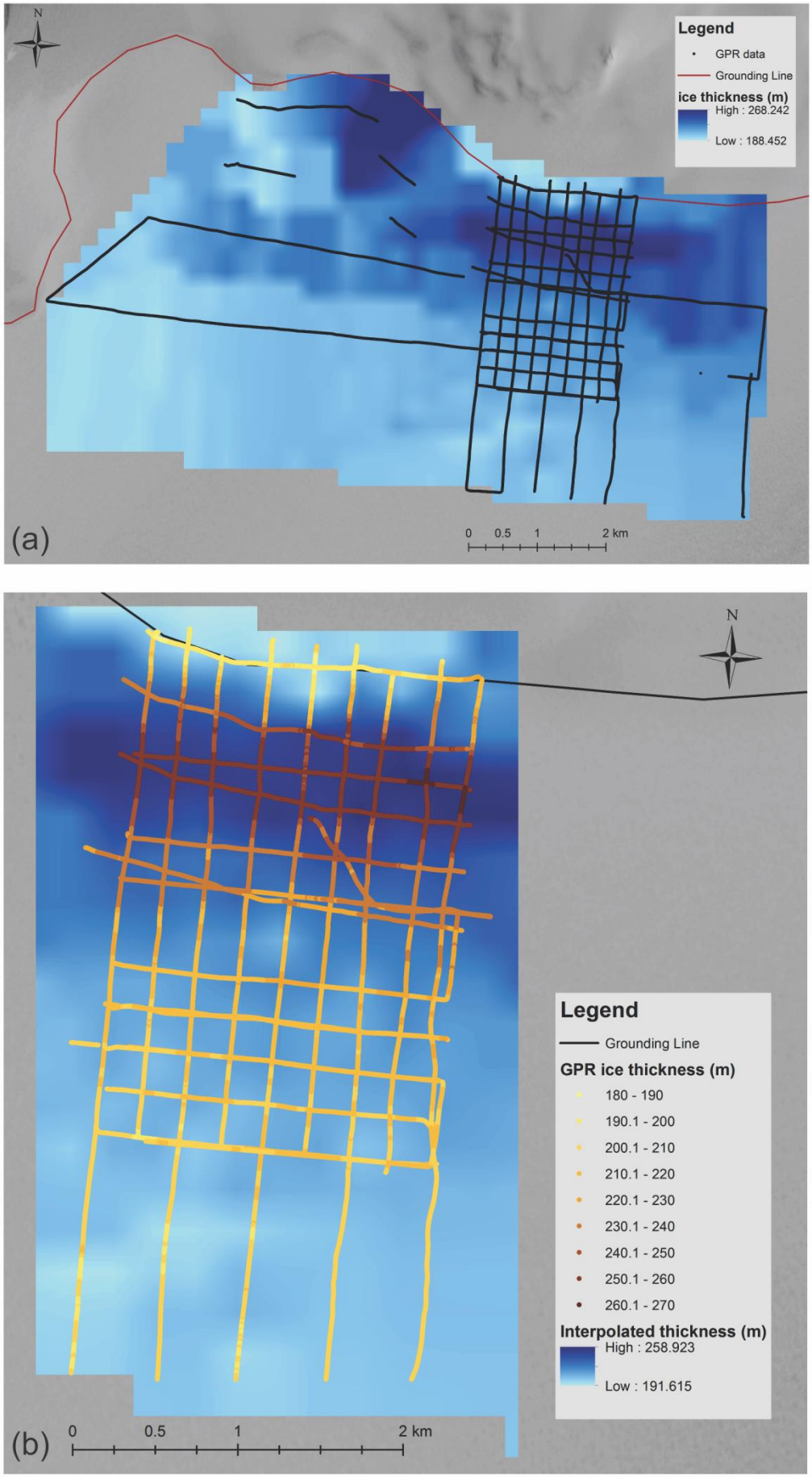

Figure 27. *GPR based ice thickness of the SMIS measurement area with (a) showing the interpolated map at 250m resolution with a bilinear resampling interpolation to smooth the appearance of the data, and (b) the colour coded ice thickness profiles at 10 m intervals for the central measurement area plotted on the interpolated ice thickness map.*

6.1.4.3 Uncertainty in ice thickness

Uncertainties in ice thickness arise from data collection through to interpolation. A discussion of these different factors and how their associated uncertainties were addressed are given below.

Positional errors during data collection are associated with the GPS. The horizontal resolution of the unprocessed Trimble GEO-XH GPS is 5 m which is considered satisfactory in this case as the position on the surface represents the peak of a cone of radiated radar energy. For a single trace, the signal received from the base of the ice shelf does not represent the basal conditions immediately below the GPR system, but rather a region surrounding it defined by the antenna footprint. Without knowing the pattern of radiated power it is impossible to accurately determine how far the radar wave spreads by the time it reaches the base, however, it can be estimated from hyperbola width. The widest part of the hyperbola represents the range at which the radar is detecting that feature and is approximately 200 m. This is significantly greater than the uncertainty in the GPS position, therefore, further processing of the GPS data was not required. Additionally, any further inaccuracies are smoothed out during the resampling of the data to 10 m resolution so should have a negligible contribution to the thickness map.

Identification of the basal reflection is complicated in some areas. For example, in zone 2 a very diffuse basal reflector does not allow a clear identification of the base. As discussed in section 6.1.2, this part of the ice shelf is underlain by numerous basal crevasses which creates a complicated reflection pattern. As discussed in section 6.1.4.1 this is where the greatest discrepancies between ice thicknesses of crossing GPR profiles are.

When picking, the assumption that the first strong reflection represents the base is made. If the ice shelf base was perfectly flat this assumption is valid, however, in areas with more complicated topography a large feature (such as a crevasse or steep slope), that is adjacent but not intersecting the GPR profile, may be closer to the radar than the nadir reflector (e.g. Line D: D8-D4 in Appendix A.1). In this case, an off-nadir reflection may arrive first. The only zones were this may pose a problem are 2, and 4. As the nature of the reflection in zone 4 is consistent across all profiles and given that it is extremely unlikely that all of these profiles would closely pass but not intersect a large number of identical features it is concluded that the ‘stepped’ characteristic of this zone is from a nadir reflector. Similarly for zone 2, most of the hyperbolae are from basal crevasses crossed by the radar. But the

signal is too complicated in this area, possibly due to a relatively high crevasse density, which makes it impossible to accurately determine what reflections are nadir and off-nadir.

The method of identifying and picking out the basal layer is highly dependent on user interpretation. Here, the base was picked as the maximum amplitude within the signal that was interpreted to be from the base. However, the time zero correction was applied to shift the reflected signal so that the first arrival of the surface reflection is at t=0. This does not correspond to the peak of the ground reflection, but oversaturation of the signal near the surface means that this cannot be corrected for unless better information about the emitted waveform is known.

It is likely that the application of a uniform firn correction of 5.2 m over the whole field area is incomplete because of the variable snow accumulation across the grounding zone. In order to minimise the error associated with the firn correction, a correction based on in-situ density measurements from a firn core was used rather than deriving it from a modelled air-firn layer. The horizontal resolution of the modelled air firn layer is 27 km, and the grid cell with the field area covers a significant portion of White Island (Ligtenberg et al., 2011). The firn core was taken from a spot seaward of the grounding line which lies in the region where the internal layers are parallel to the surface. Therefore, it is likely that the firn correction calculated from the core is more representative of the density conditions in this area. The greatest uncertainty in the firn correction is near the grounding line due to increased accumulation, but this is the area where the uncertainty in ice thickness is the greatest. The expected variability in the firn correction is of the order of 2-3 m which is a small contribution to the total uncertainty which is dominated by difficulties in defining the base in the radar profiles.

The process of interpolation may also add error to the ice thickness. To test the robustness of the IDW tool here, the modelled ice thickness is directly compared to the measured ice thickness where a GPR point lies in a grid cell. The interpolated ice thickness closely matches that of the GPR profiles (Figure 28). A comparison of the modelled thickness at each GPR point revealed that there was less than 2 m discrepancy for 49 % of the points. The largest errors were found in the area of basal crevassing, where profiles cross over, and in small localised places which may be related to picking uncertainties of the ice shelf base in Reflexw.

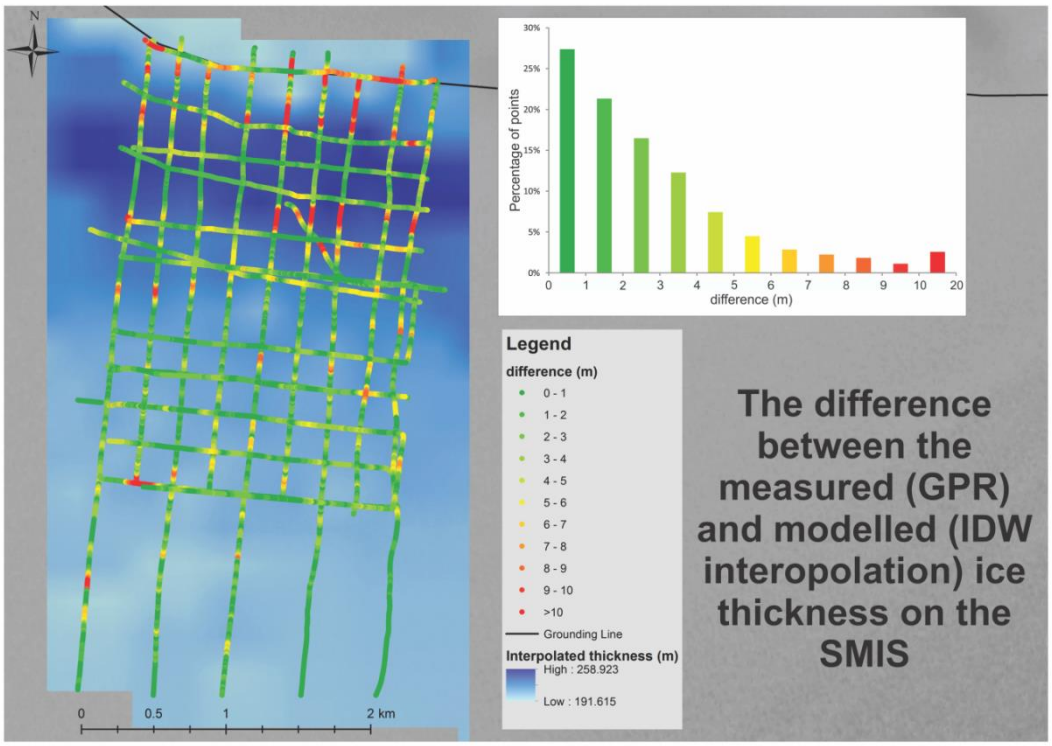

Figure 28. *A comparison between the measured ice thickness from GPR profiles and the surrounding area calculated with an inverse distance weighting interpolation.*

The total error in the ice thickness measurements is largely dependent on the zone. Given the multiple sources of error, it is unlikely that the combined uncertainty exceeds 10 m (<5 % of total thickness) with most areas being significantly less. However, without a better understanding of the transmitted radar wave, and the spatial variability of the firn layer this error cannot be better constrained. There are no previously published direct measurements of ice thickness in this region which these results can be compared with.

6.2 ApRES Compared with GPR on the SMIS

To validate the accuracy of ApRES for measuring ice thickness and identifying internal features, a number of ApRES point measurements were made along the same central line as the 25 MHz GPR on the SMIS. Ice thickness from the ApRES is compared to the results from the GPR (Figure 29). Whilst the appearance of an ApRES profile is significantly different to that of a GPR, they both show an increase in amplitude due to the strong dielectric contrast between ice and seawater. The ice-water interface is normally easier to identify in ApRES than GPR, but complications arise when there is marine ice present (discussed in section 6.3).

To ensure consistency the signal was converted to depth using radar velocity in ice and the same firn correction (5.2 m) is applied to both systems.

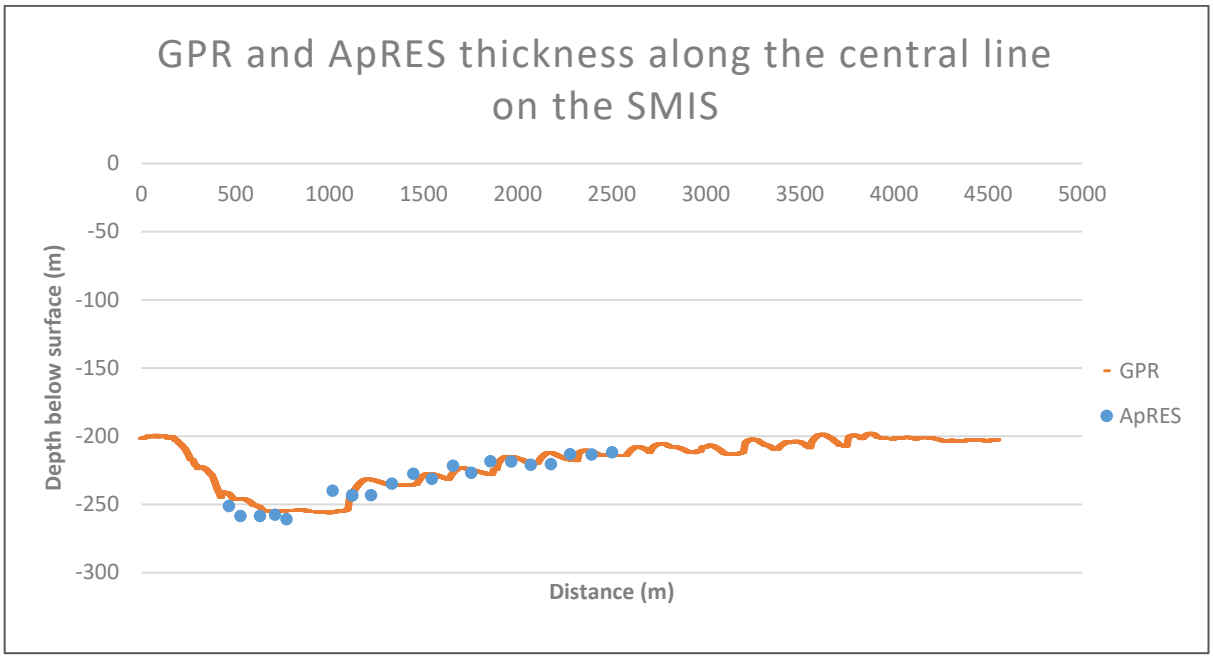

Figure 29. *A comparison between ice thicknesses measured with the GPR and ApRES radars along the central grid line. The same depth conversion and firn correction have been applied to both systems.*

From Figure 29 it can clearly be seen that the ApRES measured thicknesses are consistent with the GPR. Any discrepancy is most likely to due to differences in the methods of picking the base, a process which relies heavily on the interpretation of the profiles. The nature of the bed reflection in the ApRES displays significant variation across the 5 zones (Figure 30), with traces in zone 2 being too complicated to identify the bed due to the presence of basal crevasses creating multiple and/or weak basal reflections.

For a number of the sites (e.g. Figure 30.a) there appear to be multiple bed reflections in the ApRES data. This is caused by crevasses, steps or bedrock features. Interpreting the nature of the bed from ApRES point data alone would be difficult without the GPR profiles as these features all produce similar basal reflections in point measurements. Similarly to the GPR, the first of these reflections is assumed to be the nadir reflection and is thus identified as the bed.

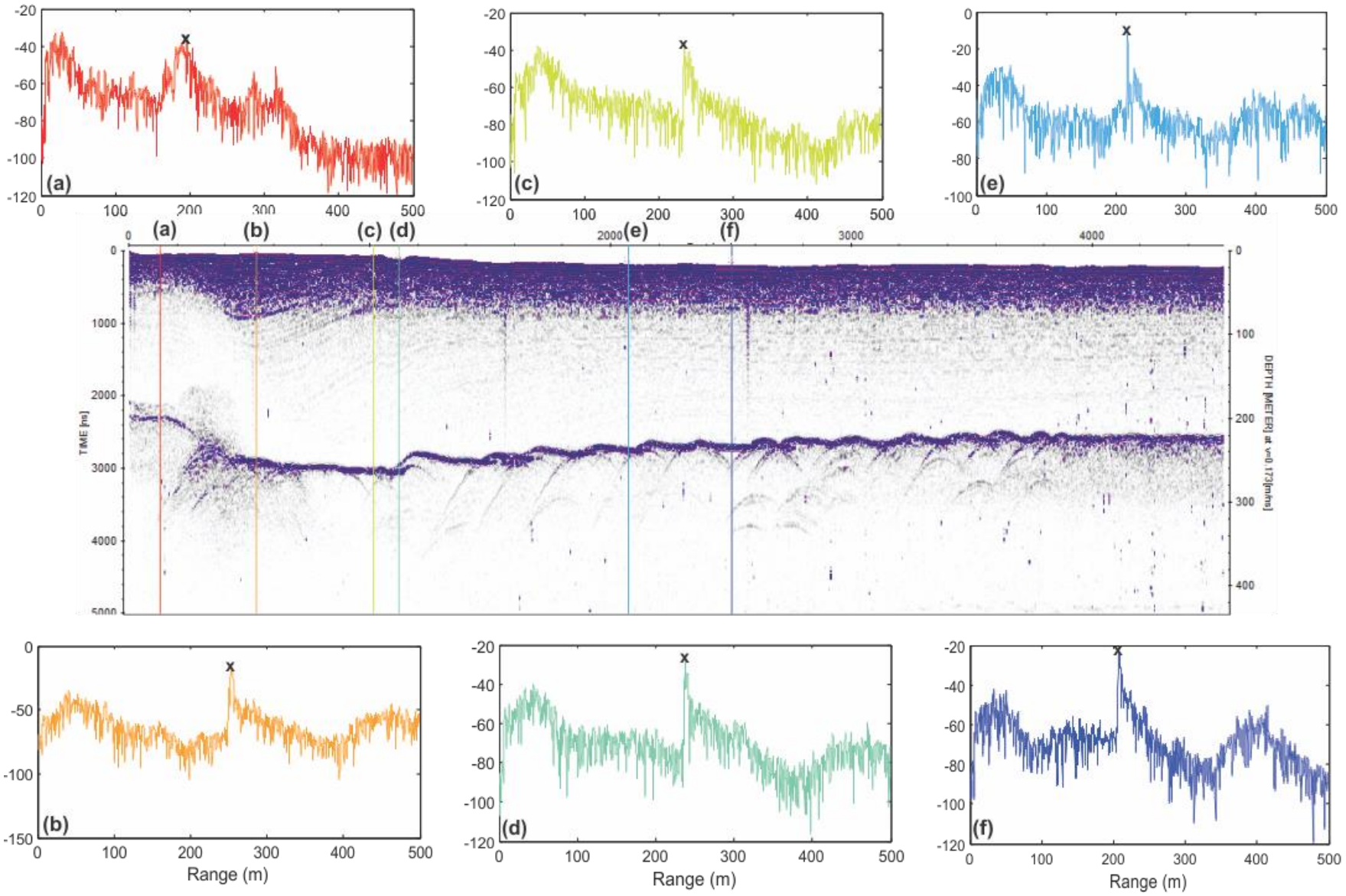

Figure 30. *Six examples of ApRES traces along the central GPR profile. The base of the ice shelf is identified with an x in the small panels, and the location of each ApRES trace is represented by a vertical line of the same colour on the GPR profile.*

6.3 PHASE SENSITIVE RADAR ON THE RIS

The 21 ApRES sites visited on the RIS display a large variation in their properties across the study area. A qualitative scale is used to describe the strength of the basal reflector and ranges from ‘very weak’ where the ice shelf base is difficult to distinguish to ‘very strong’ where it is characterised by a strong, sharp peak in amplitude (Figure 31).

Weak basal reflections indicate that there is not a sharp boundary between fresh shelf ice and the underlying seawater. This is consistent with observations made using an active seismic source on lines between ApRES sites C, E1, E7 and the camp during the same field campaign, where there was clear distinction between ice and seawater (L. van Haastrecht, personal communication, 21 Feb 2016). Conversely, sites with a strong reflection indicate a clear ice to seawater transition.

There appears to be a weak relationship between signal strength and visible surface features. The sites with strong reflections (T1-T3) are located on ice that has originated from Byrd glacier, whereas the weaker sites T4-T6 lie in the suture zone between two glacial flow units. This relationship is not consistent across the entire field area, especially the sites south of T6 which are located on ice which has been part of the ice shelf for much longer than these northern points. This does not imply that a relationship does not exist, just that it is not visible in satellite imagery where snow accumulation may have dampened/smoothed the appearance of these features on the ice shelf over time.

There are three sites where the signal is badly clipped (T1, T2, and T3) so strain and melt/freezing cannot be calculated for these locations. However, as discussed in section 5.1.2.3 ice thickness can still be determined for these sites.

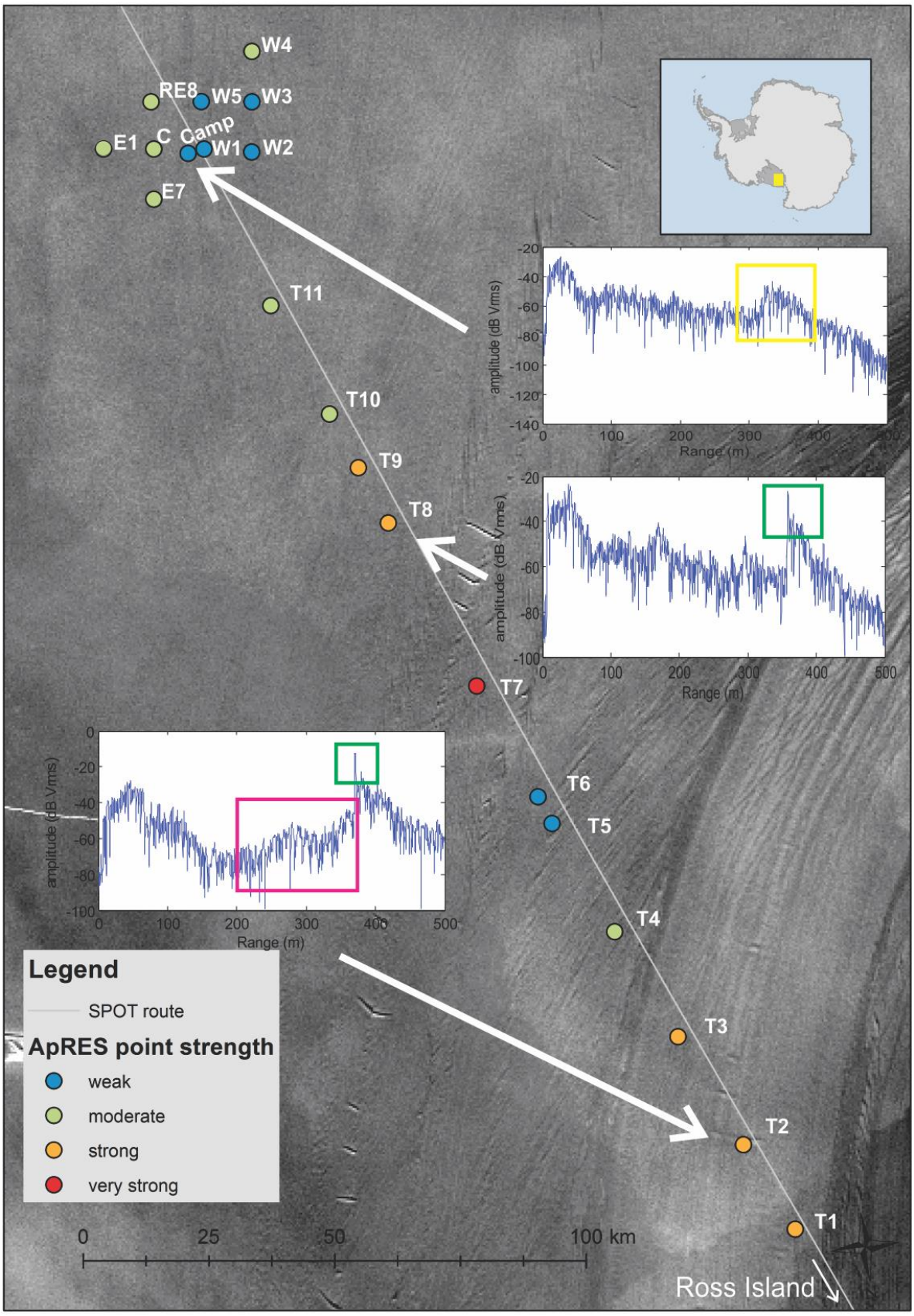

Figure 31. *The strength of the basal reflection at the ApRES sites, with examples of a 'weak' (yellow box) and strong (green box) basal reflector. Note the ramping up of the amplitude value in the pink box, this indicates that the signal has been clipped. The background is a MOA image which has been stretched to emphasise the flow features at the surface. The thick band of ice visible in the lower right is ice from the Byrd glacier.*

6.3.1 Ice thickness from ApRES

The thickness of the ice shelf at each ApRES site is calculated by applying a constant radar velocity of 0.169 m/ns, then manually selecting the thickness from a plot of amplitude against depth, followed by the application of the firn correction. For 'strong' reflections, the base is defined by a sharp peak in the amplitude. For the 'weak' reflections, the base is identified as a gradual increase in amplitude. This makes it difficult to identify the true base, which could be anywhere between the initial increase in amplitude or the peak. For these sites, thickness is defined to be the mid-point on this amplitude ramp, with uncertainties extending out to cover the entire range (e_m).

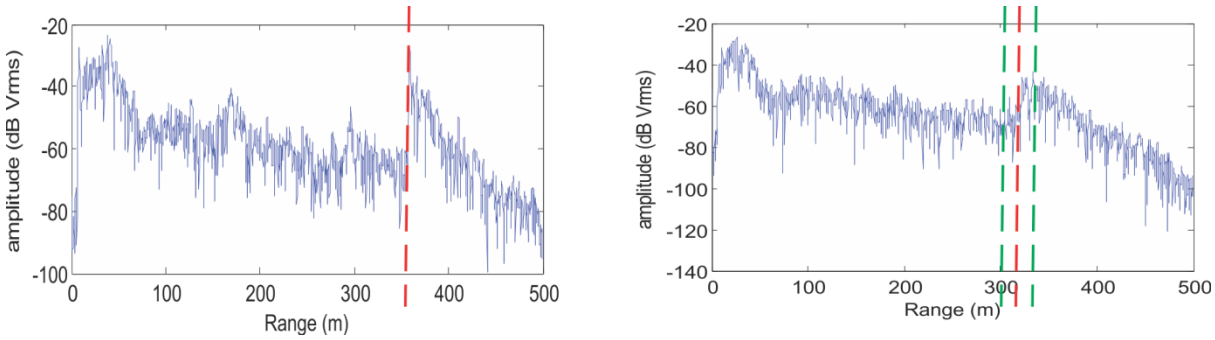

Figure 32. *Ice thickness (red line) at point T8 (left) and the campsite (right). The two green lines represent the top and bottom of the amplitude ramp and are used to define the uncertainty in ice thickness.*

Measured ice thickness is 300-400 m with an increasing trend (correlation coefficient of 0.76 between thickness and latitude) along the SPOT route towards Ross Island (Table 4). This increase in thickness is due to the large inflow of ice from nearby Transantarctic Mountain glaciers.

6.3.2 Presence and thickness of marine ice

The ApRES sites which are characterised as having a 'very weak' to 'moderate' basal reflector are interpreted to be underlain by a layer of marine ice. Although marine ice is saline and has a large dielectric contrast to fresh ice, previous boreholes into marine ice have shown that there is not a sharp transition but a zone across which the salinity and structure of the ice changes from meteoric to marine ice (Craven et al., 2009). In this case the expected radar signal would not be characterised by a sharp peak, but rather a gradual change in the reflectivity properties. This interpretation matches the observed ApRES traces.

The thickness of the marine ice layer cannot be deduced from radar data alone due to EM wave attenuation. To estimate the thickness of the marine ice layer, ice thickness measured

by ApRES is compared to ice thickness as calculated from satellite measurements (section 4.2.3). This is calculated for all sites regardless of the strength of the basal reflector. The thickness of the ApRES points along the SPOT road are plotted against the Griggs and Bamber (2011) thickness at the same point and the difference represents marine ice (Figure 33). For the sites where the Griggs and Bamber (2011) thickness is greater than the ApRES, this indicates that there is a mass of marine ice providing additional buoyancy to the ice shelf. Towards Ross Island the ApRES points are often thicker than the Griggs and Bamber (2011) points, even for the strong reflectors (Figure 31) where the two thicknesses should be identical. This indicates an error in the satellite method rather than a physical feature as this implies 'negative marine ice'. This result provides a basis for discussion on the accuracy of the satellite derived ice thickness in this area.

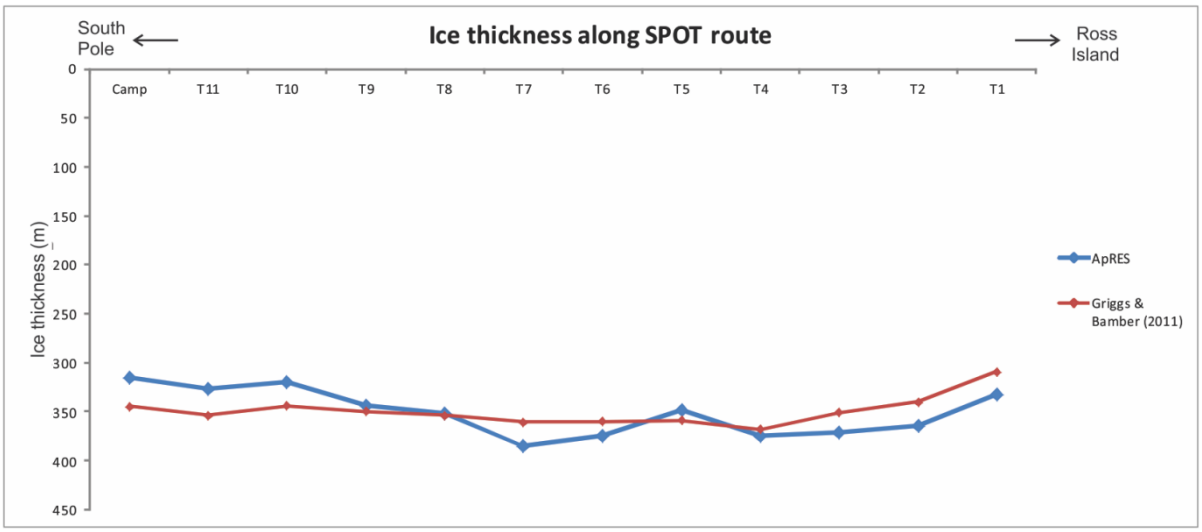

Figure 33. *Ice thickness for the ApRES sites along the SPOT road.*

6.3.3 Calculations of vertical strain

6.3.3.1 Vertical strain from surface velocity measured by satellites

In order to minimise the error and smooth variation, strain was calculated from the MEaSUREs dataset (Rignot et al., 2011b) by fitting a linear regression model to 11 data points in both x and y directions. This is equivalent to 9.9 km and this interval was chosen as it smoothed the velocity data sufficiently without removing the signature from features such as crevasses, shear margins and compression zones.

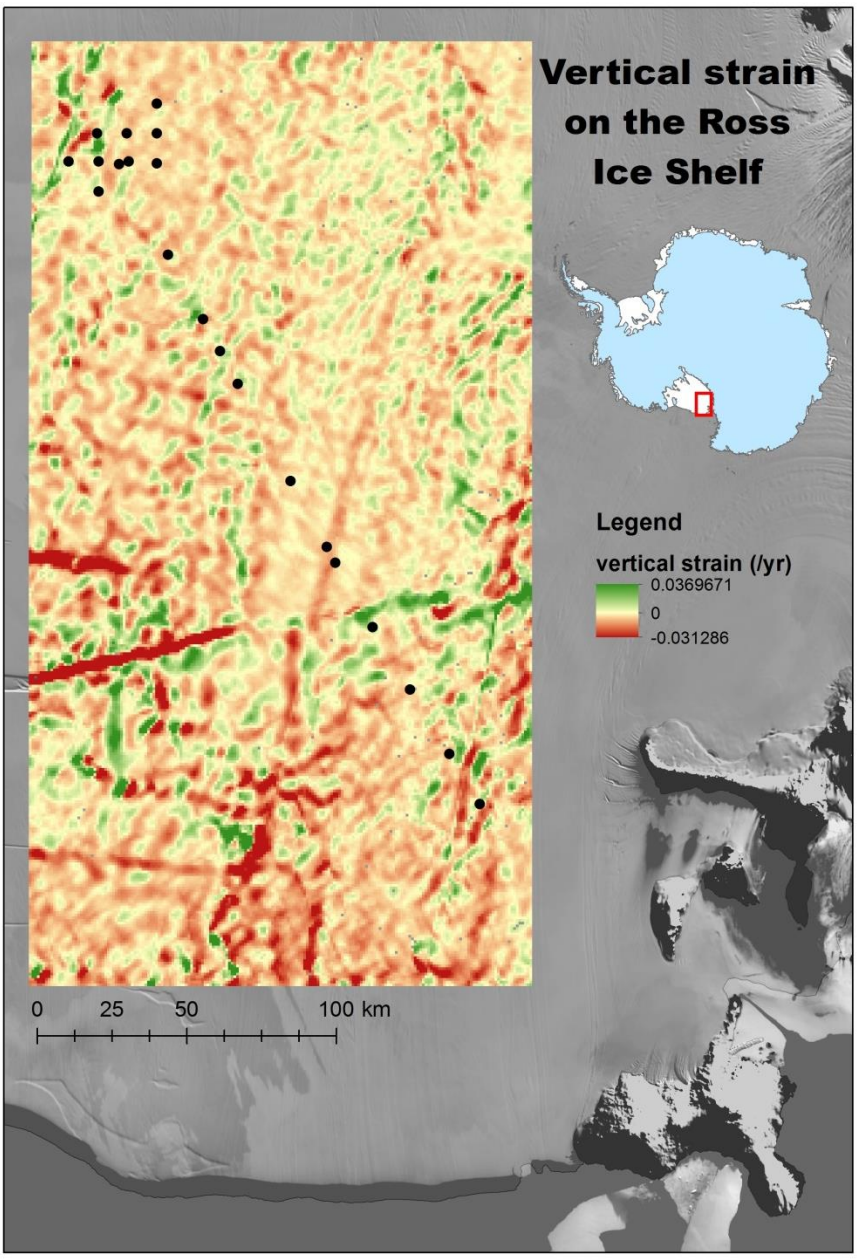

Figure 34. *Vertical strain on the Ross Ice Shelf calculated from 900 m MEaSUREs velocity data. Negative (red) strain is where the ice shelf is thinning. Thickening occurs where strain is positive (green). The black dots are sites where ApRES measurements are made.*

As can clearly be seen in Figure 34, the strain derived from satellite-based velocity measurements is extremely variable over short distances. Much of this variability is randomly distributed and is likely to come from measurement error rather than physical properties of the ice shelf.

6.3.3.2 Vertical strain from ApRES radar

The algorithm for calculating strain from repeat ApRES data in MATLAB involves identifying identical layers in measurements taken at the same location. The distance

between individual layers are compared and a linear strain model is fitted to differences in this distance. An error is also estimated based on the residuals of the data compared to the model.

In order to calculate strain using this method, the depth of the firn layer is defined. In this case, a firn depth of 60 m was applied to all sites (van den Broeke, 2008). A rough estimate of the firn depth by extrapolating the density measurements for the two firn cores (C and W3) to the firn-ice transition gave this depth to be 61 m and 43 m respectively which is consistent with the modelled value. Strain cannot be calculated for points T1-T3 due to clipping, and T5 due to an inability to sufficiently match layers during the processing.

For the remaining 17 points, the value of strain ranges from -0.00180 /year to 0.00050 /year, with a median error of 29% (Table 4). The only point where the strain rate is exceeded by the error is W3. Repeating the calculation with a firn depth of 43 m provides an error which is a factor of 12.4 times larger than the strain. If this point is excluded there is a positive correlation of 0.62 between the value of the strain and the relative error. There is no relationship between the strain error and the basal reflectivity strength.

Generally, the large errors are due to the small time period between repeat measurements (dt). An analysis of the relationship between the time period and the strain error showed that there was actually a very weak negative correlation (-0.058), but this can be neglected given the small sample size, and that even the longest time period of only 2 weeks is probably not a sufficient length of time to measure strain. The ice will have only moved approximately 20 m within this time so will not have been subject to any major changing stress fields or melt regimes.

Table 4. *The thickness (corrected for firn), thickness uncertainty, strain rate and strain error for the ApRES points on the RIS. A positive (negative) strain rate corresponds to thickening (thinning) of the ice shelf. The relative error is the absolute value of error/strain rate. Gaps in the table indicate where that value could not be calculated. The spatial distribution of points is displayed in Figure 31.*

Site name	dt (days)	Ice thickness (m)	Thickness range (e_m)	ApRES strain rate (/yr)	ApRES strain rate error (/yr)	Relative error
Camp	8.4243	315	13	0.00050	0.00023	0.46
W1	7.7822	321	13	-0.00055	0.00009	0.16
W2	7.2795	304	9	-0.00049	0.00039	0.80
W3	5.8315	318	15	0.00006	0.00017	3.00
W4	5.8216	310	3	-0.00130	0.00013	0.10
W5	5.8015	321	16	-0.00180	0.00029	0.16
C	7.1588	325	23	-0.00038	0.00010	0.27
E1	7.2365	312	5	-0.00064	0.00021	0.33
E7	7.3263	335	4	-0.00060	0.00010	0.17
RE8	5.7699	325	5	-0.00090	0.00011	0.12
T11	10.7974	327	5	0.00034	0.00019	0.56
T10	10.9868	320	2	0.00041	0.00015	0.36
T9	11.0968	344	4	-0.00035	0.00007	0.20
T8	11.1953	352	0	-0.00034	0.00011	0.33
T7	12.5465	385	0	-0.00059	0.00009	0.16
T6	12.7039	375	34	0.00042	0.00039	0.93
T5		348	27			
T4	13.8084	375	0	-0.00039	0.00011	0.29
T3		371	0			
T2		364	0			
T1		332	0			

There is no significant correlation between strain and any other measured parameter (Table 5). No obvious relationship exists between vertical strain rates and the visible surface features. This indicates that these features are either too small to impact the strain rates over a larger area, or have been propagated downstream from where they formed and that the ice shelf in this area is moving as a coherent mass rather than a series of glacial units.

Table 5. *Correlation coefficient between position, ice thickness, strain rate and error calculated from the ApRES measurements.*

Correlation coefficient	lat	long	Meteoric ice thickness	marine ice	dt (days)	ApRES strain	ApRES strain error
Latitude	1.00						
Longitude	-0.96	1.00					
Meteoric ice thickness (m)	0.76	-0.71	1.00				
Marine ice thickness (m)	-0.88	0.84	-0.88	1.00			
dt (days)	0.94	-0.83	0.81	-0.73	1.00		
ApRES strain rate (/year)	0.34	-0.27	0.16	-0.07	0.51	1.00	
ApRES strain error	-0.01	-0.06	-0.15	0.16	-0.06	0.13	1.00

6.3.4 Basal melting/freezing from ApRES

The presence of marine ice excludes a number of these sites from basal melting/freezing calculations. With the additional exclusion of the clipped points (T1-3) and T5, only three sites remain where basal melting/freezing can be investigated. Using the strain rate and error calculated above, the basal melting rate of each site is given in Table 6.

Table 6. *The basal melt rates and error for ApRES sites T7, T8, and T9. Note that a negative melt rate corresponds to basal freezing.*

Site	**Basal melt rate (m/yr)**	**Melt error (m/yr)**
T7	-0.0528	0.0186
T8	0.0059	0.0197
T9	0.0529	0.0115

The error for site T8 exceeds the basal melt rate, but between T9 and T7 (a distance of 50 km) there is a transition from a small amount of melting to a small amount of freezing. Regardless, it is impossible to determine regional variability in melting from these two points without better knowledge of the ocean circulation and how it helps redistribute mass.

7 DISCUSSION

7.1 THE SOUTHERN MCMURDO ICE SHELF

The SMIS near Minna Bluff is characterised by marine ice and strong surface ablation features (Clifford, 2005). In contrast, we observe that the accumulation zone near White Island is characterised by a strong meteoric ice–seawater interface and net surface accumulation. These observations indicate that the processes acting on the SMIS, which is a small ice shelf, have large spatial variability and observations made in the ablation zone cannot be extended to the accumulation zone.

7.1.1 SMIS grounding zone processes examined with radar

The slow velocity of the SMIS at the grounding line allows internal and basal processes to be examined with radar that may otherwise be obscured by fast flowing ice. Changes in time can be considered without applying spatial corrections due to ice velocity which ranges from ≈2 ma^{-1} near the grounding line to ≈7 ma^{-1} at the southernmost extent of the study area (Rack et al., 2016). The flow direction is roughly parallel to, with a small component across, the grounding line. Structures within and at the base of the ice shelf reveal important information about the processes occurring at the ice–water interface and within the ice shelf as a whole. These measurements will contribute to a model to invert the tidal flexure pattern to determine ice thickness from satellites (Wild et al., 2016). It is important to be able to characterise and understand the impact different features have on ice mechanics and thickness.

The observed features and their impact on the ice shelf and its stability are discussed separately below. Figure 35 is a schematic of the processes acting in the grounding zone of the accumulation region of the SMIS.

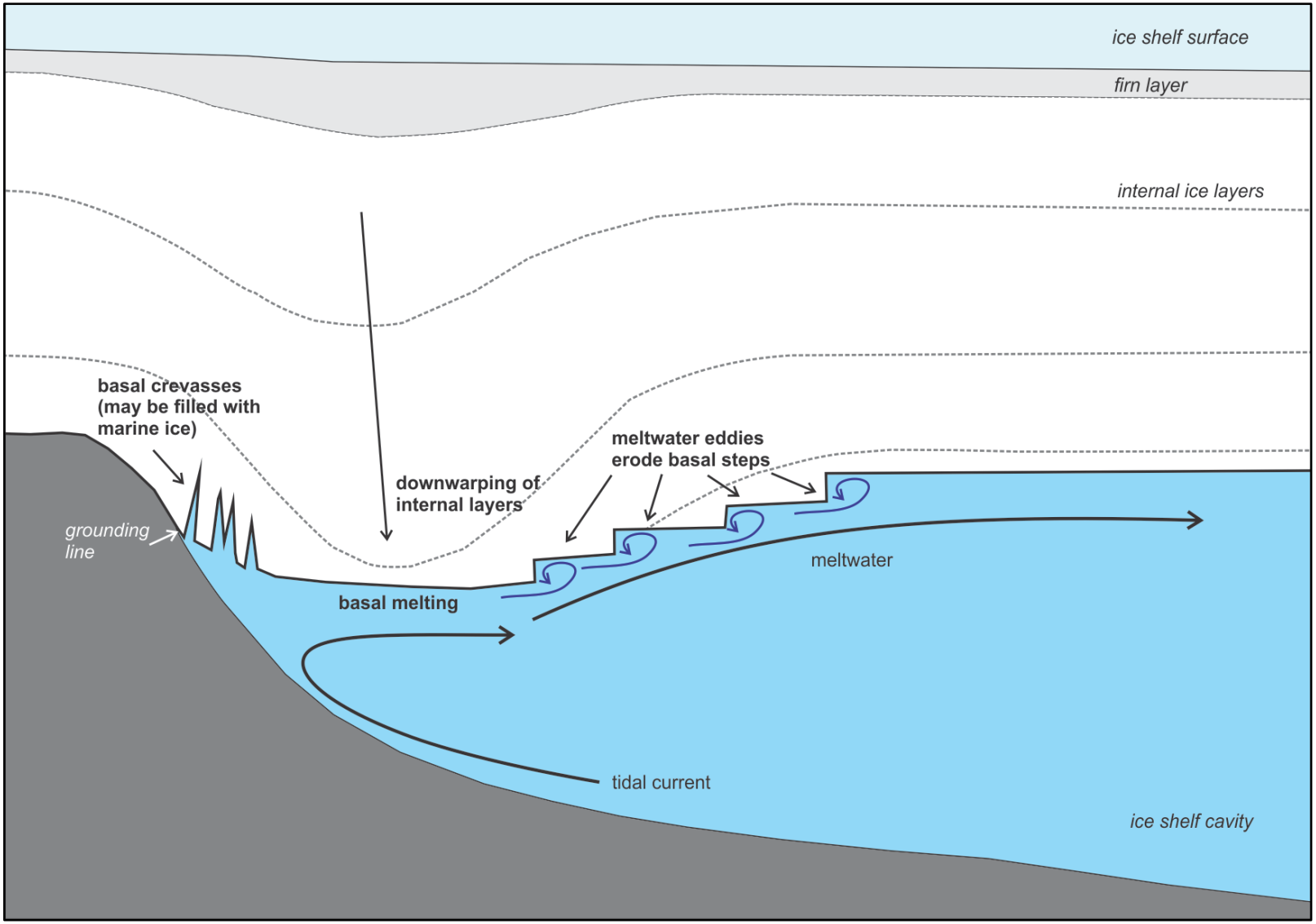

Figure 35. *Schematic of the processes occurring within the grounding zone of the Southern McMurdo Ice Shelf.*

1.1.1.1 Ice thickness and radar reflectivity

The distribution of ice thickness is typical of a grounding line; thickest where the ice has just come afloat and becoming progressively thinner further out. Thicknesses in this area are greater than those measured by Clifford (2005) further south. This is consistent with the knowledge that ice flows, due to gravitational creep as a result of the ice thickness gradient, past White Island and is deflected towards Minna Bluff by Black Island.

A simple comparison of the amplitude of the basal reflector reveals different basal zones that are distinguishable from their appearance in the radargram and can be grouped into different classes. Applying this method to larger ice shelves would require extra complexities to be incorporated into the algorithm including a correction for signal attenuation with depth and a systematic method of defining the range of the reflector.

1.1.1.2 Downwarping of internal layers

Downwarping is the dominant internal feature at the grounding line of White Island but the phenomena is rarely encountered on ice shelves as normally the ice moves through the grounding zone faster than downwarped layers can form. As a result, it has only been documented at the grounding line of ice shelves which are slow moving/stationary or have large melt rates, and where the grounding line has been stable for hundreds of years (Catania et al., 2006; Catania et al., 2010). Downwarping may be related to increased accumulation due to wind redistribution, so using the dipping internal layers to calculate basal melting (Catania et al., 2006) requires an accurate knowledge of accumulation. As annual accumulation was not measured in sufficient detail in the field, an attempt at modelling the rate of melting could not be made here.

On the SMIS, recently deposited layers demonstrate downwarping so it is likely that the modern grounding line still remains exposed to localised melting. For melting to occur a heat source is required. Given that the spatial distribution of the downwarped layers is parallel to the grounding line the source here is most likely tidal/ocean circulation in the ice shelf cavity as opposed to subglacial drainage which is not usually found outside of ice streams (Catania et al., 2010), or geothermal heating. Localised melting due to interaction with the ocean requires the inflow of warm, saline water, and some vertical mixing to promote the transfer of heat in these waters into the ice shelf. Mixing by tidal currents is strongest where the water column is thin (<100 m) (MacAyeal, 1984) such as near grounding lines. The maximum tidal amplitude measured with GPS 4.4 km from the

grounding line on the freely floating part of the ice shelf is in the order of 0.6 m (C. Wild, personal communications, September 27, 2016) which is sufficient to transport warmer water to the grounding line. Using downwarped layers to model basal melt rates do not provide absolute values, but rather rates relative to the background melting. Ocean circulation models are too coarse to predict spatial variability in melt rates due to subtle changes in the grounding line geometry, but can be used to estimate the background rate (Catania et al., 2010). There is some evidence that changes in surface slope at the grounding line can be used as a proxy for basal melting (Catania et al., 2010), but this needs to be validated at more locations and with direct measurements of basal melting.

Ocean circulation beneath the SMIS is poorly understood despite being a possible source of outflow/inflow for the RIS. This is mainly because models of ocean circulation beneath the RIS poorly consider the SMIS (e.g. Holland et al., 2003), but also due a lack of direct measurements. The water column has a maximum depth of only ≈700 m in the centre of the ice shelf (Johnston et al., 2008). It is unlikely that a shallow thermohaline circulation exists beneath the SMIS cavity as the ice shelf is tens of kilometres from the open ocean and White Island, Black Island and White Strait create a barrier to oceanic flow (Koch et al., 2015).

Significant marine ice is observed in the ablation area of the SMIS (Clifford, 2005; Fitzsimons et al., 2012; Koch et al., 2015). Isotopic analysis revealed that up to 5% of the marine ice is formed from melted meteoric ice (Koch et al., 2015). Koch et al. (2015) claim that a potential source of the freshwater is due to enhanced basal melt rates under the RIS near Minna Bluff, but they do admit that the ice pump mechanism here is weak. It can now be argued that a source of freshwater may be basal melting near the grounding line of the accumulation zone of the SMIS, which then buoyantly rises beneath the ice shelf to be incorporated into marine ice in the southern ablation zone. This does not exclude the possibility of meltwater flowing from the RIS but it may be a smaller contributing factor.

1.1.1.3 Basal crevasses at the grounding line

Basal crevasses are commonly found at or near grounding lines in response to tidal or shear stresses (e.g. Catania et al., 2010; Jezek & Bentley, 1983; Peters et al., 2005; Riger-Kusk, 2011). They are much narrower than basal channels which can also form at the grounding line but can be a result of concentrated melting (Marsh et al., 2016).

The geometry, distribution and orientation of basal crevasses can reveal important information about the stress conditions at the base of the ice shelf (Jacobel et al., 2014). Crevasses are often orientated normal to the principal stress but have also been observed at an oblique angle (Jacobel et al., 2014; Jezek et al., 1979). Basal crevasses at the grounding line of the SMIS are aligned roughly parallel to the grounding line. Coincidentally this is also in the direction of ice flow so any longitudinal shearing at the grounding line has a negligible effect on the orientation of the basal crevasses. This unique flow field allows us to conclude that the crevasses are not caused by a changing stress field as the ice flows across the grounding line. Therefore, the crevasses are a manifestation of tidal flexure and are likely kept open by the inflow of warm water to the grounding line which either directly contributes to the growth of the crevasses, or by producing meltwater near the grounding line which buoyantly rises into the crevasse and refreezes as marine ice. Given the extended length of time the ice shelf has been relatively stationary, it is not likely that these crevasses are new features which are currently experiencing growth, but are rather maintained by a dynamic equilibrium between tidal flexure, melting and freezing. Unfortunately, the radar return from these crevasses was too complex to examine if there was sea-water or marine ice within them.

The basal crevasses observed here have important implications for tidal bending patterns as they alter the ice stiffness which may be misinterpreted as a change in ice thickness or Young's Modulus (Rosier et al., 2016). This is especially important for the inversion of the tidal flexure profiles to calculate ice thickness which is a key factor in mass flux across the grounding line (Marsh et al., 2014).

1.1.1.4 Basal steps

Zone 4 in the GPR profiles is characterised by a series of semi-periodic steps. These features decrease the ice thickness away from the grounding line as sudden vertical changes, followed by a smooth, flat terrace. Similar features have been observed with radar at the grounding line of Ice Stream C (Peters et al., 2005) and the Darwin Hatherton glacier (Riger-Kusk, 2011), and adjacent to basal melt channels on Petermann glacier, Greenland and Pine Island Glacier (Dutrieux et al., 2014) but are not commonly recorded.

While Peters et al. (2005) describe these features as jumbled blocks of ice, internal layers are observed through the entire depth of the SMIS and they do not display any distortion that would support this hypothesis. Dutrieux et al. (2014) argue that these features are

formed when meltwater rises upwards under the base of the ice shelf and as it gains velocity it mixes with warmer waters below which allow heat to contact the ice shelf base and facilitates further melting. Repetition of this process creates periodic steps which have a complex shape but are orientated mostly perpendicular to the thickness gradient, similar to what is observed on the SMIS. In relation to these occurring at the grounding line, Riger-Kusk (2011) discusses that steps are formed because of the complex interaction between tidal flexure which creates cracks and basal melting freezing.

On the SMIS it is plausible that meltwater formed near the grounding line is responsible for the creation of basal steps. As the meltwater ascends beneath the ice shelf it mixes with warmer/saltier waters as proposed by Dutrieux et al. (2014). When the flow encounters irregularities in the ice shelf base an eddy is created immediately downstream which facilitates melting, in a process that is similar to the formation of aeolian sand dunes. As these features extend to the boundary of tidal flexure in InSAR imagery it is possible that irregularities may have initially been caused by tidal bending. The stability of the grounding line and the very low ice flow results in ice that is exposed to this process for a long time which allows for the creation and maintenance of steps which are a characteristic feature of the ice shelf base. This is in contrast to Pine Island Glacier, where high melts facilitate the formation of basal steps (Dutrieux et al., 2014).

Other possible explanations for the formation of these features can be ruled out here. These include; basal steps are old crevasses that formed at the grounding line (similar to what is currently observed in zone 2) and have either since moved away (due to ice flow or grounding line retreat), exposing these crevasses to differential melting; or they are a result of shearing as the ice shelf flows against rather than across the grounding line. However, for the former to be possible there has either been; significant grounding line retreat, but if this were the case downwarping wouldn't be observed; or a large change in velocity (magnitude and direction), although there is no deformation of internal layers to support this; or they were initially huge crevasses which are slowly being eroded, which would require the ice-ocean interaction to be very different to what is currently observed given that modern crevasses penetrate roughly 5% of the ice shelf thickness. If these steps are the result of longitudinal shearing, there should be significant deformation of the internal layers directly above them which is not observed.

Dutrieux et al. (2014) argue that these features may be more common than have currently been observed, but can only be detected by sub-ice imaging radar that operate at high resolution. Airborne and satellite radar which are commonly used do not have the required accuracy and a stepped base may appear as a smooth slope interrupted by basal crevasses. Another reason for their rarity may be that they only form under certain circumstances, such as on a stagnant ice shelf, or where melt rate is of significant magnitude to oppose the advection of ice through this zone by ice flow.

7.1.2 Stability of the SMIS

The grounding line of the SMIS at White Island lies on a prograde rock slope so it is not immediately vulnerable to grounding line retreat. As the mass balance of the SMIS is controlled by surface accumulation/ablation and basal melting/freezing rather than flux across the grounding line and iceberg calving, any retreat/collapse of the ice shelf is unlikely to lead to an increase in mass flux from White Island at this location. Regardless, a significant change in mass balance could have implications for the RIS which is currently isolated from the SMIS by the shear zone which extends between Minna Bluff and White Island. Given the current stability, these scenarios are not well understood but could include increased flow of the RIS into the SMIS as the restraining force it provides is reduced/removed.

Due to its unique properties (low flow velocity, significant marine ice deposits, the constant source of positive mass balance from accumulation rather than flow over a grounding line) the SMIS will display a different response to future changes in climate than other ice shelves as it is more vulnerable to changes in surface and basal mass balance rather than ice dynamics. Ice at the grounding line may be particularly sensitive as it is exposed to any changes in the ocean for an extended period of time and takes a long time to move out of the grounding zone where it has the chance to 'recover'. Increased basal melting at the grounding line will be reflected in greater downwarping of internal layers, the associated draw-down of the surface will contribute to ice thinning unless it is balanced by increased accumulation by either direct precipitation or wind distribution. Significant thinning may lead to changes in ice shelf velocity as flow is currently controlled by the thickness gradient.

The process of downwarping reveals that basal melting is not always accompanied by an associated thickness change and so care must be taken when examining static or slow moving ice shelves where melt rates may be underestimated if this is not taken into account.

Vertical strain in the grounding zone does not vary linearly with depth in a grounding zone due to differential horizontal velocity throughout the ice column in response to tides (Jenkins et al., 2006). During a tidal cycle the strain at the surface is opposite in sign to that at the base, for example during high tide there is horizontal extension at the surface and compression at the base, and vice versa during low tide as the ice bends around a neutral internal layer. Previous methods of calculating strain rates that do not penetrate the entire depth of the ice shelf (e.g. surface stake surveys and shallow firn cores) do not accurately capture the variation of strain with depth in a grounding zone. Directly measuring vertical strain with phase sensitive radar in an area of downwarping may also be difficult as the increasing distance between internal layers with depth may complicate the interpretation and could lead to miscalculations of basal melting. Other methods of measuring basal melting in a similar area include modelling downwarping of internal layers and fitting these to observed layers (Catania et al., 2006).

To better understand the stability of the SMIS, the basal melt rates and accumulation in the grounding zone need to be measured. For the ice shelf to remain in steady state, a rough estimate of basal melt rates can be made using snow depth along the central line (Figure 18) by assuming this represents 9 months of accumulation. Away from the grounding line where the internal layers are parallel to the surface, snow depth is 45-70 cm (or 0.60-0.95 ma^{-1}), and surface density is calculated from the firn core to be 344 kgm^{-3}. In this case, basal melt rates of approximately 0.20-0.35 ma^{-1} w.e. are required to maintain steady state. At the grounding line, maximum yearly accumulation, is approximately 2.1 m, and although surface density is likely to be higher than at the firn core due to wind redistribution the surface density from the firn core is used to calculate an estimated minimum annual melt rate of 0.7 m w.e. (or 0.8 m of glacial ice). As stated these are first approximations only and are limited in their extent, however, they do provide estimates of the order of basal melt rates.

7.1.3 Future work

To improve the quantitative understanding of these grounding zone processes further research is required. In particular, an examination of the evolution of downwarping over time would help to validate any relationship between surface slope change/grounding line geometry, basal melting, and the formation and maintenance of basal steps.

In order to achieve these;

- A better understanding of the spatial and temporal variability of accumulation is required;
- Modelled basal melt rates need to be compared to direct measurements with either boreholes or phase sensitive radar;
- Surface elevation needs to be mapped in high resolution to capture changes in surface slope;
- The oceanography and movement of meltwater needs to be better understood.

The southern grounding line of White Island provides an ideal location for any future studies as;

- It is easily and safely accessible, so the site can be visited repeatedly during a season/over many years;
- It is almost stationary, and with the velocity mostly parallel to the grounding line ice is not be quickly advected out of the grounding zone;
- The grounding line has variable geometry over relatively short spatial scales based on the surface slope break in Landsat imagery (Figure 5);
- The high resolution map of ice thickness created here can be used as the basis for ice shelf modelling.

7.2 The Ross Ice Shelf

Phase sensitive radar was successfully deployed at 21 sites on the RIS. Although the initial aim of measuring basal melting/freezing was not achieved for most sites during one season, the results of the radar survey still provide important information about the nature of the ice shelf base. They also are used to validate and compare with satellite-based measurements of ice thickness and vertical strain.

7.2.1 Meteoric and marine ice thickness

A comparison between ice thickness derived from altimetry-based freeboard (Griggs & Bamber, 2011) and radar reveals ice that is thicker in radar measurements than it is from freeboard calculations at seven locations (T1-T7). These result in negative ice anomalies based on the method for calculating marine ice thickness.

As sites T5 and T6 out of the seven that display this anomaly are underlain by marine ice, this is an unexpected result as the ApRES measurements should be smaller than the freeboard derived values. The three possible physical explanations for this can be subsequently ruled out;

a) The structure and mechanical properties of the ice are significantly different for these seven sites compared to the other 14 sites which impacts the velocity of radar in ice. However, using the point T2 as an example, a thickness of 364 m corresponds to a travel time of 2153.8 ns using v=0.169 m/ns. In order to match the freeboard depth of 340 m the velocity would need to be 0.159 m/ns which is significantly less than the theoretical minimum velocity in ice (0.169 ± 0.002 m/ns) (Robin et al., 1969);
b) Ice thickness has increased since the freeboard measurements were made. The freeboard thickness (Griggs & Bamber, 2011) is derived from satellite measurements taken almost 20 years ago. In the time between acquisition of these measurements and the ApRES points the ice shelf has moved approximately 15 km, thus there is a possibility that thicker ice may have been propagated downstream during this time. However, there is no evidence in the freeboard thickness that there is a region of thicker ice within 20 km upstream of the measurement points that may have flowed downstream, neither is there any indication in the vertical strain rates of significant strain thickening in this area.

c) Violation of the hydrostatic assumption. An ice shelf that is heavily crevassed or channelized has a reduced apparent thickness measured with freeboard (Drews, 2015). To account for the observed difference, there should be significant crevassing/channels which would have a surface expression (not observed), and these seven ApRES sites would need to all be located on thicker ice between crevasses, which is unlikely given the required crevasse sizes/density for this to occur.

The inability to explain these anomalies using physical processes indicates that error lies in the data itself. Given that the ApRES has sub-metre precision (Brennan et al., 2014) and the ice shelf base is identified at sites with no marine ice with confidence, error in the radar measurements is insufficient to explain the observed discrepancy between the two methods which is on the order of tens of metres. There is a strong correlation in 'marine ice' thickness with position (-0.88 with latitude and 0.84 with longitude) indicating a systematic error relating to location. As the ApRES thickness is independent of position, this error is most likely related to the Griggs and Bamber (2011) data. The conversion of freeboard to ice thickness using hydrostatic equilibrium requires a number of corrections and assumptions, of particular interest are the geoid and mean dynamic topography which are utilised.

Freeboard, by definition, is the height of the ice shelf above sea level. In the middle of an ice shelf there is no open ocean immediately adjacent to use as a reference, instead models of the geoid are used to determine the height of sea level. Griggs and Bamber (2011) implement the EIGEN-GLO4C geoid which is calculated using satellite data from the GRACE (Gravity Recovery And Climate Experiment) project (Förste et al., 2008). In order to increase the accuracy the model is supplemented with surface gravity data (Förste et al., 2008), however, there is no surface data incorporated into the model near the region of interest and so the resolution remains very coarse. An error of only 1 m in the freeboard is associated with a 10 m error in ice thickness, thus the importance of an accurate geoid is highlighted. Förste et al. (2008) describe the EIGEN-GLO4C geoid as having increased accuracy over previously published geoid models. Regardless, without incorporating high resolution gravity data collected over the RIS in, or using it to validate, the model it is very difficult to assess the accuracy, which could easily contribute to the observed 20 m error in thickness.

Mean dynamic ocean topography (MDOT) is the variation of mean sea level relative to the geoid. It is the response of the ocean to non-tidal effects such as planetary rotation, currents, wind and atmospheric pressure. On the open ocean it can be measured by comparing the geoid height with that of sea level with the effect of the tides removed, but this is not possible underneath an ice shelf. Under large ice shelves, such as the Ross, Filchner-Ronne, and Amery Ice Shelves there can be local currents which are different to the general ocean circulation (Nicholls et al., 2004). Additionally, an accurate understanding of the MDOT in the Southern Ocean is difficult to obtain as there is a lack of in-situ observations, complex topography, strong temporal variability and the presence of sea ice (Griesel et al., 2012). There is significant variation over short spatial scales and differences between separate models in this region can exceed their error (Griesel et al., 2012). Griggs and Bamber (2011) do not apply a MDOT correction to their ice thickness as they argue that extrapolating the MDOT of the Southern Ocean is likely to induce errors similar to or larger than the correction. They estimate that not applying a correction adds a mean error of 1 m with a maximum of 2 m to the freeboard measurement (which is equivalent of up to 20m in ice thickness).

Errors in the modelled sea level may be a result of error in both geoid and MDOT. Values of freeboard made relative to an incorrect sea level will lead to errors in ice thickness, and hence marine ice calculations (Figure 36).

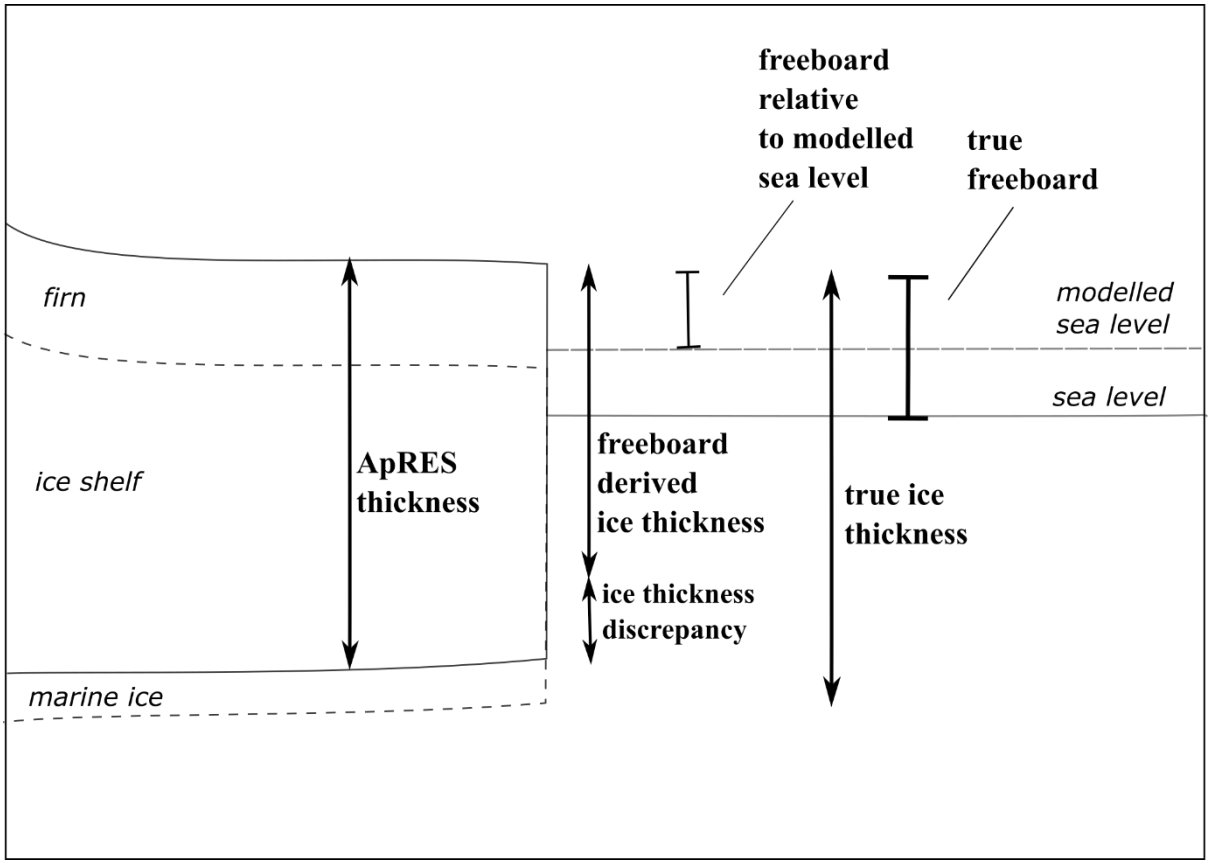

Figure 36. *Schematic demonstrating how the ice thickness anomaly is derived from the marine ice thickness calculation. On an ice shelf freeboard is measured relative to modelled sea level (geoid and MDOT). If this is not consistent with the true sea level, measured values of freeboard will lead to incorrect ice thickness.*

Despite the lack of knowledge, a discussion about whether the MDOT in the study area is significant can still be made. A plume of ice shelf water (ISW) extends north to the east and west of Ross Island and can facilitate the growth of sea ice in the Ross Sea Polynya and McMurdo Sound (Robinson et al., 2014). One suggested source of this ISW, which flows into McMurdo Sound between White Island and Ross Island, is the RIS cavity (Robinson et al., 2014). It is inferred that this ISW, which buoyantly ascends up the base of the ice shelf, has flowed north from its source at the grounding line and whose path takes it past Minna Bluff and the ApRES sites where we find the thickness discrepancy. Furthermore, a series of oceanographic measurements made along the ice shelf front in December 1976 and January 1978 reveals seawater in the western Ross Sea, directly north of our study area, that is the most dense and saline water found in Antarctic oceans (Jacobs et al., 1979). While not explicitly stated in the paper, this region immediately east of Ross Island is the Ross Sea Polynya which is the largest supply of high salinity shelf water (HSSW) in the Ross Sea (Zwally et al., 1985). Despite this, the inflow of HSSW near Ross Island has been largely overlooked (Robinson et al., 2010), however, modelling does

suggest that some HSSW flows south into the cavity along the sea floor (Holland et al., 2003). The presence of these currents in the vicinity of the field area also indicates that the MDOT may be significant in this region.

Although satellite-based measurements may not be of high enough accuracy to compare with direct measurements, often it is not thickness but rather the change in thickness which is of interest for ice shelf stability. If there were significant melting/freezing this could be measured using altimetry, provided that the same geoid model and MDOT correction is used for each dataset. If thickness change is measured using different methods (i.e. radar and altimetry), special care needs to be taken to ensure that the measurements are consistent.

7.2.2 Presence and distribution of marine ice

The presence and distribution of marine ice beneath the RIS closely matches a previous prediction (Neal, 1979). The error introduced to the freeboard measurements due to the geoid and MDOT corrections are of a similar magnitude as the expected marine ice thickness. While the results presented here cannot improve the estimate of marine ice thickness, it is likely that they agree with the magnitude of ice thickness proposed by Neal (1979).

The thickness of the marine ice layer below this part of the RIS is significantly less than what has been observed under the Amery (Fricker et al., 2001) and Filchner-Ronne (Lambrecht et al., 2007) ice shelves. These two ice shelves have much greater drafts at the grounding line than the RIS, which facilitates more meltwater production and hence marine ice formation. Therefore, the processes that effect marine ice formation and stability will be different on the RIS and thus will require studies dedicated to this region.

Regardless of the uncertainties associated with its thickness, the distribution of marine ice still provides useful information. Assuming the error is fairly systematic across the study area, there is a strong negative (-0.88) correlation between the ApRES ice thickness and the calculated marine ice thickness. In other words, marine ice is thicker where meteoric ice is thinner. This suggests that the distribution of marine ice is likely dominated by local basal topography rather than regional ocean circulation, as marine ice forms preferentially where pressure at the ice-water interface is lower.

7.2.3 Vertical strain

The vertical strain rate and associated error from both satellite and ground-based measurements are compared for each ApRES site (Figure 37). While most ApRES points lie within the bounds of uncertainty of the satellite derived points, there is generally poor agreement between the value and often the sign of the strain. The error in the satellite-based calculation exceeds the value of the strain rate at 19 of the 21 points. The MEaSUREs velocity data used in this calculation (Rignot et al., 2015) has estimated errors on the order of <10 m. Although this is a reasonably small error in velocity, when it is propagated through the strain calculations it is enhanced into very large uncertainties. The difference in velocities between neighbouring points, which is the basis of the strain calculation, is of a similar magnitude to the combined error. The strain rate noise in the MEaSUREs dataset is $3x10^{-4}$ yr^{-1} Rignot et al. (2011b). Below this value, satellite track boundaries, thermal noise, and ionospheric noise dominate the strain value. The subtle crosshatch appearance of the vertical strain map (Figure 34) is therefore not a feature of the ice shelf, but an artefact from this dataset.

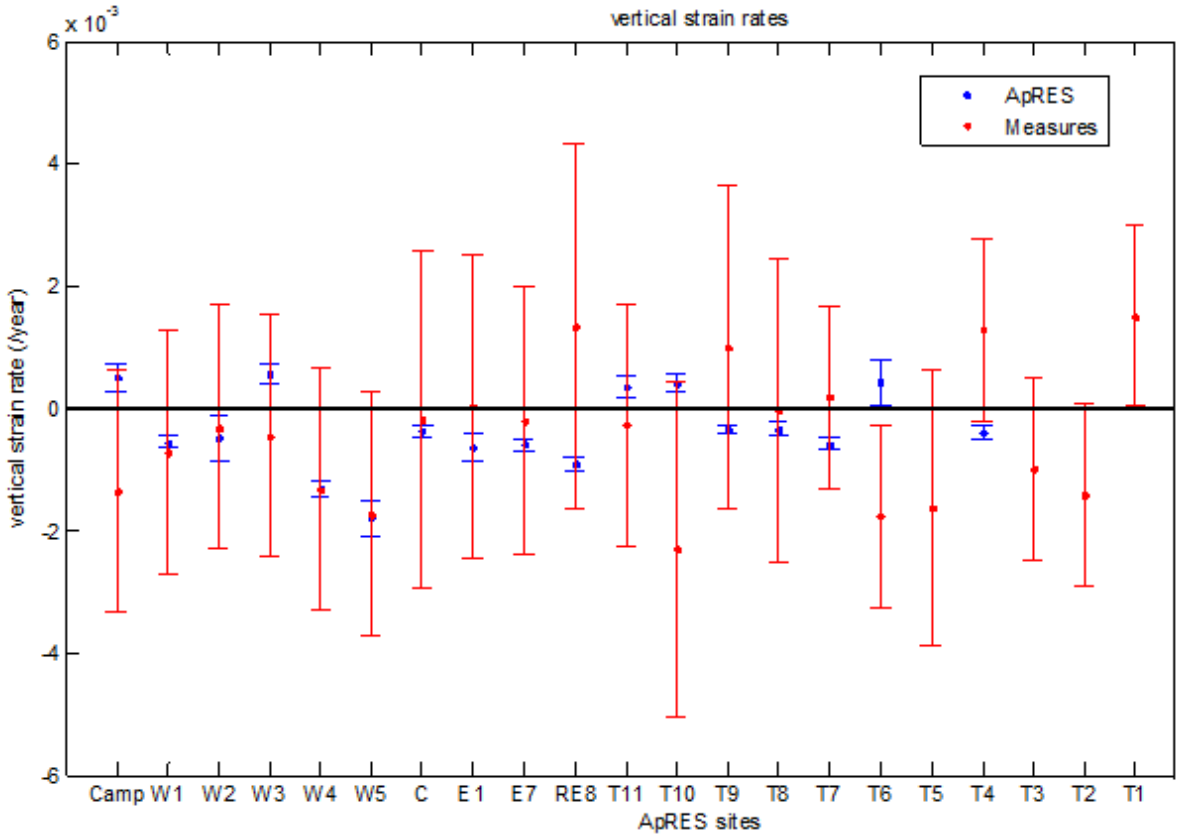

Figure 37. *Vertical strain rate and errors for the 21 field sites on the RIS calculated from the MEaSUREs dataset and with the ApRES.*

In comparison, the error calculated using ApRES is much smaller and even at the extreme uncertainty bounds is the same sign as the calculated value. At each site it can be concluded whether strain thinning or thickening is occurring, but the magnitude at which this is happening remains poorly constrained. Due to the high spatial variability in strain, these measurements cannot be validated. However, they are of a similar magnitude to existing values of strain measured at other locations across the RIS (Crary et al., 1962a), and in the middle of other ice shelves (Craven et al., 2009) using different methods. The order of vertical strain is similar to measurements made on Pine Island Glacier with ApRES (Nicholls et al., 2015).

Despite the relatively large errors in the vertical strain rates calculated using the ApRES, this method still offers a fast and improved way to measure strain. Errors are largely due to the relatively short time between measurements. The selected sites were on the freely floating part of the ice shelf and the three sites which may have been subject to the greatest strain rates (T1-3) due to; their closer proximity to the shear zone, compression of the ice shelf between Ross Island, and their location on ice that has more recently entered the ice shelf; are the same sites where strain could not be calculated due to signal clipping. Unfortunately, these three sites are also the sites with the longest repeat period. In this case the error using ApRES can be reduced by increasing the time period between repeat measurements, however, at locations where there is increased extension or compression, a shorter time period may be desirable to ensure that layers are matched correctly. Therefore, the repeat time measurement needs to be chosen carefully which requires prior knowledge of the conditions of the ice shelf. This can be obtained using satellite velocity measurements, in conjunction with visible surface features (e.g. confluence zones, suture zones, rifts), but these methods do not provide reliable values to examine ice shelf stability.

Single point values of vertical strain do not offer the same level of understanding of ice shelf motion as horizontal strain rates. With the increased interest in ice shelf stability, there is a growing demand in measuring vertical strain as a component of ice thickness change. ApRES offers a way of measuring vertical strain to high resolution provided it is implemented carefully in the field. Each site which is measured by ApRES is equivalent to a single borehole, so it offers significant advantages of being time efficient, inexpensive and highly accurate.

7.2.4 Basal melting/freezing from ApRES

ApRES was unsuccessful in capturing the spatial variability in basal melting/freezing for three reasons;

a. The presence of marine ice and signal clipping eliminated most of the measured sites;
b. For the three sites where the calculation could be made, the relatively large strain rate error is compounded during the basal melt/freeze calculation which resulted in uncertainties that exceeded the values;
c. The three sites which were measured were on a straight line which was neither along or perpendicular to ice flow so spatial variability could not be examined. Additionally, even if an attempt was made, the small sample size would create ambiguous results.

In an area where basal melting/freezing is largely controlled by basal topography, a single ApRES measurement may not be representative of a large area. Therefore, either care needs to be taken to choose sites carefully to avoid this, or melt/freeze rates need to be linked to meteoric ice thickness to be able to apply a point measurement to a larger area.

7.2.5 Future work

Important questions about the current behaviour and future stability of the RIS still remain unanswered. While this thesis has been able to effectively map the presence of marine ice at point locations, knowledge of the thickness, spatial distribution and the temporal behaviour of marine remain poorly understood. Marine ice thickness was unable to be calculated in this thesis due to errors in the geoid and MDOT corrections applied by Griggs and Bamber (2011) in their conversion from altimetry freeboard to thickness. Due to the impenetrability of radar wave through a conductive medium, such as marine ice, measurements of marine ice thickness require direct measurements (which are expensive and time consuming), or significant improvement in modelling of sea level in this area. Since the EIGEN-GLO4C model was published in 2007 there has been considerable effort to gather higher resolution gravity data in Antarctica with 73% of the Antarctic continent, including ice shelves, being covered by 2016 (Scheinert et al., 2016). New geoid models will more accurately represent the area around Ross Island, and a reprocessing of the altimetry data which was used for the Griggs and Bamber (2011) ice shelf thickness should alter the thickness in this region and reduce this error.

Temporal behaviour of the ice shelf base (such as basal melting, freezing or salinity changes of the marine ice) still remains poorly understood. As the distribution of marine ice is largely controlled by ice shelf thickness, it is reasonable to hypothesise that basal melting and freezing displays a similar dependence. This limits the spatial extent a single point measurement represents. ApRES provides the opportunity to make multiple point measurements which gives it a distinctive advantage over other methods such as boreholes, but the repeat time between measurements needs to be much longer than what is presented here. If a survey with a single radar is conducted, ideally measurements would be a year apart in order to capture the annual average rather than the seasonal one which may not be representative of the area as a whole.

1.2 POTENTIAL OF APRES AS A GEOPHYSICAL TOOL

In addition to its designed purpose of measuring vertical strain and basal melting to very high accuracy, the ApRES has large potential as a geophysical tool. A single radar return with the ApRES can be used to calculate meteoric ice thickness and identify the nature of the base (i.e. if there is marine ice). It may be possible that the ApRES can be used to capture changes at the meteoric-marine ice interface such as the evolution of the pore close-off depth. On the Amery ice shelf this has been measured to be 0.3-0.9 m/yr (Craven et al., 2009). In order to achieve this initially the hydraulic connection layer needs to be identified in the radar return so ApRES data would need to be collected simultaneously with measurements made down a borehole. However, once this is established, the ApRES has the potential to extend the observation time.

Despite the possibilities of the ApRES, there are a number of considerations that should be taken into account when using it;

- While the interpretation of weak ApRES reflectors is consistent with those made with other radar (Neal, 1979) it is not suitable for large scale mapping of marine/meteoric ice distribution and thickness. A single measurement takes a significantly longer time than other conventional radar so it is limited to making point measurements. However the ApRES does have the ability to identify the nature of the basal reflector which can be used to assist in locating a suitable spot for long term studies;
- Care needs to be taken that the system is applied consistently at each site (for example the location, orientation and separation of the antennae). This is not an

issue for a system that will remain in-situ, but is important if it will be removed from the site between measurements. This will ensure that the radiation pattern and internal layers are consistent between measurements.

- To capture seasonal variability, the radar needs to be left in the field. If measurements are limited to the summer, any measurements may not represent the current conditions but the yearly average.

When designing a field survey, it is important to consider whether a Lagrangian or Eulerian frame of reference is of interest. If an ApRES system remains in-situ it will move with the ice, whereas removing the radar between measurements means that repeat measurements can be made at the same coordinates, or over the same column of ice. Any time series made in a Lagrangian reference frame will not only be influenced by seasonal variability but also spatial ice-ocean interaction, especially if there are large changes over short distances.

8 CONCLUSION

Ice shelves are an important part of the Antarctic ice sheet as they regulate the flow of ice across the grounding line into the oceans. As ice shelves are in direct contact with both the atmosphere and the ocean they are vulnerable to changes from above and below. The oceans absorb most of the atmospheric warming due to climate change, so the ice-ocean interaction at the ice shelf base has been identified as an area of research where a better understanding is required (IPCC, 2013). In this thesis sub-ice shelf processes and properties have been examined quantitatively and qualitatively by analysing and interpreting measurements made with a ground penetrating and a phase sensitive radar.

In contrast to previous observations of marine ice below the Southern McMurdo Ice Shelf (SMIS) (e.g. Clifford, 2005; Fitzsimons et al., 2012; Koch et al., 2015), the grounding line of White Island is characterised by a meteoric ice–seawater interface which is subject to basal melting. The ice here is thicker than previously reported downstream. Because of these differences, the accumulation zone of the SMIS will demonstrate a different response to climate change than the ablation zone. The appearance of different basal zones in radar reveals important information about the interaction between the ice shelf base and the ocean which may not otherwise be visible in a moving ice shelf. For a stationary ice shelf, basal topography is largely controlled by the presence of meltwater. Meltwater produced at the grounding line can induce further melting close to the grounding zone by mixing with warmer waters and eroding the ice shelf base, but can also contribute to the formation and accumulation of marine ice further downstream. It is likely that the processes that contribute to these observed features are not unique to stationary ice shelves. It can be assumed that either ice moves too fast through the grounding zone for these features to form, or they have been misinterpreted in previous measurements.

Not only does this research contribute to the understanding of grounding line processes, but it also provides information about a previously unstudied area of Antarctica. The results presented here contribute to an increased understanding of the northern SMIS system which has very different properties to what has previously been observed in the surface ablation zone (e.g. Clifford, 2005; Koch et al., 2015; Swithinbank, 1970).

The Ross Ice Shelf (RIS) is different to other large Antarctic ice shelves as marine ice is thin and intermittent compared to the thick, extensive layers of marine ice observed below the Amery and Ronne-Filchner ice shelves (e.g. Fricker et al., 2001; Oerter et al., 1992). With a smaller draft, less meltwater is produced at the grounding line of the RIS and so the ice shelf base further downstream will demonstrate a different interaction with the ocean than these other ice shelves. There is a strong relationship between the presence of marine ice and meteoric ice thickness which indicates that the distribution of marine ice below the RIS is dominantly controlled by basal topography as opposed to oceanic circulation.

Marine ice thickness could not be calculated by comparing radar measurements with satellite-based measurements due to uncertainties in the geoid model and a lack of mean dynamic ocean topography correction used to derive ice thickness from freeboard. Despite this, marine ice is not thicker than the error introduced to these measurements (which is on the order of 20m). This is consistent with what has previously been predicted for this area (Neal, 1979) and observed on the opposite side of the RIS (Zotikov et al., 1980). The presence of marine ice, combined with large errors in measuring vertical strain over a two week period, meant that basal melting/freezing could not be well constrained. The three sites where this was calculated revealed both melting and freezing, however, the value was exceeded by the error. Given the distribution of marine ice, it is possible that there is a correlation between thickness and melting/freezing.

This study has demonstrated some of the potential and limitations of a new phase sensitive radar system as a geophysical imaging tool. While measurements of ice thickness and interpretation of basal conditions are consistent with those made with GPR, the long period required for each measurement means that the ApRES is a tool for precise point measurements at unprecedented accuracy, complementing profiling radars for ice shelf stratigraphy and structure. It can be used for the examination of the ice shelf base as basis to identify suitable field sites for long term studies. ApRES has the potential to replace or complement observation time of other laborious, expensive, and non-invasive methods of measuring strain and basal melting. With each ApRES measurement being equivalent to a single borehole, a network of ApRES sites which are visited periodically would provide invaluable information about spatial and temporal changes within and at the base of the ice shelf.

9 REFERENCES

Alley, K. E., Scambos, T. A., Siegfried, M. R., & Fricker, H. A. (2016). Impacts of warm water on Antarctic ice shelf stability through basal channel formation. *Nature Geoscience*. doi:10.1038/ngeo2675

Arcone, S. A., Spikes, V. B., & Hamilton, G. S. (2005a). Phase structure of radar stratigraphic horizons within Antarctic firn. *Annals of Glaciology, 41*(1), 10-16. doi:10.3189/172756405781813267

Arcone, S. A., Spikes, V. B., & Hamilton, G. S. (2005b). Stratigraphic variation within polar firn caused by differential accumulation and ice flow: interpretation of a 400 MHz short-pulse radar profile from West Antarctica. *Journal of Glaciology, 51*(174), 407-422. doi:10.3189/172756505781829151

Arzeno, I. B., Beardsley, R. C., Limeburner, R., Owens, B., Padman, L., Springer, S. R., . . . Williams, M. J. M. (2014). Ocean variability contributing to basal melt rate near the ice front of Ross Ice Shelf, Antarctica. *Journal of Geophysical Research, 119*(7), 4214-4233. doi:10.1002/2014JC009792

Bailey, J. T., Robin, G. d. Q., & Evans, S. (1964). Radio Echo Sounding of Polar Ice Sheets. *Nature, 204*(4957), 420-421. doi:10.1038/204420a0

Bamber, J. L., Riva, R. E. M., Vermeersen, B. L. A., & LeBrocq, A. M. (2009). Reassessment of the potential sea-level rise from a collapse of the West Antarctic Ice Sheet. *Science, 324*, 901-903.

Bassis, J. N., & Ma, Y. (2015). Evolution of basal crevasses links ice shelf stability to ocean forcing. *Earth and Planetary Science Letters, 409*, 203-211.

Bentley, C. R. (1984). The Ross Ice Shelf Geophysical and Glaciological Survey (RIGGS): Introduction and summary of measurements performed. *The Ross Ice Shelf: Glaciology and Geophysics Antarctic Research Series, 42*(1), 1-20.

Berthier, E., Scambos, T. A., & Shuman, C. A. (2012). Mass loss of Larsen B tributary glaciers (Antarctic Peninsula) unabated since 2002. *Geophysical Research Letters, 39*(13). doi:10.1029/2012GL051755

Bindschadler, R. (1993). Siple Coast Project research of Crary Ice Rise and the mouths of Ice Streams B and C, West Antarctica: review and new perspectives. *Journal of Glaciology, 39*(133), 538-552.

Bindschadler, R., Choi, H., Wichlacz, A., Bingham, R., Bohlander, J., Brunt, K., . . . Young, N. (2011). Getting around Antarctica: new high-resolution mappings of the grounded and freely-floating boundaries of the Antarctic ice sheet created for the International Polar Year. *The Cryosphere, 5*(3), 569-588. doi:10.5194/tc-5-569-2011

Bingham, R. G., Rippin, D. M., Karlsson, N. B., Corr, H. F. J., Ferraccioli, F., Jordan, T. A., . . . Siegert, M. J. (2015). Ice-flow structure and ice dynamic changes in the Weddell Sea sector of West Antarctica from radar-imaged internal layering. *Journal of Geophysical Research, 120*(4), 655-670. doi:10.1002/2014JF003291

Bintanja, R., Oldenborgh, G. J. V., Drijfhout, S. S., Wouters, B., & Katsman, C. A. (2013). Important role for ocean warming and increased ice-shelf melt in Antarctic sea-ice expansion. *Nature Geoscience, 6*(5), 376. doi:10.1038/ngeo1767

Bogorodsky, V., Bentley, C., & Gudmandsen, P. (1985). *Radioglaciology*. Dordrecht, Holland: D. Reidel Publishing Company.

Brennan, P. V., Lok, L. B., Nicholls, K. W., & Corr, H. F. J. (2014). Phase sensitive FMCW radar system for high-precision Antarctic ice shelf profile monitoring. *IET Radar, Sonar and Navigation, 8*(7), 776-786.

Catania, G. A., Conway, H., Raymond, C. F., & Scambos, T. A. (2005). Surface morphology and internal layer stratigraphy in the downstream end of Kamb Ice Stream, West Antarctica. *Journal of Glaciology, 51*(174), 423-431. doi:10.3189/172756505781829142

Catania, G. A., Conway, H., Raymond, C. F., & Scambos, T. A. (2006). Evidence for floatation or near floatation in the mouth of Kamb Ice Stream, West Antarctica, prior to stagnation. *Journal of Geophysical Research, 111*(F1), F01005. doi:10.1029/2005JF000355

Catania, G. A., Hulbe, C., & Conway, H. (2010). Grounding-line basal melt rates determined using radar-derived internal stratigraphy. *Journal of Glaciology, 56*(197), 545-554. doi:10.3189/002214310792447842

Clifford, A. E. (2005). *Physiography, flow characteristics and vulnerability of the Southern McMurdo Ice Shelf, Antarctica.* (Master of Science), University of Otago, Dunedin, New Zealand.

Clough, J. W., & Hansen, B. L. (1979). The Ross Ice Shelf Project. *Science, 203*, 433-434.

Corr, H. F. J., Jenkins, A., Nicholls, K. W., & Doake, C. S. M. (2002). Precise measurement of changes in ice-shelf thickness by phase-sensitive radar to determine basal melt rates. *Geophysical Research Letters, 29*(8).

Corr, H. F. J., Young, N. W., Doake, C. S. M., Skvarca, P., & Rott, H. (1998). Breakup and conditions for stability of the northern Larsen Ice Shelf, Antarctica. *Nature, 391*(6669), 778-780. doi:10.1038/35832

Crary, A. P., Robinson, E. S., Bennett, H. F., & Boyd, W. W. (1962a). Glaciological regime of the Ross Ice Shelf. *Journal of Geophysical Research, 67*(7), 2791-2807.

Crary, A. P., Robinson, E. S., Bennett, H. F., & Boyd, W. W. (1962b). Glaciological studies of the Ross Ice Shelf, Antarctica. *IGY Glaciological Report, 6*.

Craven, M., Allison, I., Fricker, H. A., & Warner, R. (2009). Properties of a marine ice layer under the Amery Ice Shelf, East Antarctica. *Journal of Glaciology, 55*(192), 717-728.

Craven, M., Carsey, F., Behar, A., Matthews, J., Brand, R., Elcheikh, A., . . . Treverrow, A. (2005). Borehole imagery of meteoric and marine ice layers in the Amery Ice Shelf, East Antarctica. *Journal of Glaciology, 51*(172), 75-84. doi:10.3189/172756505781829511

Cuffey, K., & Paterson, W. S. B. (2010). *The physics of glaciers* (Vol. 4th). Burlington, MA: Butterworth-Heinemann/Elsevier.

De Angelis, H., & Skvarca, P. (2003). Glacier surge after ice shelf collapse. *Science, 299*, 1560-1562.

Debenham, F. (1920). A new mode of transportation by ice: The raised marine muds of Southern Victoria Land (Antarctica). *Quarterly Journal of the Geological Society, 75*, 51-76.

Dierckx, M., & Tison, J. L. (2013). Marine ice deformation experiments: an empirical validation of creep parameters. *Geophysical Research Letters, 40*(1), 134-138. doi:10.1029/2012GL054197

Drews, R. (2015). Evolution of ice-shelf channels in Antarctic ice shelves. *The Cryosphere, 9*(3), 1169-1181. doi:10.5194/tc-9-1169-2015

Drews, R., Eisen, O., Steinhage, D., Weikusat, I., Kipfstuhl, S., & Wilhelms, F. (2012). Potential mechanisms for anisotropy in ice-penetrating radar data. *Journal of Glaciology, 58*(209), 613-624.

Dupont, T. K., & Alley, R. B. (2005). Assessment of the importance of ice-shelf buttressing to ice-sheet flow. *Geophysical Research Letters, 32*(4). doi:10.1029/2004GL022024

Dutrieux, P., Stewart, C., Jenkins, A., Nicholls, K. W., Corr, H. F. J., Rignot, E., & Steffen, K. (2014). Basal terraces on melting ice shelves. *Geophysical Research Letters, 41*(15), 5506-5513. doi:10.1002/2014GL060618

Eisen, O., Frezzotti, M., Genthon, C., Isaksson, E., Magand, C., van den Broeke, M. R., . . . Vaughan, D. G. (2008). Ground-based measurements of spatial and temporal variability of snow accumulation in East Antarctica. *Reviews of Geophysics, 46*(2).

Engelhardt, H. (2004). Ice temperature and high geothermal flux at Siple Dome, West Antarctica, from borehole measurements. *Journal of Glaciology, 50*(169), 251-256. doi:10.3189/172756504781830105

Engelhardt, H., & Determann, J. (1987). Borehole evidence for a thick layer of basal ice in the central Ronne Ice Shelf. *Nature, 327*(6120), 318-319. doi:10.1038/327318a0

Fitzsimons, S., Mager, S., Frew, R., Clifford, A., & Wilson, G. (2012). Formation of ice-shelf moraines by accretion of sea water and marine sediment at the southern margin of the McMurdo Ice Shelf, Antarctica. *Annals of Glaciology, 53*(60), 211-220. doi:10.3189/2012AoG60A155

Förste, C., Schmidt, R., Stubenvoll, R., Flechtner, F., Meyer, U., König, R., . . . Esselborn, S. (2008). The GeoForschungsZentrum Potsdam/Groupe de Recherche de Gèodésie Spatiale satellite-only and combined gravity field models: EIGEN-GL04S1 and EIGEN-GL04C. *Journal of Geodesy, 82*(6), 331-346. doi:10.1007/s00190-007-0183-8

Fretwell, P., Pritchard, H. D., Vaughan, D. G., Bamber, J. L., Barrand, N. E., Bell, R., . . . Fujita, S. (2013). Bedmap2: improved ice bed, surface and thickness datasets for Antarctica. *The Cryosphere, 7*(375-393).

Fricker, H. A., Coleman, R., Padman, L., Scambos, T. A., Bohlander, J., & Brunt, K. M. (2009). Mapping the grounding zone of the Amery Ice Shelf, East Antarctica using InSAR, MODIS and ICESat. *Antarctic Science, 21*(5), 515-532. doi:10.1017/S095410200999023X

Fricker, H. A., & Padman, L. (2006). Ice shelf grounding zone structure from ICESat laser altimetry. *Geophysical Research Letters, 33*(15), L15502. doi:10.1029/2006GL026907

Fricker, H. A., Popov, S., Allison, I., & Young, N. (2001). Distribution of marine ice beneath the Amery Ice Shelf, East Antarctica. *Geophysical Research Letters, 28*(11), 2241-2244.

Galton-Fenzi, B. K., Hunter, J. R., Coleman, R., Marsland, S. J., & Warner, R. C. (2012). Modeling the basal melting and marine ice accretion of the Amery Ice Shelf. *Journal of Geophysical Research, 117*(C9). doi:10.1029/2012JC008214

Gillet-Chaulet, F., Hindsmarsh, R. C. A., Corr, H. F. J., King, E. C., & Jenkins, A. (2011). In-situ quantification of ice rheology and direct measurement of the Raymond Effect at Summit, Greenland using a phase-sensitive radar. *Geophysical Research Letters, 38*.

Glasser, N., Goodsell, B., Copland, L., & Lawson, W. (2006). Debris characteristics and ice-shelf dynamics in the ablation region of the McMurdo Ice Shelf, Antarctica. *Journal of Glaciology, 52*(177), 223-234. doi:10.3189/172756506781828692

Glasser, N. F., Holt, T., Fleming, E., & Stevenson, C. (2014). Ice shelf history determined from deformation styles in surface debris. *Antarctic Science, 26*(6), 661-673. doi:10.1017/S0954102014000376

Glasser, N. F., & Scambos, T. A. (2008). A structural glaciological analysis of the 2002 Larsen B ice-shelf collapse. *Journal of Glaciology, 54*(184), 3-16. doi:10.3189/002214308784409017

Goldberg, D., Holland, D. M., & Schoof, C. (2009). Grounding line movement and ice shelf buttressing in marine ice sheets. *Journal of Geophysical Research, 114*(F4). doi:10.1029/2008JF001227

Goldstein, R. M., Engelhardt, H., Kamb, B., & Frolich, R. M. (1993). Satellite Radar Interferometry for Monitoring Ice Sheet Motion: Application to an Antarctic Ice Stream. *Science, 262*(5139), 1525-1530. doi:10.1126/science.262.5139.1525

Griesel, A., Mazloff, M. R., & Gille, S. T. (2012). Mean dynamic topography in the Southern Ocean: Evaluating Antarctic Circumpolar Current transport. *Journal of Geophysical Research, 117*(C1). doi:10.1029/2011JC007573

Griggs, J. A., & Bamber, J. L. (2011). Antarctic ice-shelf thickness from satellite radar altimetry. *Journal of Glaciology, 57*(203), 485-498.

Gudmundsson, G. H. (2013). Ice-shelf buttressing and the stability of marine ice sheets. *The Cryosphere, 7*(2), 647-655. doi:10.5194/tc-7-647-2013

Gutt, J., Cape, M., Dimmler, W., Fillinger, L., Isla, E., Lieb, V., . . . Göteborgs, u. (2013). Shifts in Antarctic megabenthic structure after ice-shelf disintegration in the Larsen area east of the Antarctic Peninsula. *Polar Biology, 36*(6), 895-906. doi:10.1007/s00300-013-1315-7

Hellmer, H. H. (2004). Impact of Antarctic ice shelf basal melting on sea ice and deep ocean properties. *Geophysical Research Letters, 31*(10). doi:10.1029/2004GL019506

Helm, V., Humbert, A., & Miller, H. (2014). Elevation and elevation change of Greenland and Antarctica derived from CryoSat-2. *The Cryosphere, 8*(4), 1539-1559. doi:10.5194/tc-8-1539-2014

Holland, D. M., Jacobs, S. S., & Jenkins, A. (2003). Modelling the ocean circulation beneath the Ross Ice Shelf. *Antarctic Science, 15*(1), 13-23. doi:10.1017/S0954102003001019

Horgan, H. J., Christianson, K., Jacobel, R. W., Anandakrishnan, S., & Alley, R. B. (2013). Sediment deposition at the modern grounding zone of Whillans Ice Stream, West Antarctica. *Geophysical Research Letters, 40*(15), 3934-3939.

Horwath, M., Dietrich, R., Baessler, M., Nixdorf, U., Steinhage, D., Fritzsche, D., . . . Reitmayr, G. (2006). Nivlisen, an Antarctic ice shelf in Dronning Maud Land: geodetic–glaciological results from a combined analysis of ice thickness, ice surface height and ice-flow observations. *Journal of Glaciology, 52*(176), 17-30. doi:10.3189/172756506781828953

Hubbard, B., Tison, J. L., Philippe, M., Heene, B., Pattyn, F., Malone, T., & Freitag, J. (2013). Ice shelf density reconstructed from optical televiewer borehole logging. *Geophysical Research Letters, 40*(22), 5882-5887. doi:10.1002/2013GL058023

Hulbe, C. L., Scambos, T. A., Lee, C.-K., Bohlander, J., & Haran, T. (2013). Recent changes in the flow of the Ross Ice Shelf, West Antarctica. *Earth and Planetary Science Letters, 376*, 54-62. doi:10.1016/j.epsl.2013.06.013

IPCC. (2013). *Climate Change 2013: The Physical Science Basis. Contribution of Working Group I to the Fifth Assessment Report of the Intergovernmental Panel on Climate Change* (T. F. Stocker, D. Qin, G. K. Plattner, M. Tignor, S. K. Allen, J. Boschung, A. Nauels, Y. Xia, V. Bex, & P. M. Midgley Eds.). Cambridge, United Kingdom and New York, NY, USA: Cambridge University Press.

Jacobel, R. W., Christianson, K., Wood, A. C., K.J., D., & Gobel, R. M. (2014). Morphology of basal crevasses at the grounding zone of Whillans Ice Stream, West Antarctica. *Annals of Glaciology, 55*(67), 57-63.

Jacobs, S. S., Gordon, A. L., & Ardai, J. T. (1979). Circulation and Melting Beneath the Ross Ice Shelf. *Science, 203*(4379), 439-443.

Jacobs, S. S., Hellmer, H. H., Doake, C. S. M., Jenkins, A., & Frolich, R. M. (1992). Melting of ice shelves and the mass balance of Antarctica. *Journal of Glaciology, 38*, 375-387.

Jansen, D., Luckman, A., Kulessa, B., Holland, P. R., & King, E. C. (2013). Marine ice formation in a suture zone on the Larsen C Ice Shelf and its influence on ice shelf dynamics. *Journal of Geophysical Research, 118*(3), 1628-1640. doi:10.1002/jgrf.20120

Jenkins, A., Corr, H. F. J., Nicholls, K. W., Stewart, C. L., & Doake, C. S. M. (2006). Interactions between ice and ocean observed with phase-sensitive radar near an Antarctic ice-shelf grounding line. *Journal of Glaciology, 52*(178), 325-346.

Jenkins, A., & Doake, C. S. M. (1991). Ice-Ocean Interaction on Ronne Ice Shelf, Antarctica. *Journal of Geophysical Research, 96*(C1), 791-813. doi:10.1029/90JC01952

Jezek, K. C. (1984). A modified theory of bottom crevasses used as a means for measuring the buttressing effect of ice shelves on inland ice sheets. *Journal of Geophysical Research: Solid Earth, 89*(B3), 1925-1931. doi:10.1029/JB089iB03p01925

Jezek, K. C., & Bentley, C. R. (1983). Field studies of bottom crevasses in the Ross Ice Shelf, Antarctica. *Journal of Glaciology, 29*(118-126).

Jezek, K. C., Bentley, C. R., & Clough, J. W. (1979). Electromagnetic sounding of bottom crevasses on the Ross Ice Shelf, Antarctica. *Journal of Glaciology, 24*, 321-330.

Johnston, L., Wilson, G. S., Gorman, A. R., Henrys, S. A., Horgan, H., Clark, R., & Naish, T. R. (2008). Cenozoic basin evolution beneath the southern McMurdo Ice Shelf, Antarctica. *Global and Planetary Change, 62*(1), 61-76. doi:10.1016/j.gloplacha.2007.11.004

Jol, H. M. (2009). *Ground Penetrating Radar Theory and Applications*. Amsterdam, The Netherlands: Elsevier Science.

Joughin, I., & Alley, R. B. (2011). Stability of the West Antarctic ice sheet in a warming world. *Nature Geoscience, 4*(8), 506-513. doi:10.1038/ngeo1194

Karlsson, N. B., Rippin, D. M., Vaughan, D. G., & Corr, H. F. J. (2009). The internal layering of Pine Island Glacier, West Antarctica, from airborne radar-sounding data. *Annals of Glaciology, 50*(51), 141-146.

Katz, R. F., & Worster, M. G. (2010). Stability of ice-sheet grounding lines. *Proceedings: Mathematical, Physical and Engineering Sciences, 466*, 1597-1620.

Kim, J., Kim, D., Kim, S. H., Ha, H. K., & Lee, S. H. (2015). Disintegration and acceleration of Thwaites Ice Shelf on the Amundsen Sea revealed from remote sensing measurements. *GIScience & Remote Sensing, 52*(4), 498-412. doi:10.1080/15481603.2015.1041766

Kingslake, J., Hindsmarsh, R. C. A., Aoalgeirsdottir, G., Conway, H., Corr, H. F. J., Gillet-Chaulet, F., . . . Pritchard, H. D. (2014). Full-depth englacial vertical ice sheet velocities measured using phase-sensitive radar. *Journal of Geophysical Research, 119*, 2604-2618.

Koch, I., Fitzsimons, S., Samyn, D., & Tison, J.-L. (2015). Marine ice recycling at the southern McMurdo Ice Shelf, Antarctica. *Journal of Glaciology, 61*(228), 689-701. doi:10.3189/2015JoG14J095

Kovacs, A., Gow, A. J., & Morey, R. M. (1995). The in-situ dielectric constant of polar firn revisited. *Cold Regions Science and Technology, 23*(3), 245-256. doi:10.1016/0165-232X(94)00016-Q

Kruetzman, N. C., Rack, W., McDonald, A. J., & George, S. E. (2011). Snow accumulation and compaction derived from GPR data near Ross Island, Antarctica. *The Cryosphere, 5*, 391-404.

Kulessa, B., Jansen, D., Luckman, A. J., King, E. C., & Sammonds, P. R. (2014). Marine ice regulates the future stability of a large Antarctic ice shelf. *Nature communications, 5*, 3707. doi:10.1038/ncomms4707

Lambrecht, A., Sandhäger, H., Vaughan, D. G., & Mayer, C. (2007). New ice thickness maps of Filchner–Ronne Ice Shelf, Antarctica, with specific focus on grounding lines and marine ice. *Antarctic Science, 19*(4), 521-532. doi:10.1017/S0954102007000661

Le Brocq, A. M., Ross, N., Griggs, J. A., Bingham, R. G., Corr, H. F. J., Ferraccioli, F., . . . Siegert, M. J. (2013). Evidence from ice shelves for channelized meltwater flow beneath the Antarctic Ice Sheet. *Nature Geoscience, 6*(11), 945-948. doi:10.1038/ngeo1977

Ligtenberg, S. R. M., Helsen, M. M., & van den Broeke, M. R. (2011). An improved semi-empirical model for the densification of Antarctic firn. *The Cryosphere, 5*, 809-819.

Luckman, A., Jansen, D., Kulessa, B., King, E. C., Sammonds, P., & Benn, D. I. (2012). Basal crevasses in Larsen C Ice Shelf and implications for their global abundance. *The Cryosphere, 6*, 113-123.

MacAyeal, D. R. (1984). Thermohaline circulation below the Ross Ice Shelf - A consequence of tidally induced vertical mixing and basal melting. *Journal of Geophysical Research, 89*(C1), 597-606. doi:10.1029/JC089iC01p00597

MacDonald, W. J. P., & Hatherton, T. (1961). Movement of the Ross Ice Shelf near Scott Base. *Journal of Glaciology, 3*(29), 859-866.

MacGregor, J. A., Catania, G. A., Markowski, M. S., & Andrews, A. G. (2012). Widespread rifting and retreat of ice-shelf margins in the eastern Amundsen Sea Embayment between 1972 and 2011. *Journal of Glaciology, 58*(209), 458-466. doi:10.3189/2012JoG11J262

Makinson, K., King, M. A., Nicholls, K. W., & Hilmar Gudmundsson, G. (2012). Diurnal and semidiurnal tide-induced lateral movement of Ronne Ice Shelf, Antarctica. *Geophysical Research Letters, 39*(10). doi:10.1029/2012GL051636

Marsh, O. J., Fricker, H. A., Siegfried, M. R., Christianson, K., Nicholls, K. W., Corr, H. F. J., & Catania, G. (2016). High basal melting forming a channel at the grounding line of Ross Ice Shelf, Antarctica. *Geophysical Research Letters, 43*(1), 250-255. doi:10.1002/2015GL066612

Marsh, O. J., Rack, W., Golledge, N. R., Lawson, W., & Floricioiu, D. (2014). Grounding-zone ice thickness from InSAR: inverse modelling of tidal elastic bending. *Journal of Glaciology, 60*(221), 526-536. doi:10.3189/2014JoG13J033

Marshall, H.-P., & Koh, G. (2008). FMCW radars for snow research. *Cold Regions Science and Technology, 52*(2), 118-131. doi:10.1016/j.coldregions.2007.04.008

McGrath, D., Steffen, K., Holland, P. R., Scambos, T., Rajaram, H., Abdalati, W., & Rignot, E. (2014). The structure and effect of suture zones in the Larsen C Ice Shelf, Antarctica. *Journal of Geophysical Research, 119*(3), 588-602. doi:10.1002/2013JF002935

McGrath, D., Steffen, K., Scambos, T. A., Rajaram, H., Casassa, G., & Rodriguez Lagos, J. L. (2012). Basal crevasses and associated surface crevassing on the Larsen C ice shelf, Antarctica, and their role in ice-shelf instability. *Annals of Glaciology, 53*(60), 10-18.

Miles, B. W. J., Stokes, C. R., & Jamieson, S. S. R. (2016). Pan–ice-sheet glacier terminus change in East Antarctica reveals sensitivity of Wilkes Land to sea-ice changes. *Science Advances, 2*(5). doi:10.1126/sciadv.1501350

Millgate, T., Holland, P. R., Jenkins, A., & Johnson, H. L. (2013). The effect of basal channels on oceanic ice-shelf melting. *Journal of Geophysical Research, 118*(12), 6951-6964. doi:10.1002/2013JC009402

Monaghan, A. J., Bromwich, D. H., Powers, J. G., & Manning, K. W. (2005). The climate of the McMurdo, Antarctica, region as represented by one year of forecasts from the Antarctic Mesoscale Prediction System. *Journal of Climate, 18*, 1174-1189.

Naish, T., Powell, R., Levy, R., Wilson, G., Scherer, R., Talarico, F., . . . Williams, T. (2009). Obliquity-paced Pliocene West Antarctic ice sheet oscillations. *Nature, 458*(7236), 322-328. doi:10.1029/ 2005PA001153 (2005).

Neal, C. S. (1979). The dynamics of the Ross Ice Shelf revealed by radio echo sounding. *Journal of Glaciology, 24*(90), 295-307.

Nicholls, K. W., Corr, H. F. J., Stewart, C. L., Lok, L. B., Brennan, P. V., & Vaughan, D. G. (2015). A ground-based radar for measuring vertical strain rates and time-varying basal melt rates in ice sheets and shelves. *Journal of Glaciology, 61*(230), 1079-1087. doi:10.3189/2015JoG15J073

Nicholls, K. W., Makinson, K., & Østerhus, S. (2004). Circulation and water masses beneath the northern Ronne Ice Shelf, Antarctica. *Journal of Geophysical Research, 109*(C12), C12017. doi:10.1029/2004JC002302

Oerter, H., Kipfstuhl, J., Determann, J., Miller, H., Wagenbach, D., Minikin, A., & Graft, W. (1992). Evidence for basal marine ice in the Filchner-Ronne ice shelf. *Nature, 358*(6385), 399-401. doi:10.1038/358399a0

Paolo, F. S., Fricker, H. A., & Padman, L. (2015). Volume loss from Antarctic ice shelves is accelerating. *Science, 348*(6232), 327-331. doi:10.1126/science.aaa0940

Paterson, W. S. B. (1976). Vertical strain-rate measurements in an Arctic ice cap and deductions from them. *Journal of Glaciology, 17*(75), 3-12.

Peters, M. E., Blankenship, D. D., & Morse, D. L. (2005). Analysis techniques for coherent airborne radar sounding: Application to West Antarctic ice streams. *Journal of Geophysical Research, 110*(B6), 303-317. doi:10.1029/2004JB003222

Peters, M. E., Blankenship, D. D., Smith, D. E., Holt, J. W., & Kempf, S. D. (2007). The Distribution and Classification of Bottom Crevasses From Radar Sounding of a Large Tabular Iceberg. *IEEE Geoscience and Remote Sensing Letters, 4*(1), 142-146. doi:10.1109/LGRS.2006.887057

Pollard, D., & DeConto, R. M. (2009). Modelling West Antarctic Ice Sheet growth and collapse through the past five million years. *Nature, 458*, 329-333.

Pritchard, H. D., Arthern, R. J., Vaughan, D. G., & Edwards, L. A. (2009). Extensive dynamic thinning on the margins of the Greenland and Antarctic ice sheets. *Nature, 461*(7266), 971-975. doi:10.1038/nature08471

Rack, W., King, M. A., Marsh, O. J., Wild, C. T., & Floricioiu, D. (2016). Analysis of ice shelf flexure and its InSAR representation in the grounding zone of the Southern McMurdo Ice Shelf. *Manuscript in preparation*.

Ragle, R. H., Hansen, B. L., Gow, A., & Patenaude, R. W. (1960). *Deep core drilling in the Ross Ice Shelf, Little America V, Antarctica*. Retrieved from Wilmette, Illinois:

Rebesco, M., Domack, E., Zgur, F., Lavoie, C., Leventer, A., Brachfeld, S., . . . Pettit, E. (2014). Boundary condition of grounding lines prior to collapse, Larsen-B Ice Shelf, Antarctica. *Science, 345*(6202), 1354-1358. doi:10.1126/science.1256697

Reddy, T. E., Holland, D. M., & Arrigo, K. R. (2010). Ross ice shelf cavity circulation, residence time, and melting: Results from a model of oceanic chlorofluorocarbons. *Continental Shelf Research, 30*(7), 733-742. doi:10.1016/j.csr.2010.01.007

Riedel, B., Nixdorf, U., Heinert, M., Eckstaller, A., & Mayer, C. (1999). The response of the Ekstromisen (Antarctica) grounding zone to tidal forcing. *Annals of Glaciology, 29*(1), 239-242. doi:10.3189/172756499781821247

Riger-Kusk, M. (2011). *Ice dynamics of the Darwin-Hatherton glacial system, Transantarctic Mountains, Antarctica.* (Doctor of Philosophy), University of Canterbury, Christchurch, New Zealand.

Rignot, E. (2008). Changes in West Antarctic ice stream dynamics observed with ALOS PALSAR data. *Geophysical Research Letters, 35*(12). doi:10.1029/2008GL033365

Rignot, E., Casassa, G., Gogineni, P., Krabill, W., Rivera, A., & Thomas, R. (2004). Accelerated ice discharge from the Antarctic Peninsula following the collapse of Larsen B ice shelf. *Geophysical Research Letters, 31*. doi:10.1029/2004GL020697

Rignot, E., Jacobs, S. S., Mouginot, J., & Scheuchl, B. (2013). Ice-shelf melting around Antarctica. *Science, 341*(6143), 266-270.

Rignot, E., Mouginot, J., Morlighem, M., Seroussi, H., & Scheuchl, B. (2014). Widespread, rapid grounding line retreat of Pine Island, Thwaites, Smith, and Kohler glaciers, West Antarctica, from 1992 to 2011. *Geophysical Research Letters, 41*(10), 3502-3509. doi:10.1002/2014GL060140

Rignot, E., Mouginot, J., & Scheuchl, B. (2011a). Antarctic grounding line mapping from differential satellite radar interferometry. *Geophysical Research Letters, 38*, L10504. doi:10.1029/2011GL047109

Rignot, E., Mouginot, J., & Scheuchl, B. (2011b). Ice flow of the Antarctic Ice Sheet. *Science, 333*, 1427-1430. doi:10.1126/science.1208336

Rignot, E., Mouginot, J., & Scheuchl, B. (2015). *MEaSUREs InSAR-based Antarctic Ice Velocity Map. Version 1.2*. Retrieved from: https://nsidc.org/data/docs/measures/nsidc0484_rignot/

Robin, G. D. Q., Evans, S., & Bailey, J. T. (1969). Interpretation of Radio Echo Sounding in Polar Ice Sheets. *Philosophical Transactions of the Royal Society of London. Series A, Mathematical and Physical Sciences, 265*(1166), 437-505.

Robinson, N. J., Williams, M. J. M., Barrett, P. J., & Pyne, A. R. (2010). Observations of flow and ice-ocean interaction beneath the McMurdo Ice Shelf, Antarctica. *Journal of Geophysical Research, 115*(C3). doi:10.1029/2008JC005255

Robinson, N. J., Williams, M. J. M., Stevens, C. L., Langhorne, P. J., & Haskell, T. G. (2014). Evolution of a supercooled Ice Shelf Water plume with an actively growing subice platelet matrix. *Journal of Geophysical Research, 119*(6), 3425-3446. doi:10.1002/2013JC009399

Rosier, S. H. R., Marsh, O. J., Rack, W., Gudmundsson, G. H., Wild, C. T., & Ryan, M. R. (2016). On interpreting measurements of ice-shelf flexure. *Manuscript submitted for publication - Journal of Glaciology*.

Rotschky, G., Rack, W., Dierking, W., & Oerter, H. (2006). Retrieving snowpack properties and accumulation estimates from a combination of SAR and scatterometer measurements. *IEEE Transactions on Geoscience and Remote Sensing, 44*(4), 943-956.

Sanderson, T. J. O., & Doake, C. S. M. (1979). Is Vertical Shear in an Ice Shelf Negligible? *Journal of Glaciology, 22*(87), 285-292.

Sasgen, I., Konrad, H., Ivins, E. R., van den Broeke, M. R., Bamber, J. L., Martinec, Z., & Klemann, V. (2013). Antarctic ice-mass balance 2003 to 2012: regional reanalysis of GRACE satellite gravimetry measurements with improved estimate of glacial-isostatic adjustment based on GPS uplift rates. *The Cryosphere, 7*(5), 1499-1512. doi:10.5194/tc-7-1499-2013

Scambos, T. A., Haran, T. M., Fahnestock, M. A., Painter, T. H., & Bohlander, J. (2007). MODIS-based Mosaic of Antarctica (MOA) data sets: Continent-wide surface morphology and snow grain size. *Remote Sensing of Environment, 111*(2), 242-257. doi:10.1016/j.rse.2006.12.020

Scheinert, M., Ferraccioli, F., Schwabe, J., Bell, R., Studinger, M., Damaske, D., . . . Richter, T. D. (2016). New Antarctic gravity anomaly grid for enhanced geodetic and geophysical studies in Antarctica. *Geophysical Research Letters, 43*(2), 600-610. doi:10.1002/2015GL067439

Scheuchl, B., Mouginot, J., Rignot, E., Morlighem, M., & Khazendar, A. (2016). Grounding line retreat of Pope, Smith, and Kohler Glaciers, West Antarctica, measured with Sentinel-1a radar interferometry data. *Geophysical Research Letters, 43*(16), 8572-8579. doi:10.1002/2016GL069287

Shabtaie, S., & Bentley, C. R. (1982). Tabular Icebergs: Implications from Geophysical Studies of Ice Shelves. *Journal of Glaciology, 28*(100), 413-430. doi:10.3198/1982JoG28-100-413-430

Shepherd, A., Lenaerts, J. T. M., Ligtenberg, S. R. M., van Angelen, J. H., van de Berg, W. J., van den Broeke, M. R., & Zwally, H. J. (2012). A Reconciled Estimate of Ice-Sheet Mass Balance. *Science, 338*(6111), 1183-1189. doi:10.1126/science.1228102

Siegert, M. J. (1999). On the origin, nature and uses of Antarctic ice-sheet radio-echo layering. *Progress in Physical Geography, 23*(2), 159-179. doi:10.1177/030913339902300201

Smethie, W. M., & Jacobs, S. S. (2005). Circulation and melting under the Ross Ice Shelf: estimates from evolving CFC, salinity and temperature fields in the Ross Sea. *Deep-Sea Research Part I, 52*(6), 959-978. doi:10.1016/j.dsr.2004.11.016

Stanton, T. P., Shaw, W. J., Truffer, M., Corr, H. F. J., Peters, L. E., Riverman, K. L., . . . Anandakrishnan, S. (2013). Channelized Ice Melting in the Ocean Boundary Layer Beneath Pine Island Glacier, Antarctica. *Science, 341*(6151), 1236-1239.

Stephenson, S. N., Doake, C. S. M., & Horsfall, J. A. C. (1979). Tidal flexure of ice shelves measured by tiltmeter. *Nature, 282*(5738), 496-497. doi:10.1038/282496a0

Stuart, A. W., & Bull, C. (1963). Glaciological Observations on the Ross Ice Shelf near Scott Base, Antarctica. *Journal of Glaciology, 4*(34), 399-413.

Swithinbank, C. W. M. (1970). *Ice movement in the McMurdo Sound area of Antarctica* (Vol. 86): International Association of Scientific Hydrology.

Treverrow, A., Warner, R. C., Budd, W. F., & Craven, M. (2010). Meteoric and marine ice crystal orientation fabrics from the Amery Ice Shelf, East Antarctica. *Journal of Glaciology, 56*(199), 877-890. doi:10.3189/002214310794457353

van den Broeke, M. (2008). Depth and Density of the Antarctic Firn Layer. *Arctic, Antarctic, and Alpine Research, 40*(2), 432-438. doi:10.1657/1523-0430(07-021)[BROEKE]2.0.CO;2

van der Veen, C. J. (1998). Fracture mechanics approach to penetration of bottom crevasses on glaciers. *Cold Regions Science and Technology, 27*(3), 213-223. doi:10.1016/S0165-232X(98)00006-8

Vaughan, D. G. (1994). Investigating tidal flexure on an ice shelf using kinematic GPS. *Annals of Glaciology, 20*(1), 372-376. doi:10.3189/172756494794587375

Vaughan, D. G. (1995). Tidal flexure at ice shelf margins. *Journal of Geophysical Research, 100*(B4), 6213-6224. doi:10.1029/94JB02467

Vaughan, D. G., Comiso, J. C., Allison, I., Carrasco, J., Kaser, G., Kwok, R., . . . Zhang, T. (2013). Observations: Cryosphere. In T. F. Stocker, D. Qin, G. K. Plattner, M. Tignor, S. K. Allen, J. Boschung, A. Nauels, Y. Xia, V. Bex, & P. M. Midgley (Eds.), *Climate Change 2013: The Physical Science Basis. Contribution of Working*

Group I to the Fifth Assessment Report of the Intergovernmental Panel on Climate Change (pp. 317-382). Cambridge, United Kingdom and New York, NY, USA: Cambridge University Press.

Vaughan, D. G., Corr, H. F. J., Bindschadler, R. A., Dutrieux, P., Gudmundsson, G. H., Jenkins, A., . . . Wingham, D. J. (2012). Subglacial melt channels and fracture in the floating part of Pine Island Glacier, Antarctica. *Journal of Geophysical Research, 117*(F3). doi:10.1029/2012JF002360

Walford, M. E. R. (1964). Radio Echo Sounding Through an Ice Shelf. *Nature, 204*(4956), 317-319. doi:10.1038/204317a0

Weertman, J. (1973). *Can a Water-Filled Crevasse Reach the Bottom Surface of a Glacier?* Paper presented at the International Association of Hydrologic Sciences, Wallingford, UK.

Wesche, C., Jansen, D., & Dierking, W. (2013). Calving Fronts of Antarctica: Mapping and Classification. *Remote Sensing, 5*(12), 6305-6322. doi:10.3390/rs5126305

Wild, C. T., Marsh, O. J., & Rack, W. (2016). Viscosity and elasticity: a model-intercomparison of ice-shelf bending in an Antarctic grounding zone. *Manuscript submitted for publication - Journal of Glaciology*.

Young, N. W., & Hyland, G. (2002). Velocity and strain rates derived from InSAR analysis over the Amery Ice Shelf, East Antarctica. *Annals of Glaciology, 34*(1), 228-234. doi:10.3189/172756402781817842

Zhang, D., Sun, B., Ke, C., Cui, X., Li, X., & Guo, J. (2014). Effect of Ice Shelf Changes on Ice Sheet Volume Change in the Amundsen Sea Embayment, West Antarctica. *IEEE Journal of Selected Topics in Applied Earth Observations and Remote Sensing, 7*(3), 863-871. doi:10.1109/JSTARS.2013.2264160

Zotikov, I. A., Zagorodnov, V. S., & Raikovsky, J. V. (1980). Core Drilling through the Ross Ice Shelf (Antarctica) Confirmed Basal Freezing. *Science, 207*(4438), 1463-1465. doi:10.1126/science.207.4438.1463

Zwally, H. J., Comiso, J. C., & Gordon, A. L. (1985). Antarctic offshore leads and polynyas and oceanographic effects. In S. S. Jacobs (Ed.), *Oceanology of the Antarctic Continental Shelf* (Vol. 43, pp. 203-226). Washington, D.C.: American Geophysical Union.

APPENDIX A. GPR TRACES ON THE SMIS

A.1. GPR TRACES COLLECTED WITHIN THE INNER GRID

The processed GPR profiles captured on the Southern McMurdo Ice shelf in the inner grid. The map of the traces below is for label reference purposes only. The northern ends of the lines (upper edge) are labelled 'J' followed by a number (e.g. J6). The southern end of the lines are named in a similar manner with either an 'A' or a 'D' depending on the length of the line. Note that the vertical and horizontal scales on the GPR profiles are not identical.

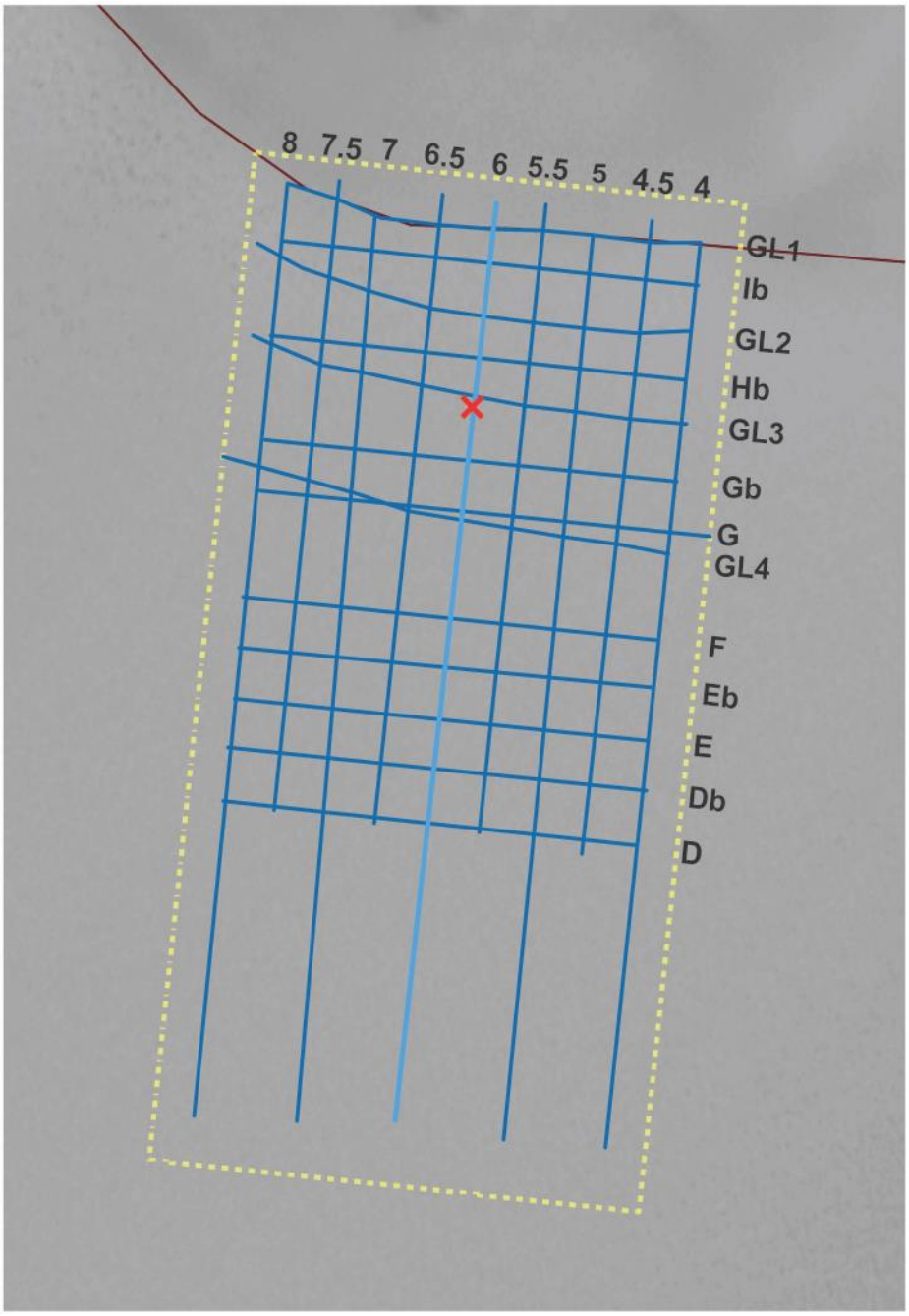

Line 4: J4-A4

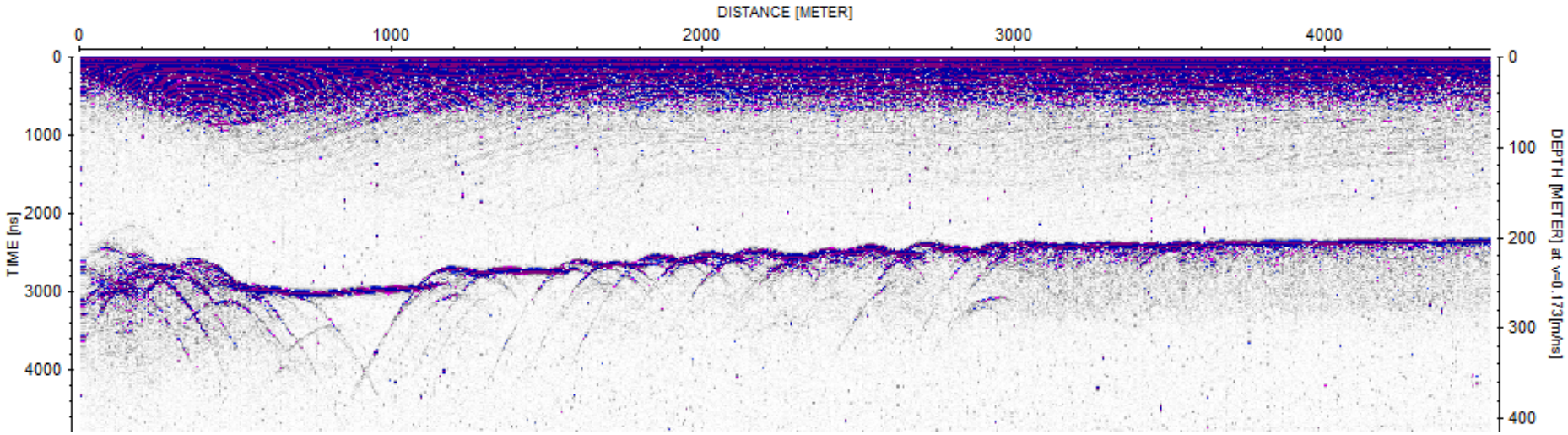

Line 4.5: J4.5-D4.5

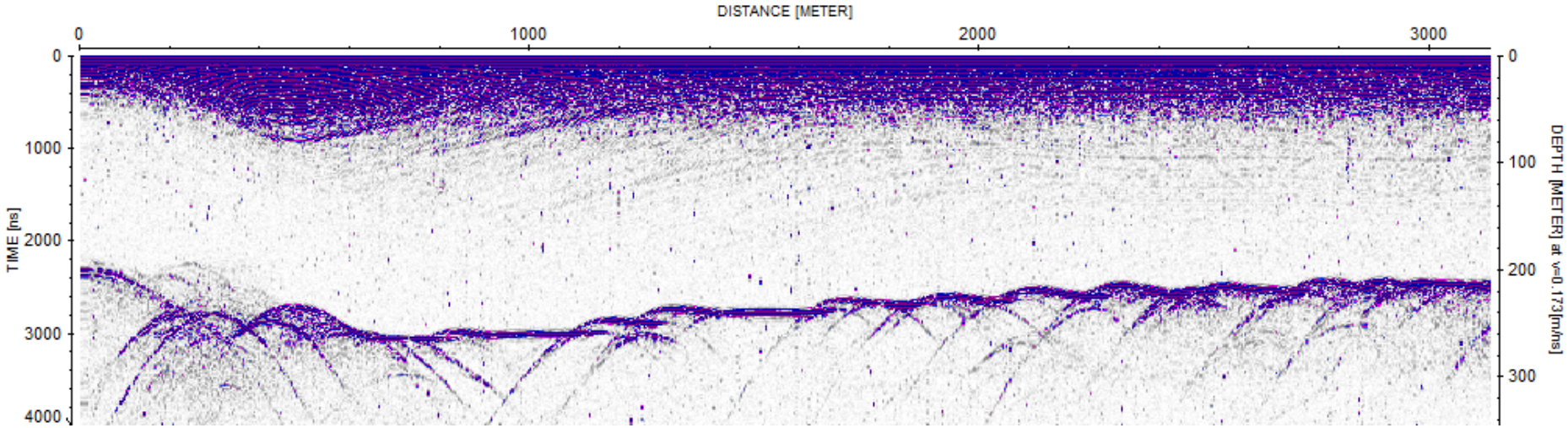

Line 5: J5-A5

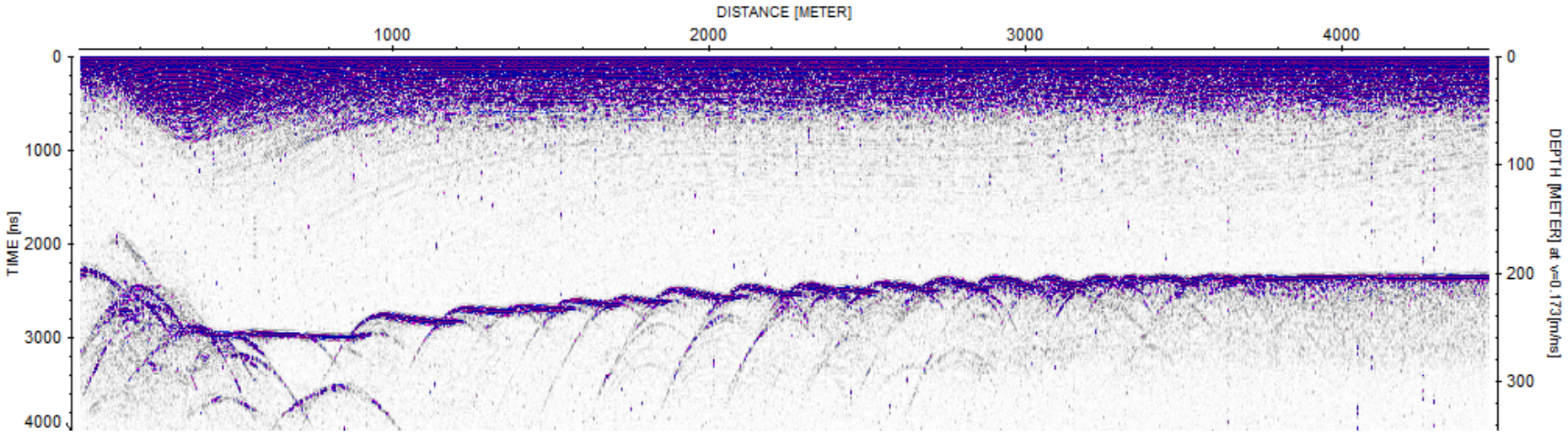

Line 5.5: J5.5-D5.5

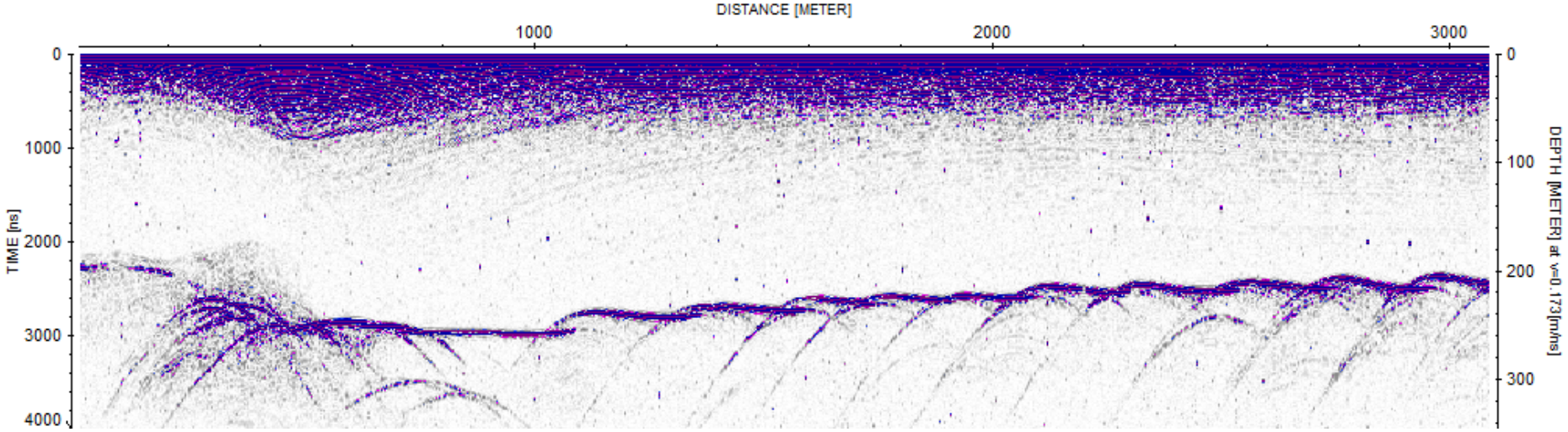

Line 6: J6-A6

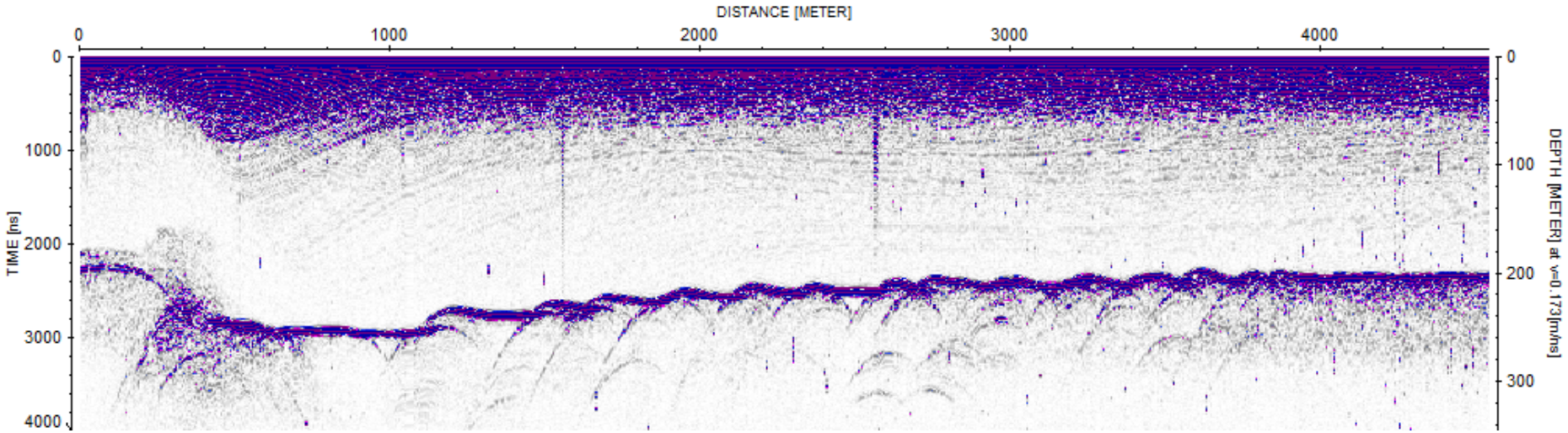

Line 6.5: J6.5-D6.5

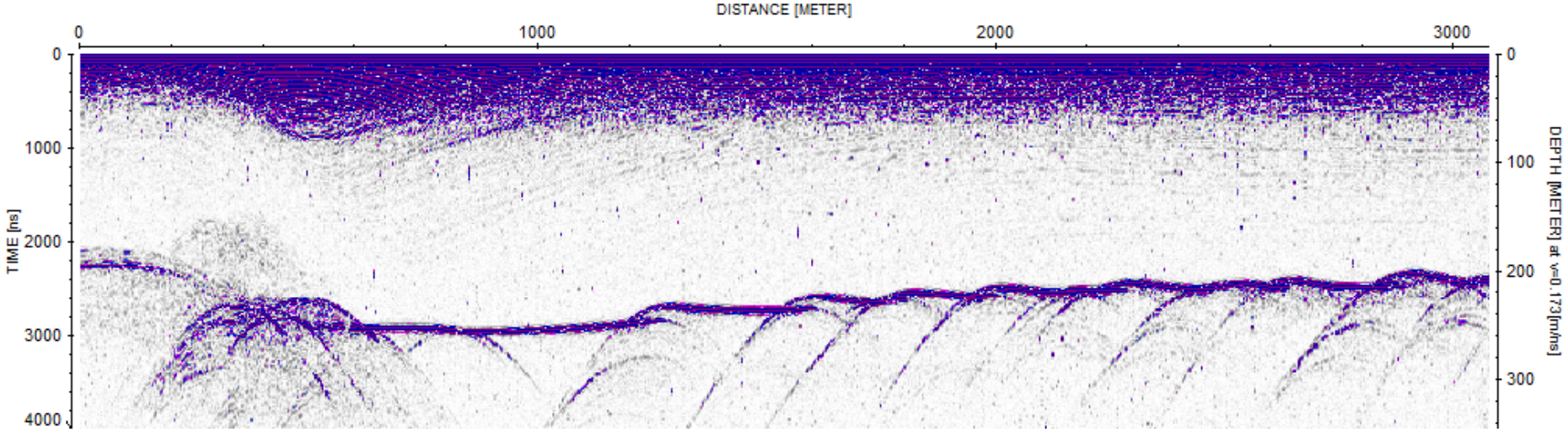

Line 7: J7-A7

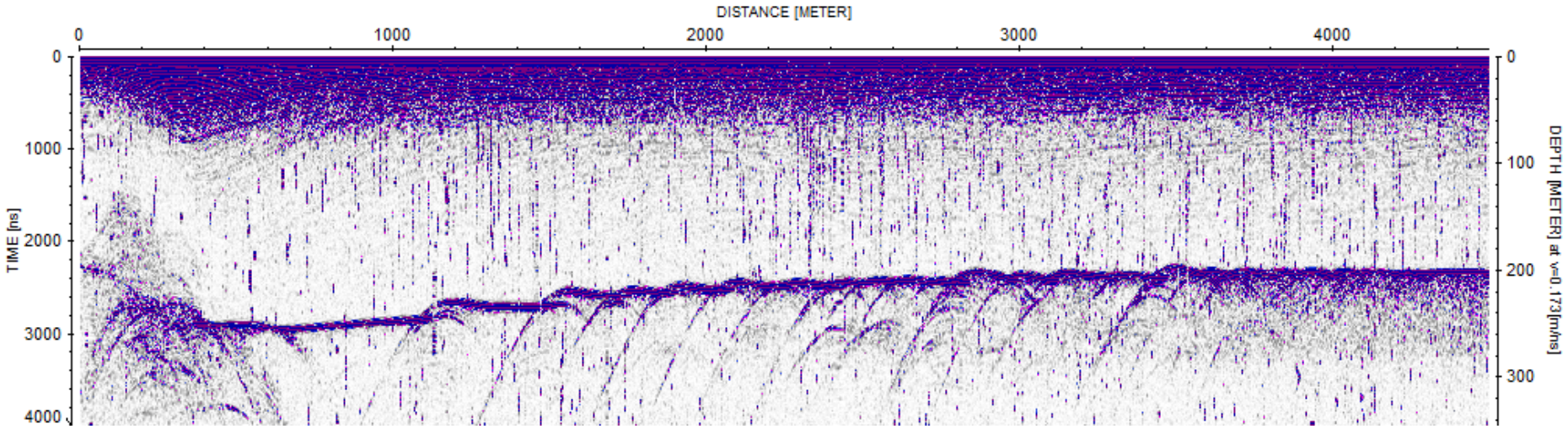

Line 7.5: J7.5-D7.5

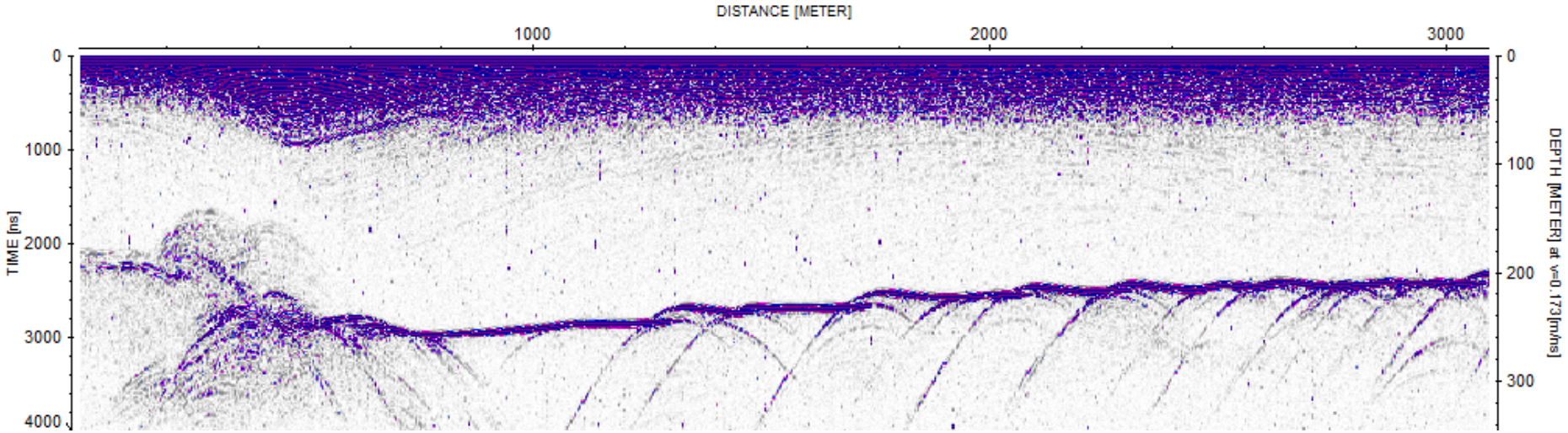

Line 8: J8-A8

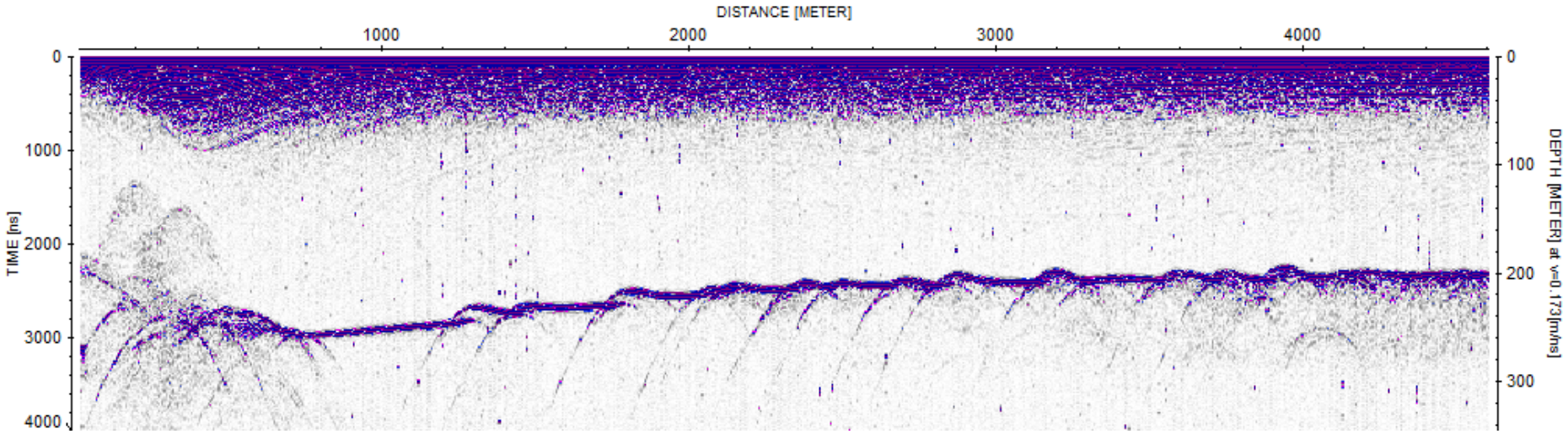

Line D: D8-D4

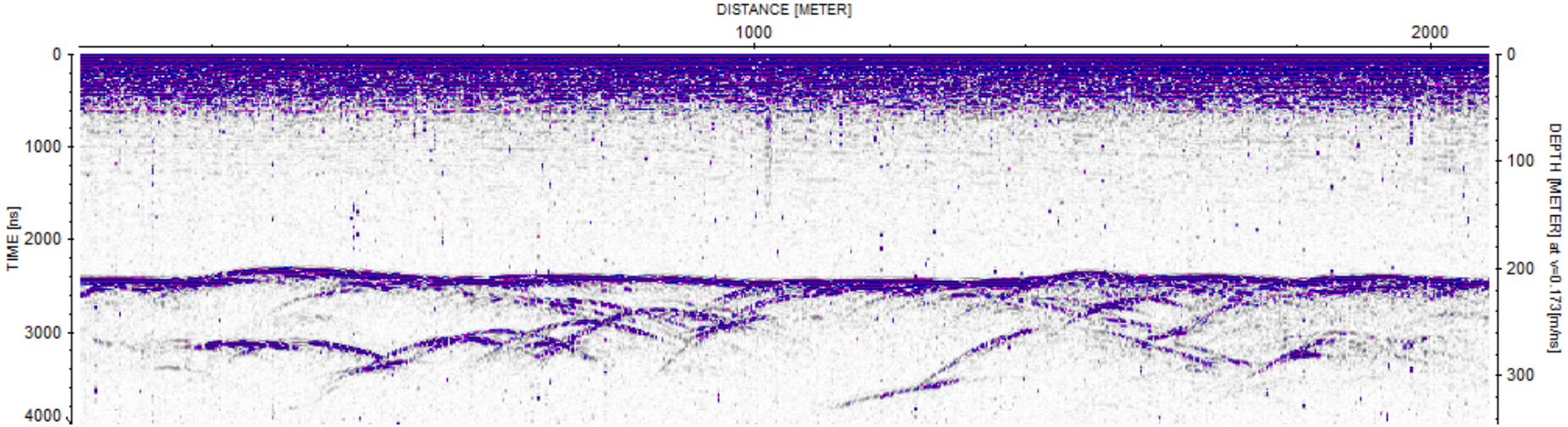

Line Db: Db8-Db4

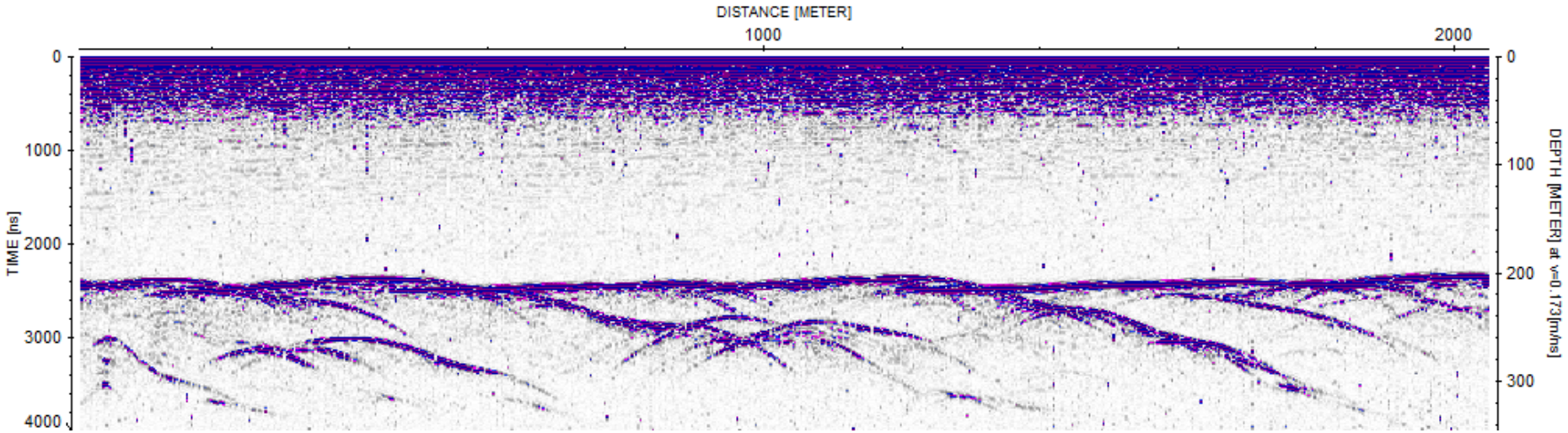

Line E: E8-E4

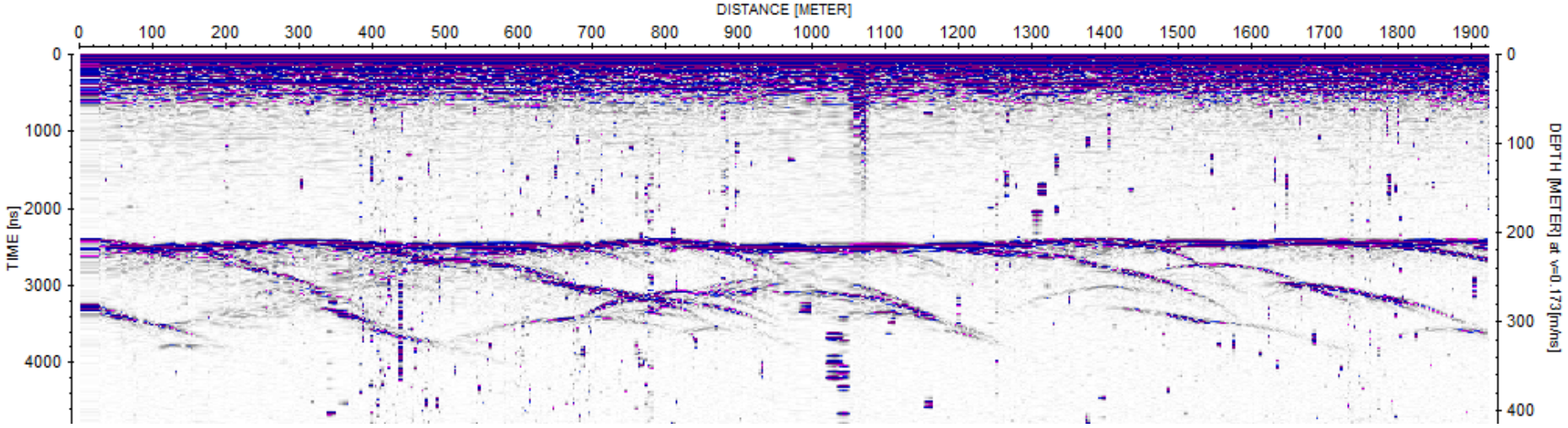

Line Eb: Eb8-Eb4

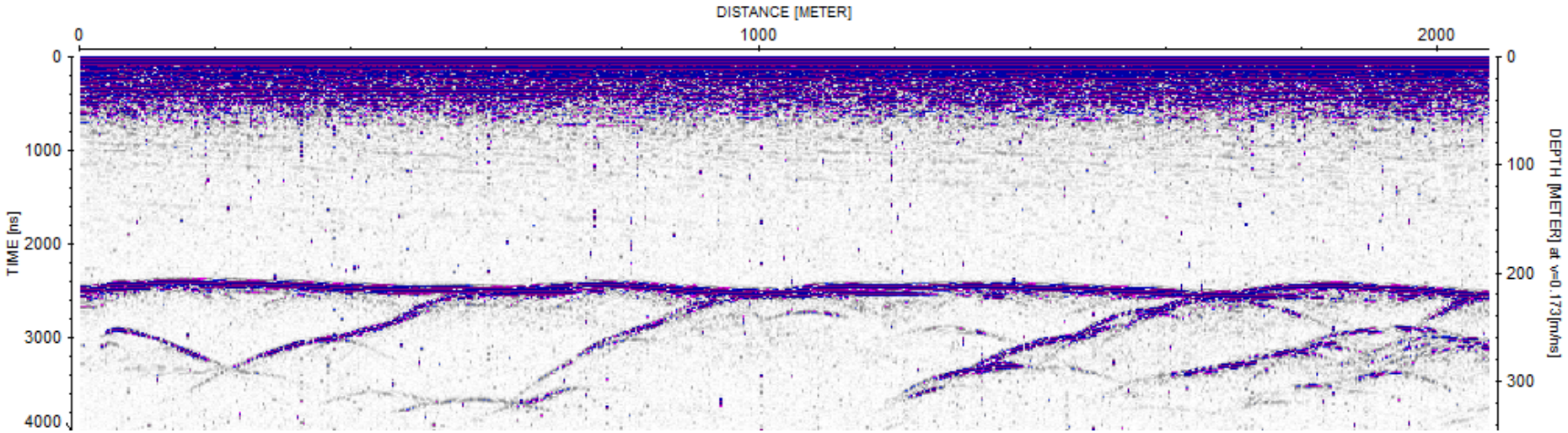

Line F: F8-F4

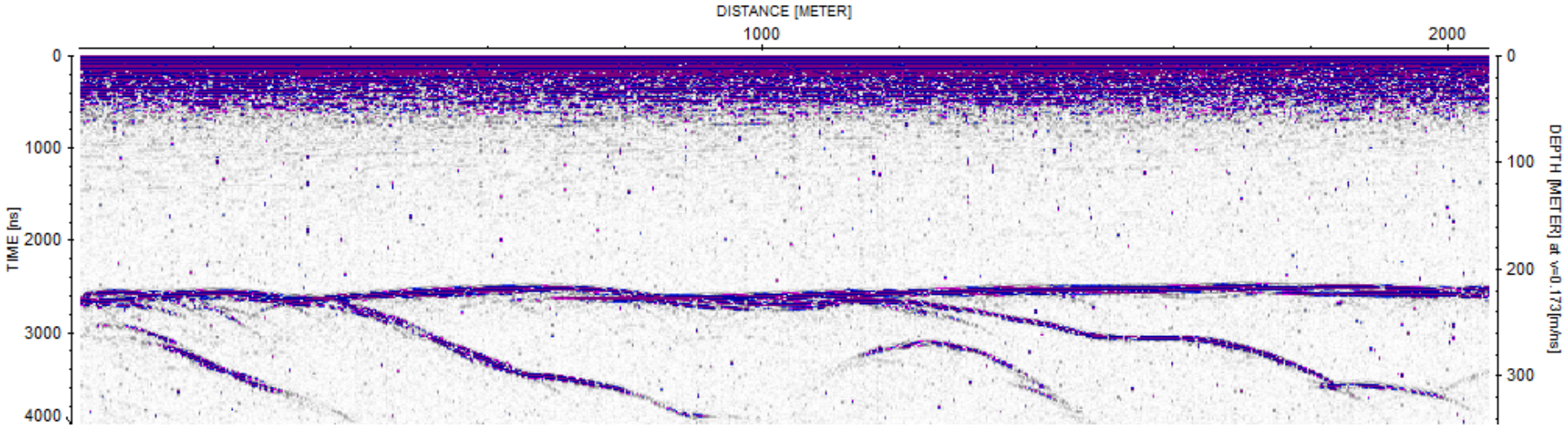

Grounding line 4: GL4_8-GL4_4

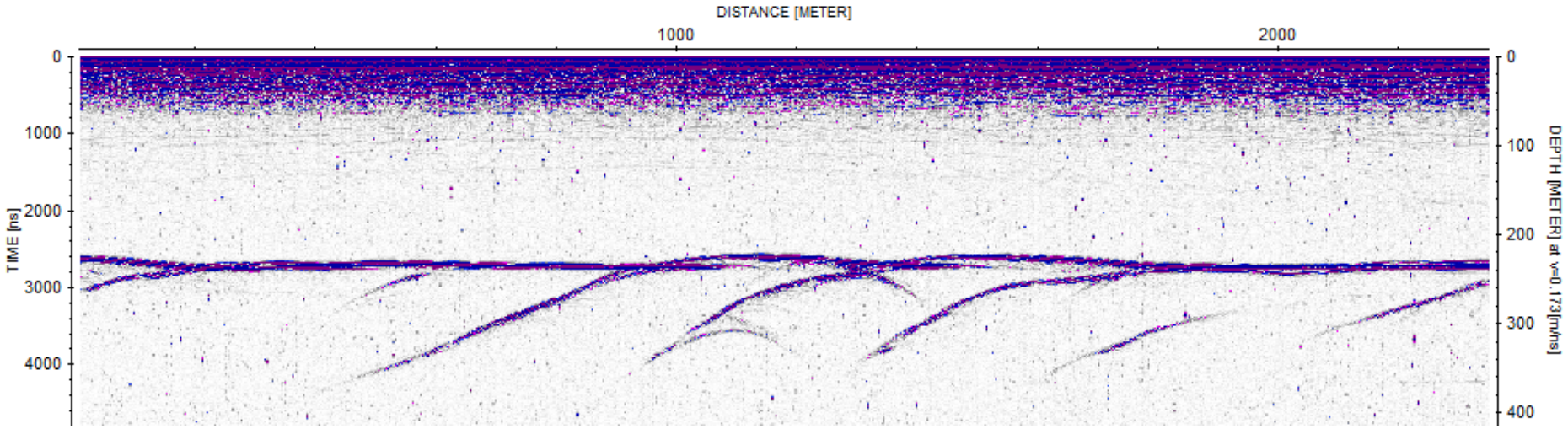

Line G: G8_G6

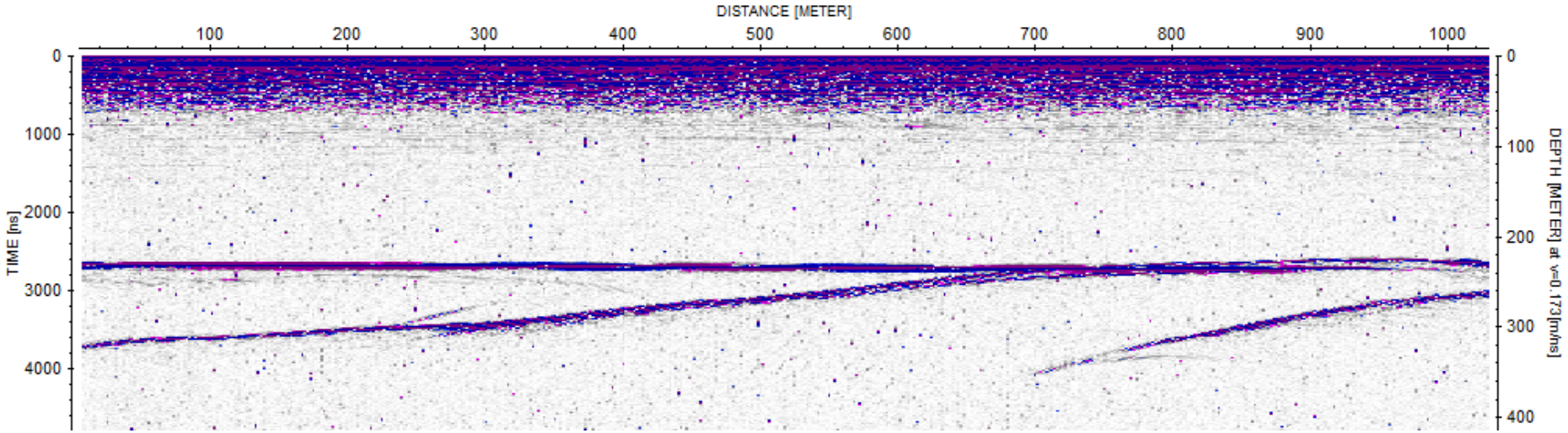

G6_G4

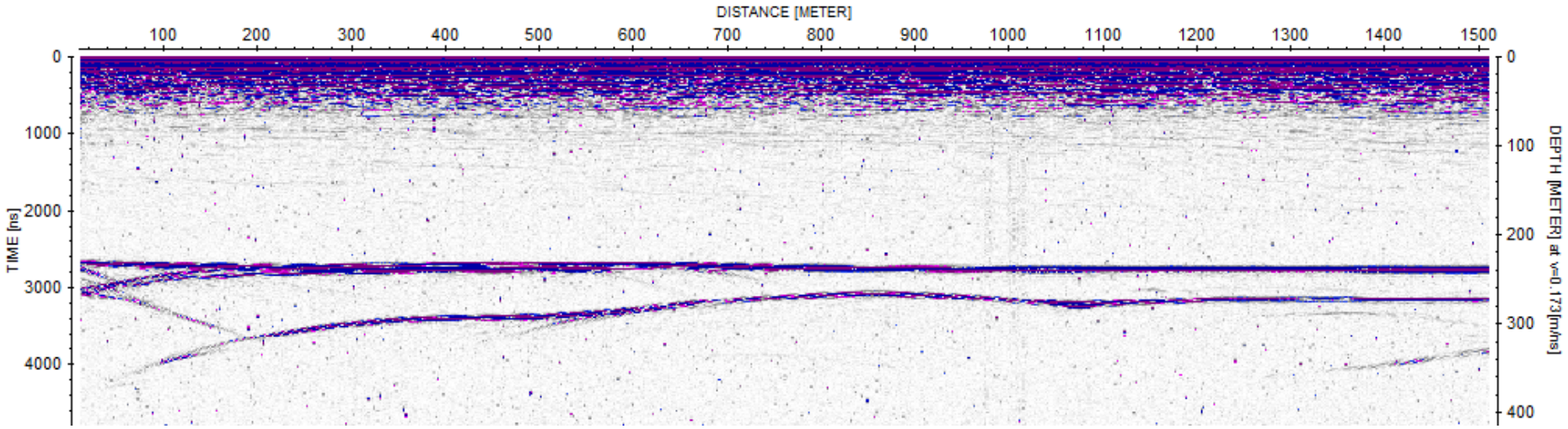

Line Gb: Gb8-Gb4

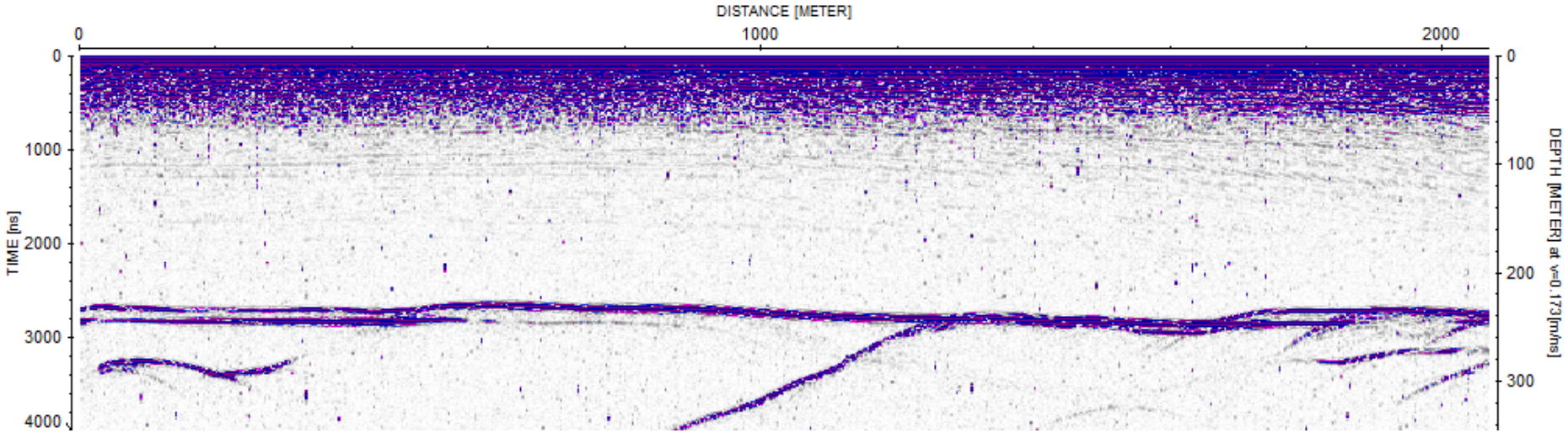

Grounding line 3: GL3_8-GL3_4

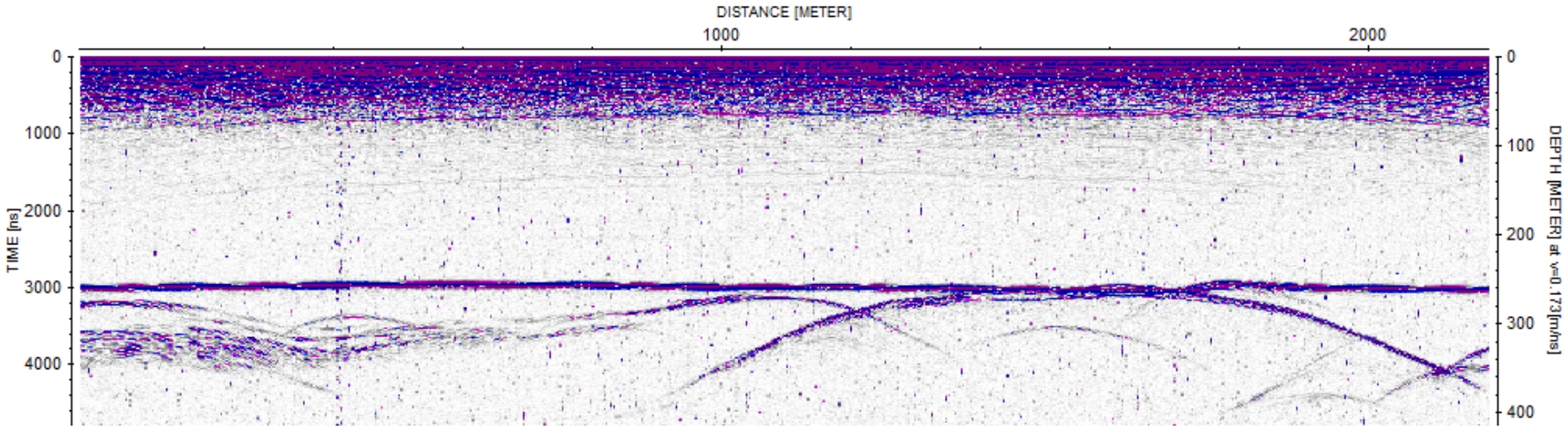

Line Hb: Hb8-Hb4

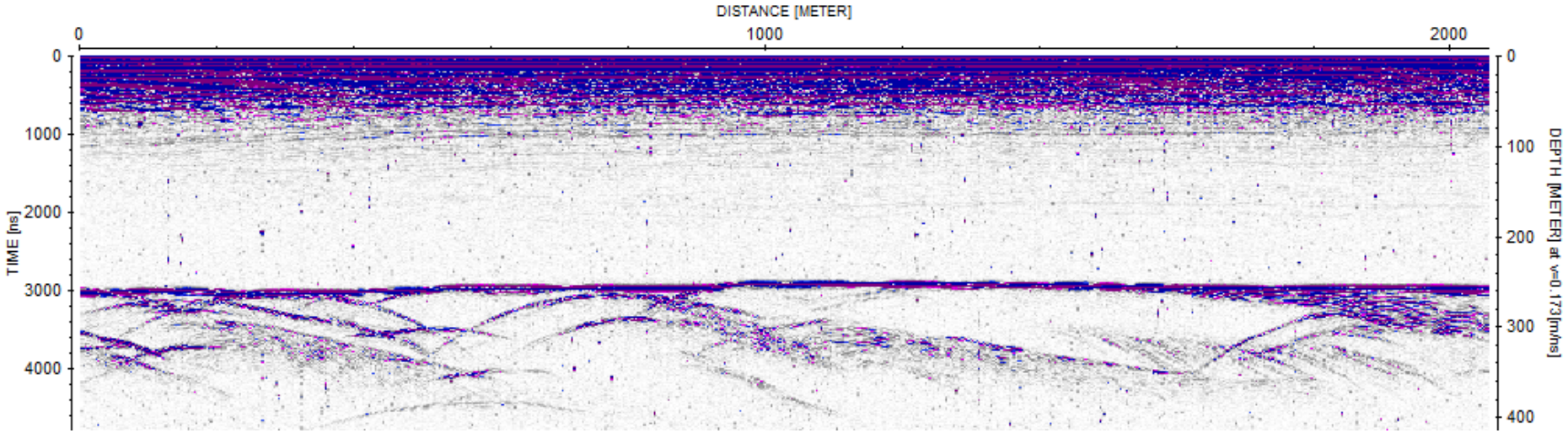

Grounding line 2: GL2_8-GL2_4

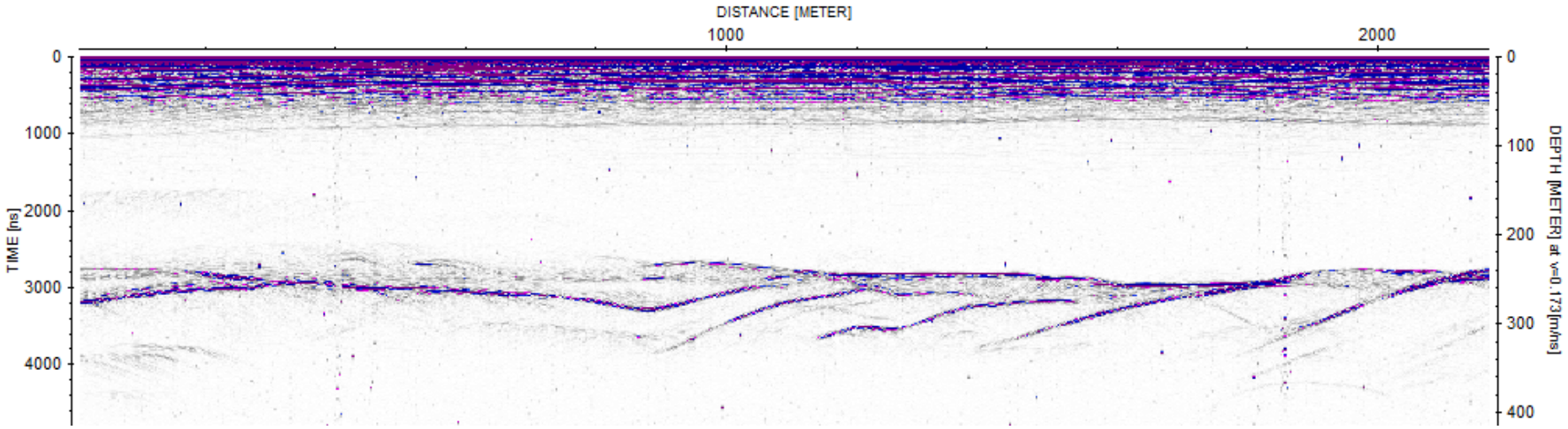

Line Ib: Ib8-Ib4

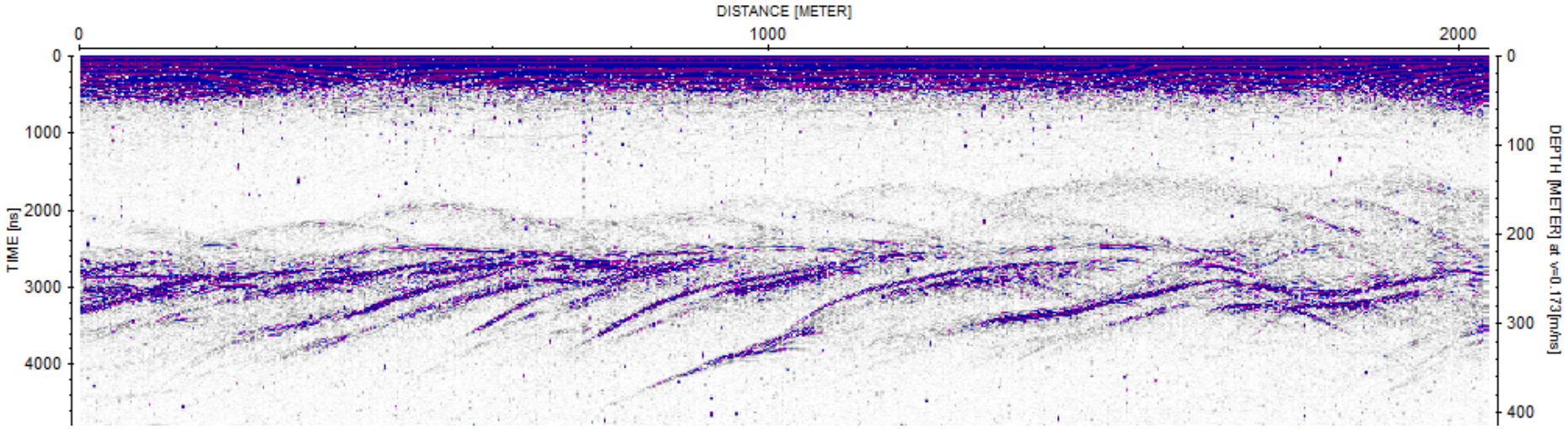

Grounding line 1: GL1_8-GL1_4

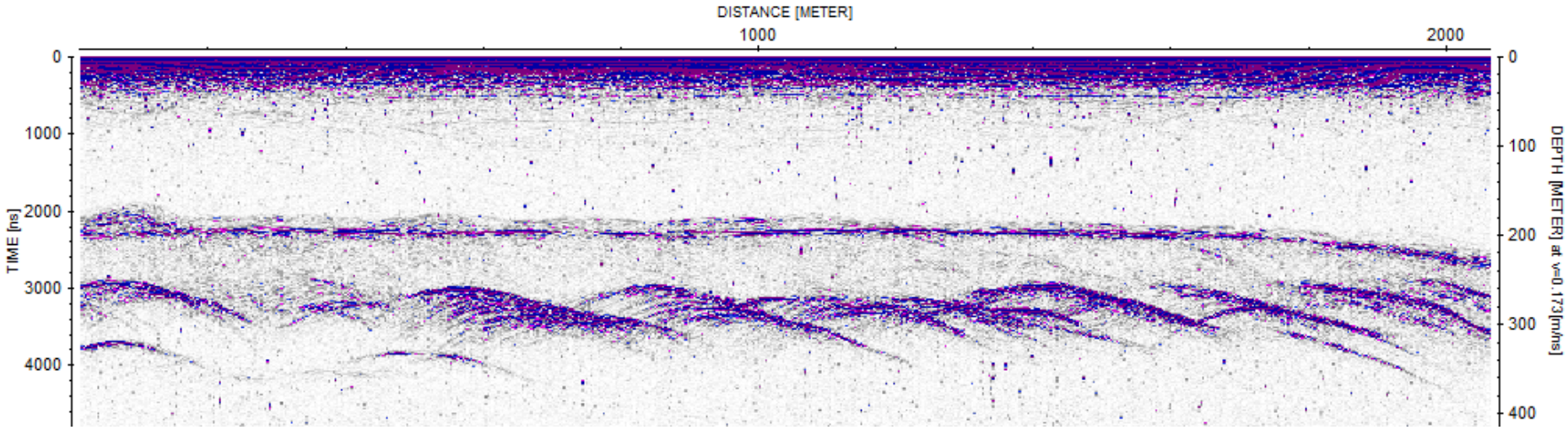

A.2. CROSS-OVER ANALYSIS OF ICE THICKNESS

The absolute difference in ice thickness (m) of GPR profiles at crossing points. Gaps represent locations where, despite their appearance, GPR traces do not cross. This is either often due to equipment failure, which required multiple sections of a single line to be 'stitched' together, or where lines were not physically intersected with the skidoo.

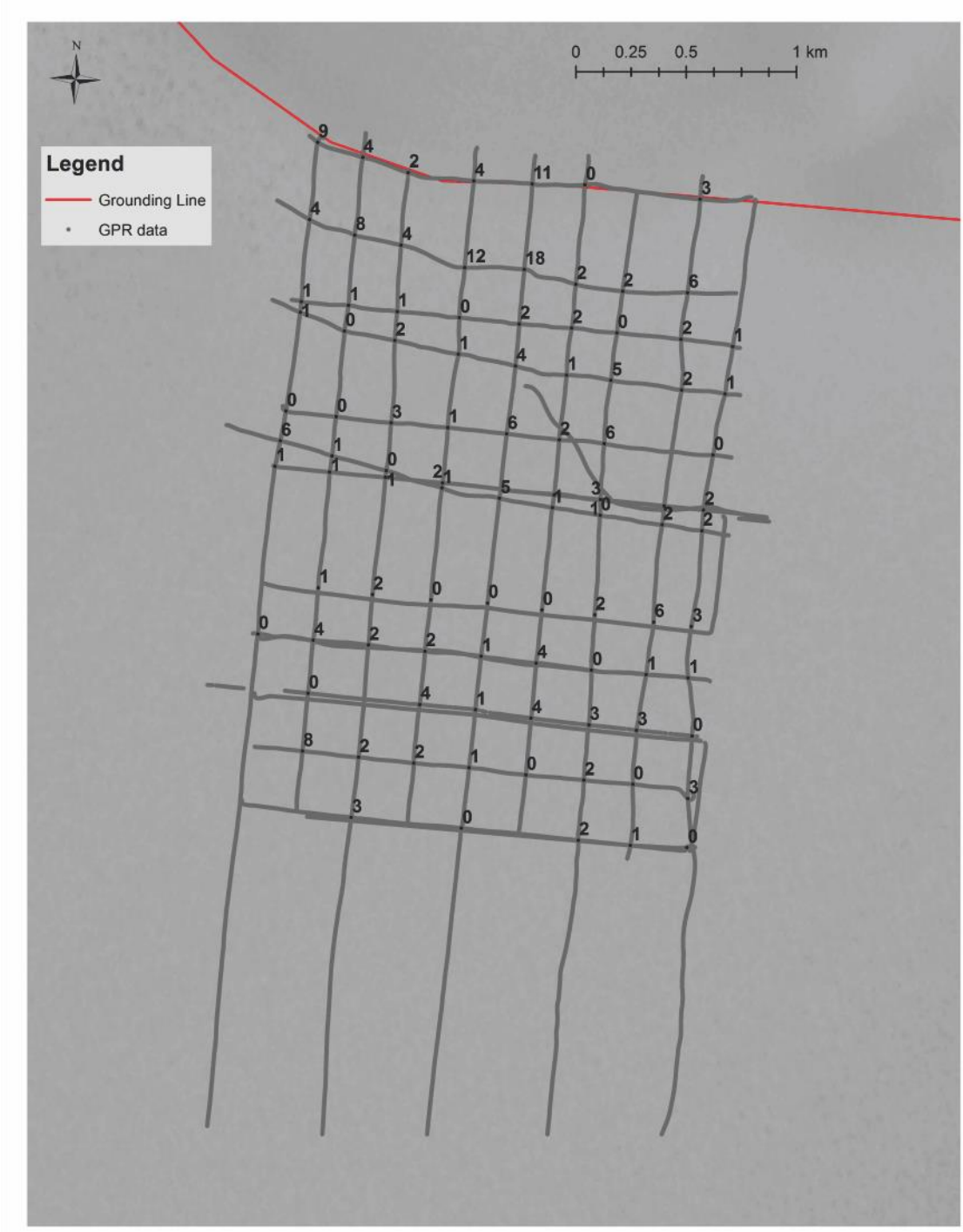

APPENDIX B. APRES ON THE RIS

B.1. ACQUISITION PARAMETERS OF APRES ON THE RIS.

The acquisition parameters, additional notes and radar profiles of the 21 ApRES sites on the RIS. The map below is for site name reference only.

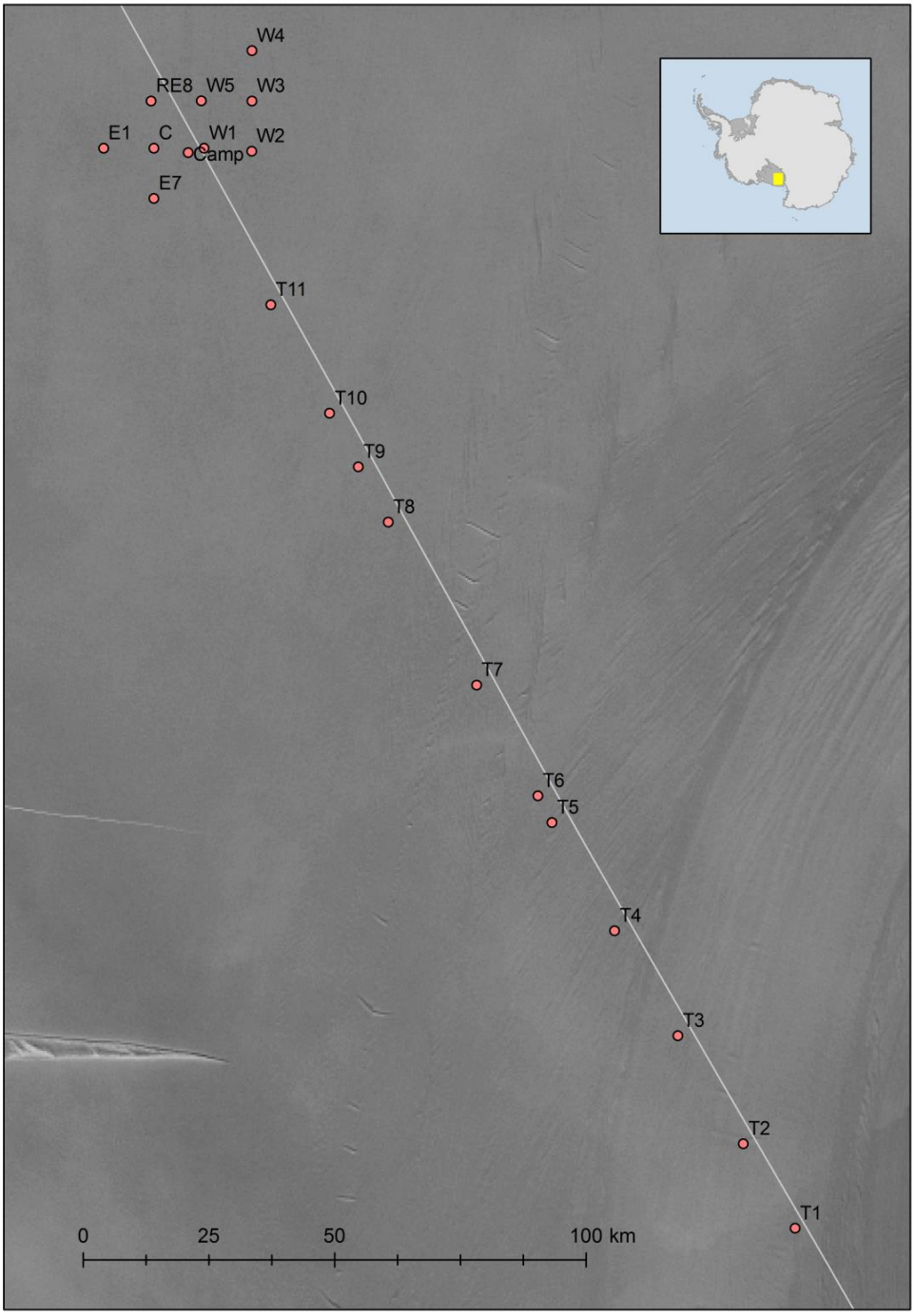

Site	Lat/Long (WGS84)	Attenuation (dB)	Gain (dB)	Number of chirps	Marine ice? (Y/N)	Notes	Radar profile
T1	-8.5867/ 169.8297	31	-6	20	**N**	Badly clipped[1], neglected from strain calculations	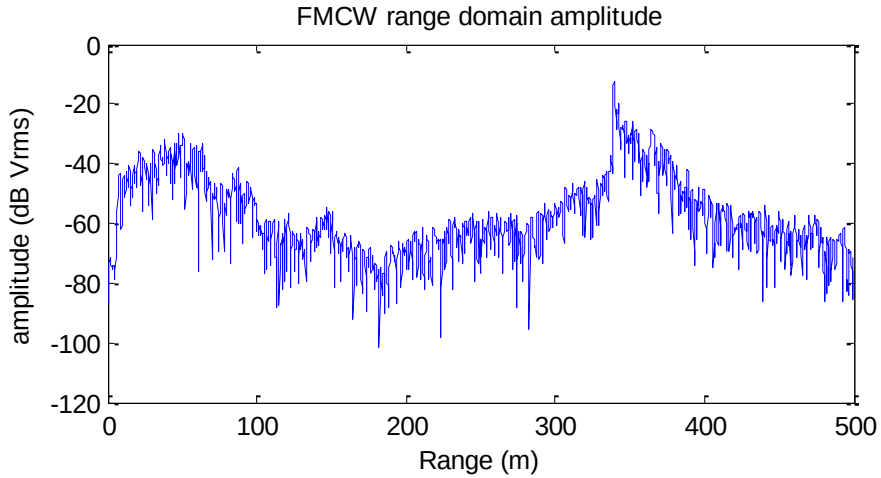
T2	-8.7539/ 170.1633	31	-6	20	**N**	Badly clipped, neglected from strain calculations	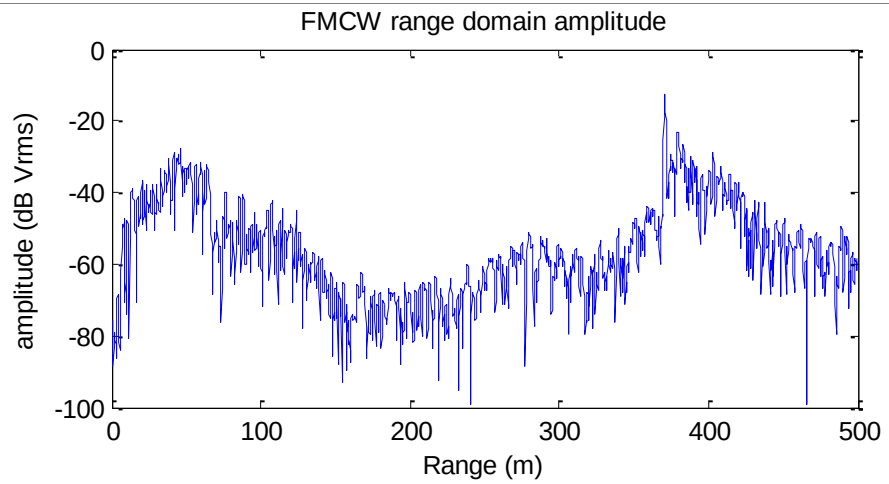

T3	-8.9671/ 170.6004	31	-6	20	**N**	Loose cable, badly clipped, neglected from strain	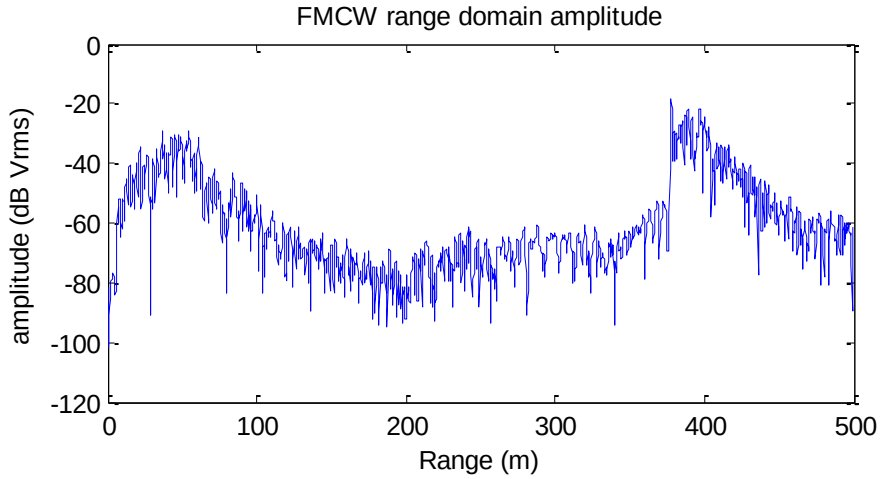
T4	-9.9671/ 171.0369	31	-6	20	**Y**		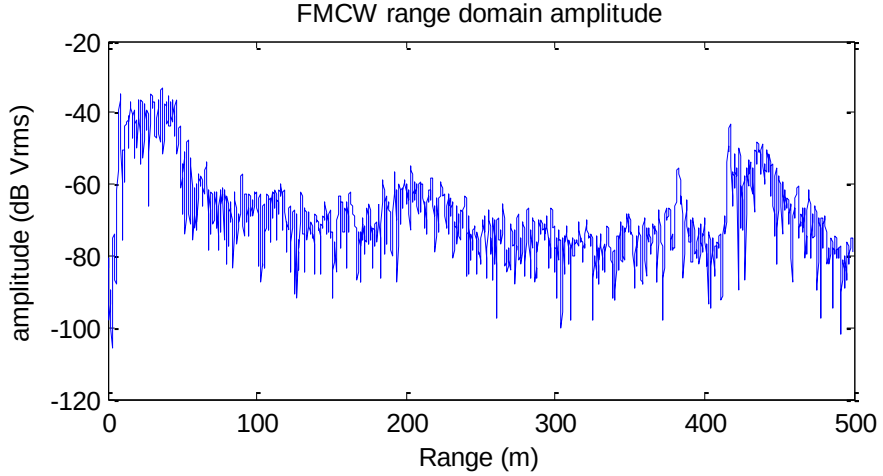

T5	-9.3847/ 171.4797	31/30	-6/0	20	**Y**	Strain fitting unable to match layers, neglected from strain	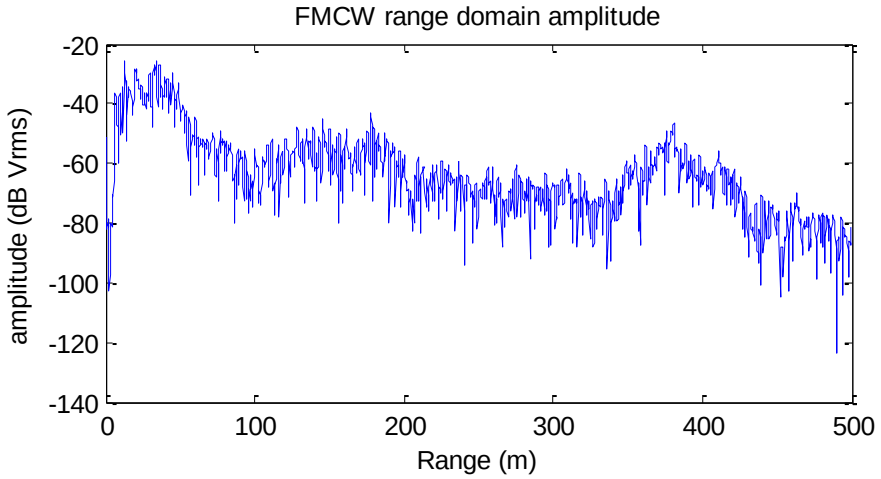
T6	-9.4364/ 171.5800	31	-6	20	**Y**		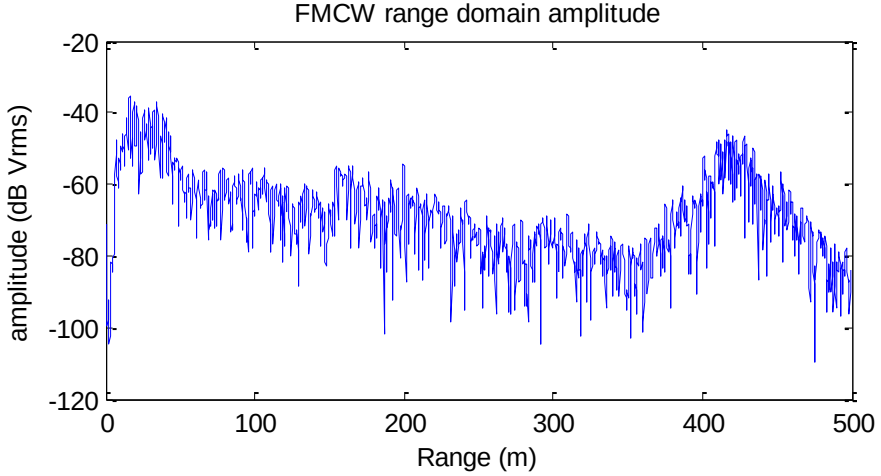

T7	-9.6513/ 172.0281	31	-6	20	**N**	Very strong, single peak reflector	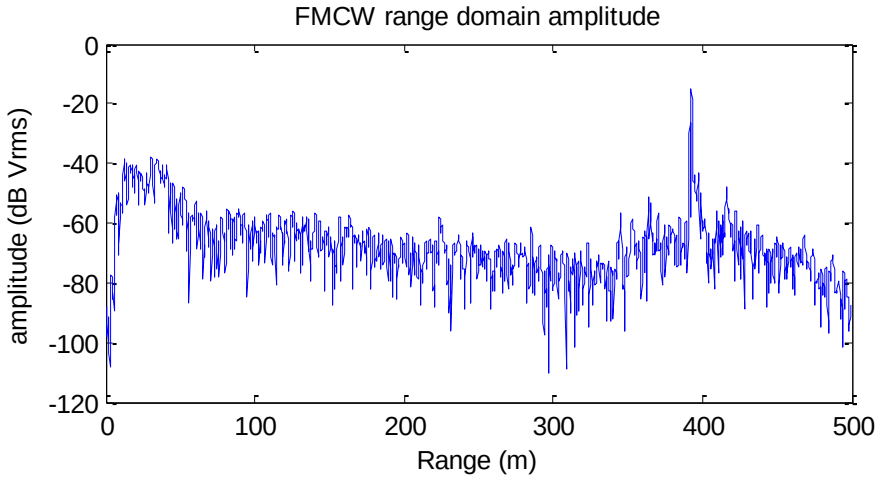
T8	-9.9660/ 172.7056	28	0	20	**N**		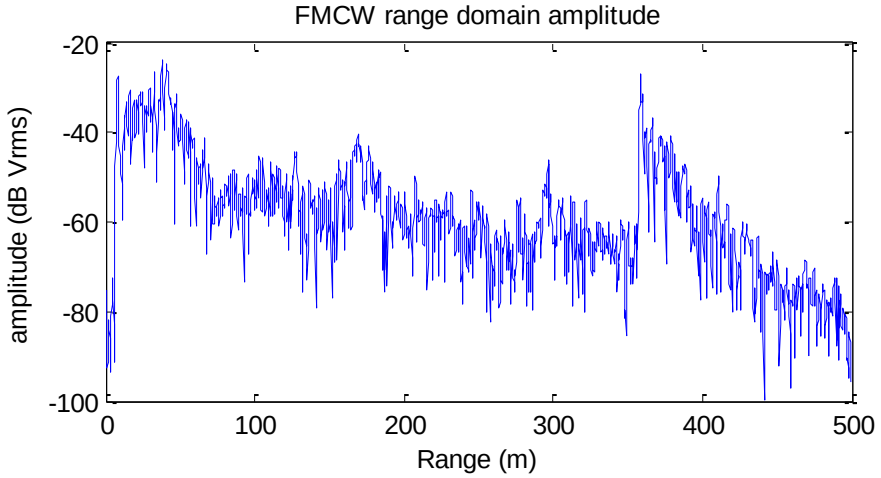

T9	-0.0726/ 172.9431	28	0	20	**N**	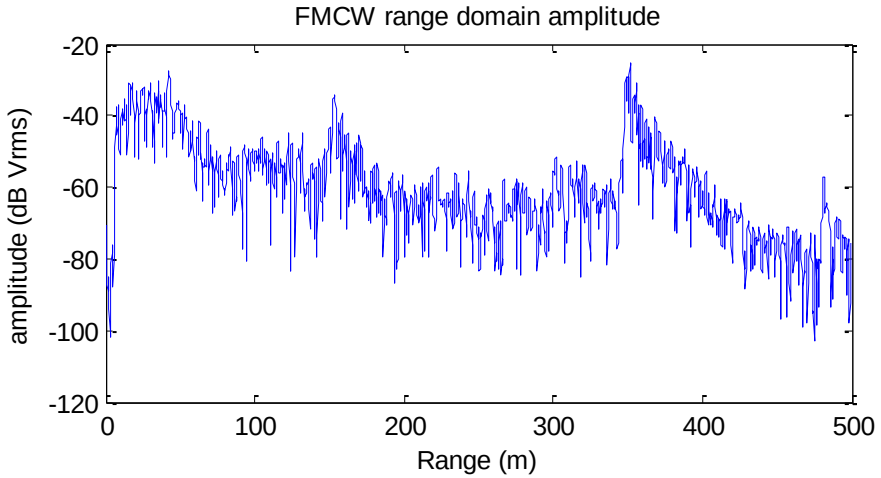
T10	-0.1754/ 173.1777	28	0	20	**Y**	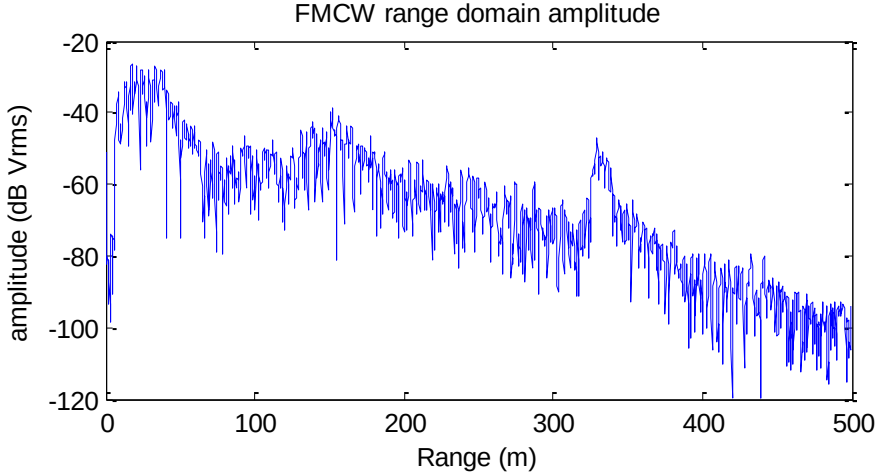

T11	-0.3835/ 173.6721	28	0	20	**Y**	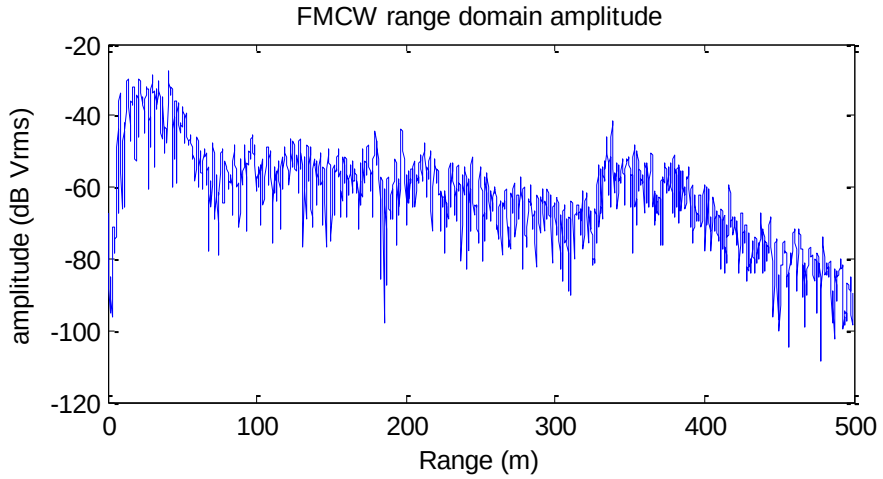
Camp	-0.6746/ 174.4044	28	0	20	**Y**	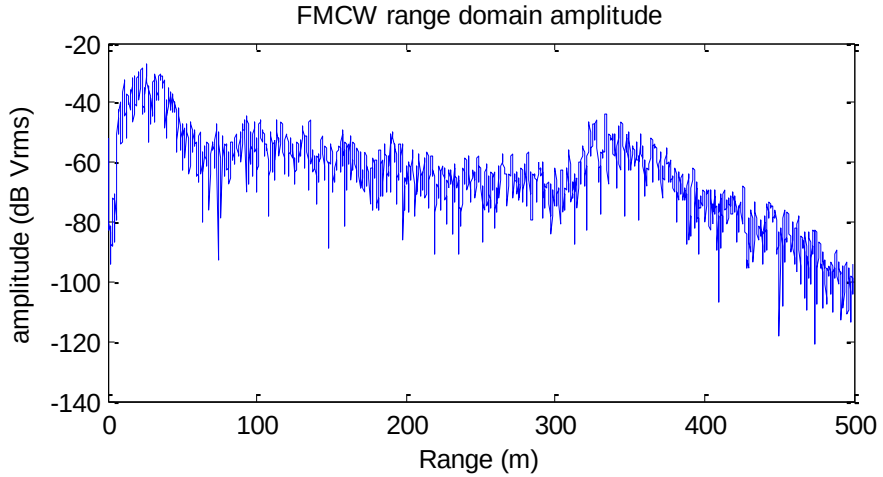

W1	-0.6796/ 174.2214	28	0	20	**Y**	Two peaks, second is nadir based on ice thickness at camp which is close by	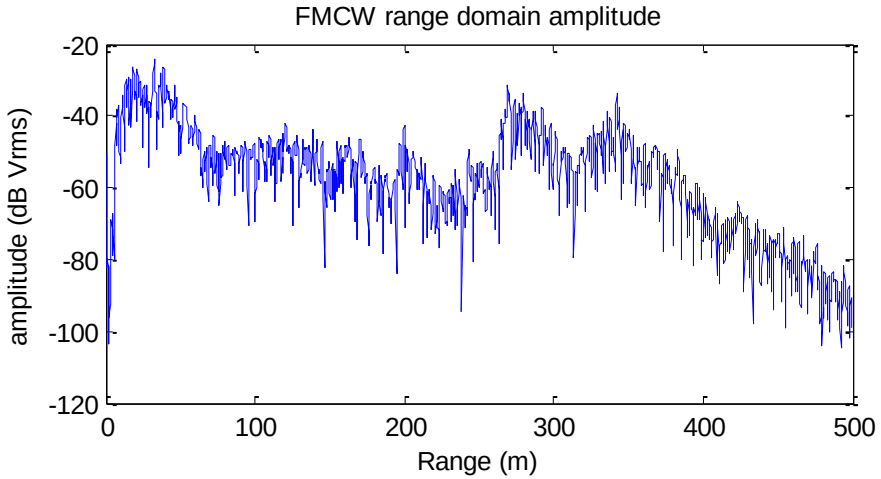
W2	-0.6649/ 173.6943	28	0	20	**Y**		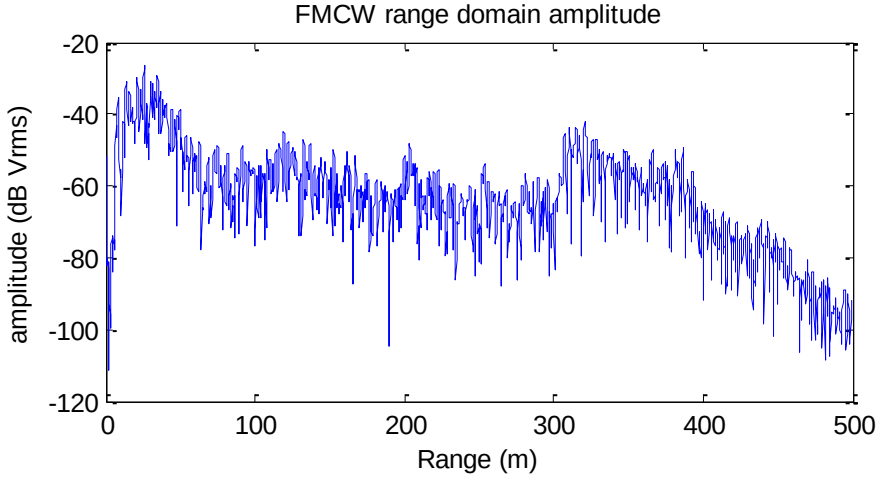

W3	-0.7557/ 173.6301	26	0	20	**Y**	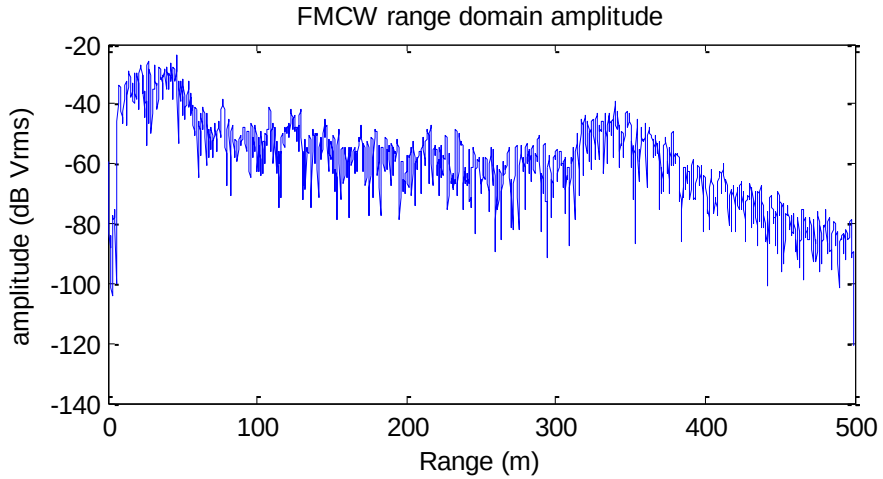
W4	-0.8466/ 173.5662	26	0	25	**Y**	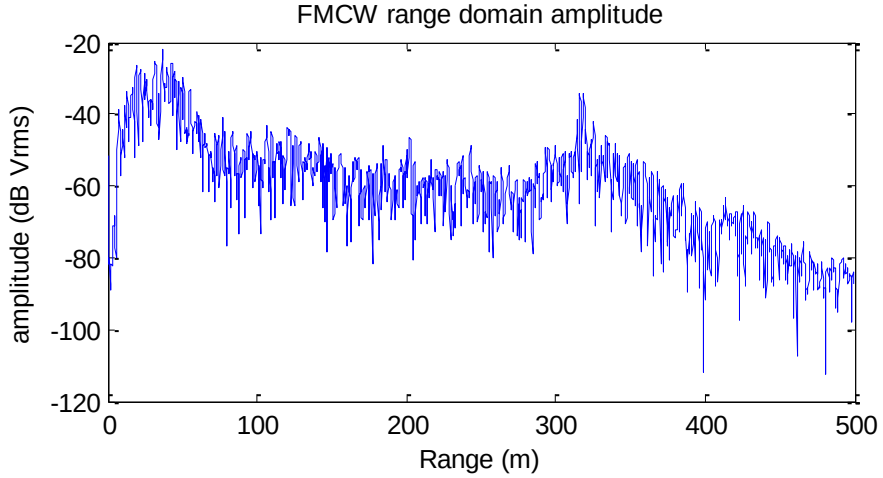

W5	-0.7657/ 174.1991	24	0	25	**Y**	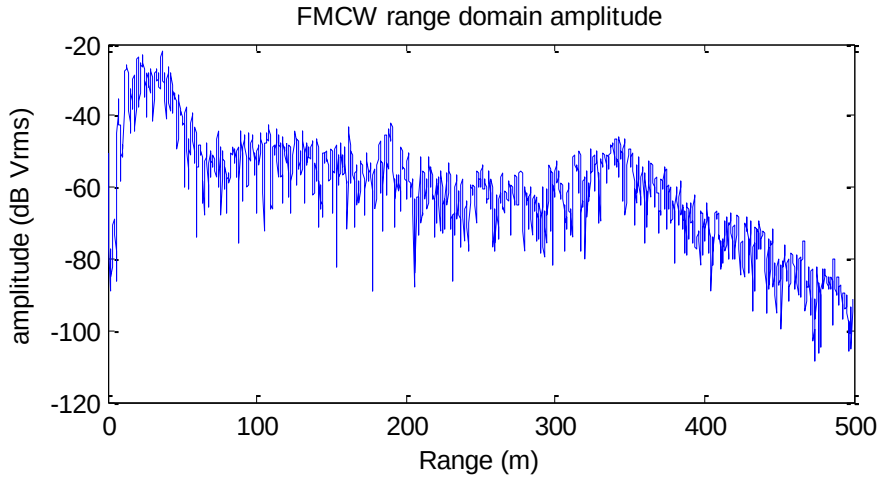
RE8	-0.7743/ 174.7657	26	0	25	**Y**	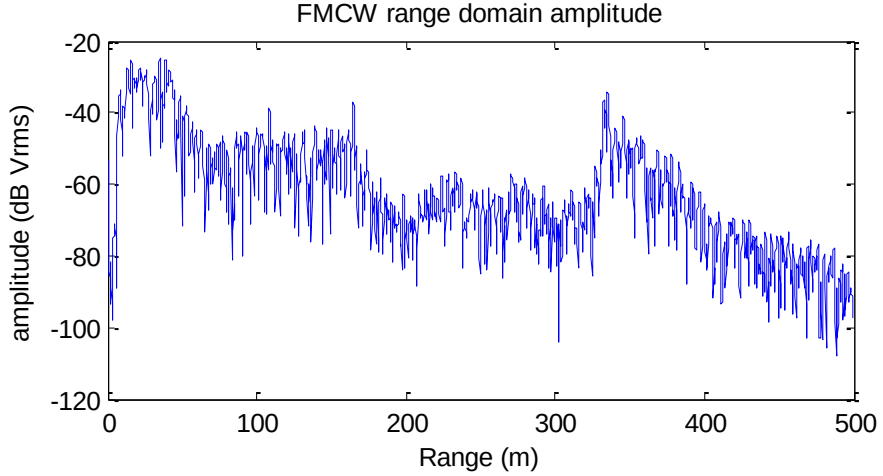

C	-0.6883/ 174.7837	25	0	30	**Y**	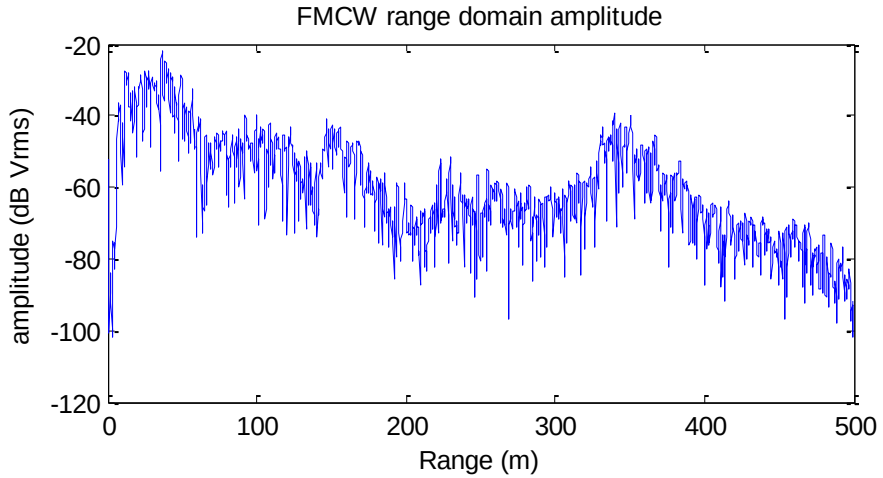
E1	-0.6962/ 175.7837	25	0	20	**Y**	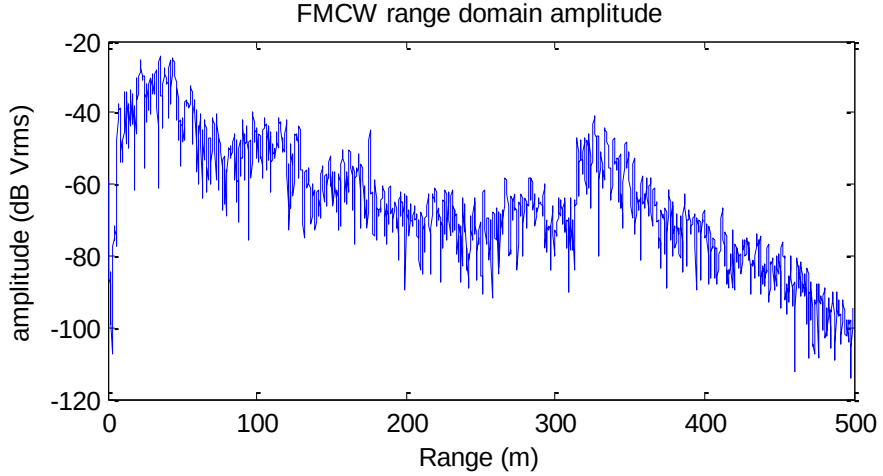

E7	-0.5972/ 174.8345	26	0	20	**Y**	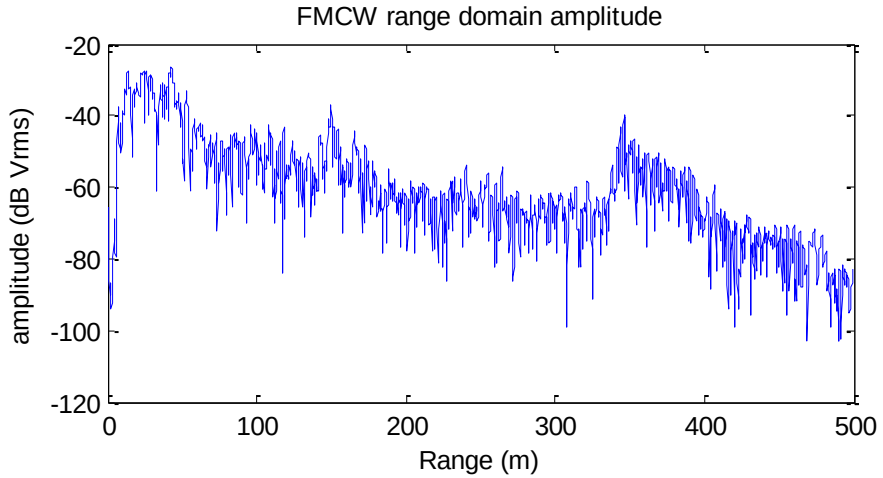

[1] *clipping occurs when the voltage of the reflected signal exceeds the sensitivity of the receiving antenna. Signal clipping can be revealed by plotting voltage against time. Here, T1 is used as an example of a site which is badly clipped in the first 0.6s and at other subsequent times. Other sites that display clipping have a similar plot.*

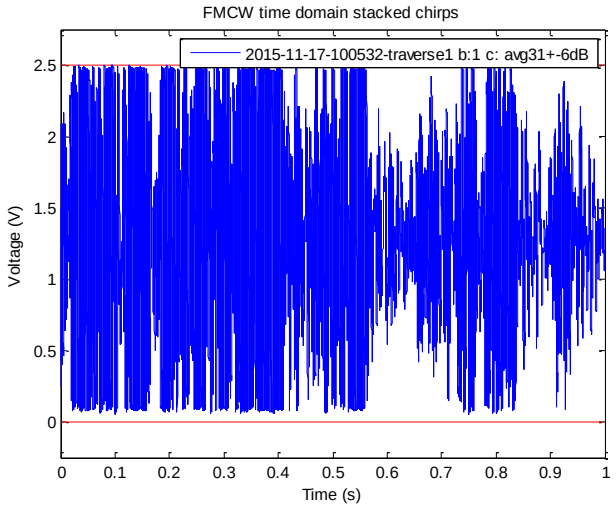

B.2. REPEAT RADAR PROFILES AND STRAIN/BASAL MELT CALCULATION (WHERE APPLICABLE)

The radar profiles and the results from the vertical strain and basal melt (for sites denoted with a *) calculations. The initial (blue line) and repeat (red line) measurements are plotted. Strain is calculated by measuring the changing thickness between internal layers and applying a linear fit. The difference between the range of the bed at different time is dependent on the strain and basal melt/freezing. Note that ice thickness has not been corrected for firn.

Site	Bed search range (*m*)	Bulk matching range *(m)*	Bed depth initial/final *(m)*	dt *(days)*	Strain (error) *(x10^{-4}/year)*	Melt (error) *(m/yr)*	
T4	410-420	65-400	417.1546/ 416.8633	13.8084	-3.9342 (1.1252)		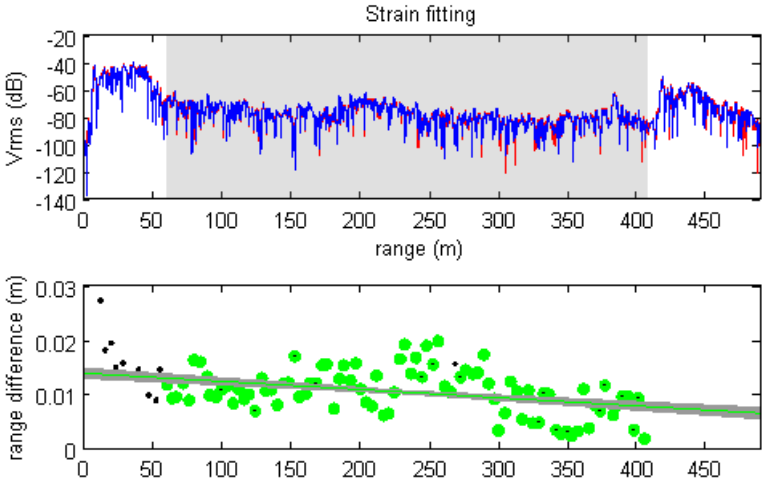

T6	410-420	65-400	416.0370/ 415.9457	12.7039	0.4202 (3.9008)		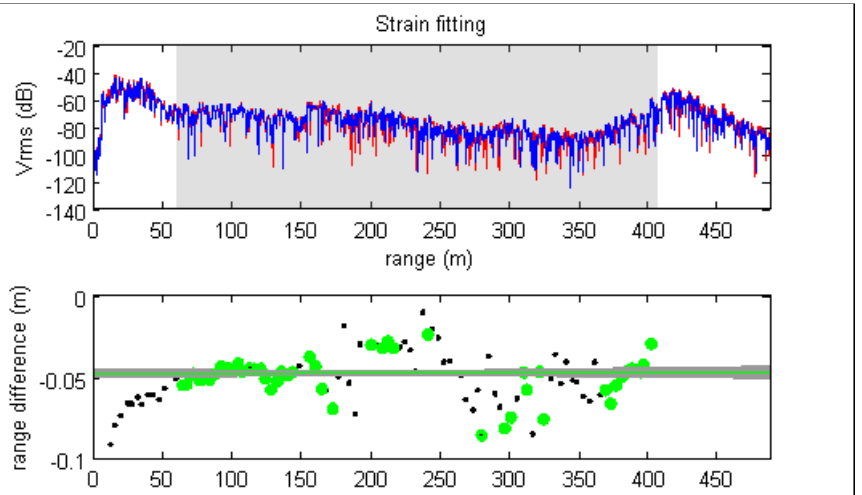
T7*	380-400	65-380	392.4436/ 392.7200	12.5465	-5.8665 (0.9484)	-0.0528 0.0186	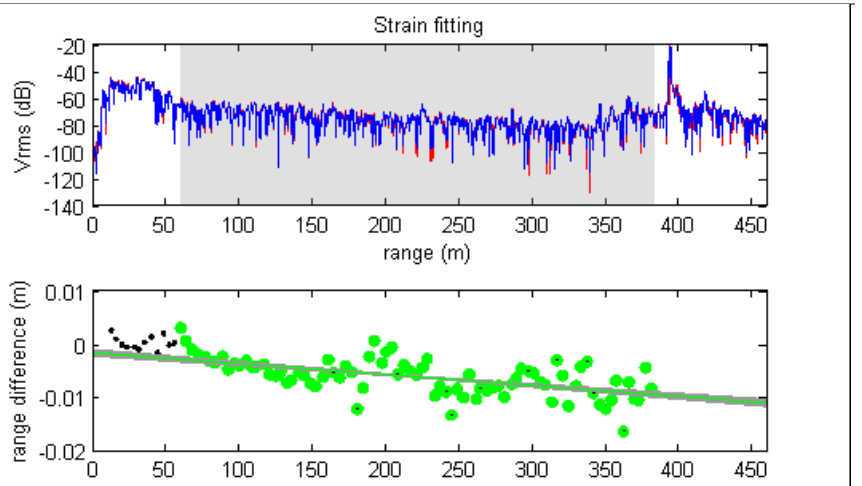

T8*	350-370	65-350	358.6843/ 358.6774	11.1953	-3.3826 (1.1254)	0.0059 (0.0197)	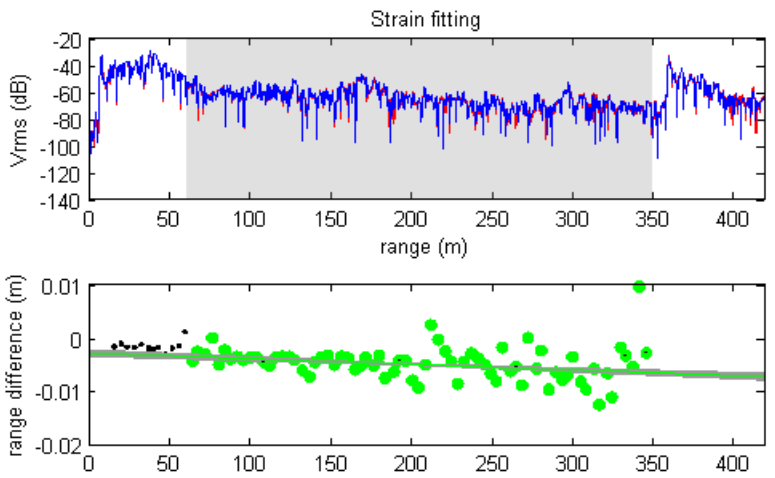
T9*	350-370	65-350	351.4884/ 351.4811	11.0968	-3.3490 (0.6700)	0.0529 (0.0115)	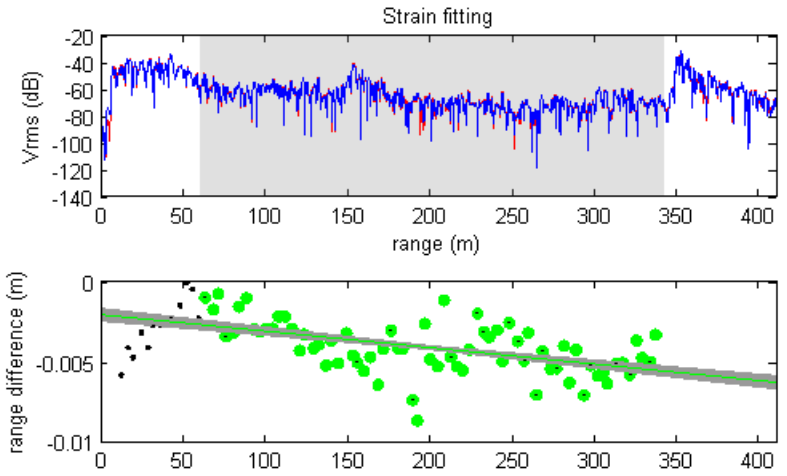

T10	320-350	65-320	329.5779/329.5690	10.9868	4.0601 (1.4762)	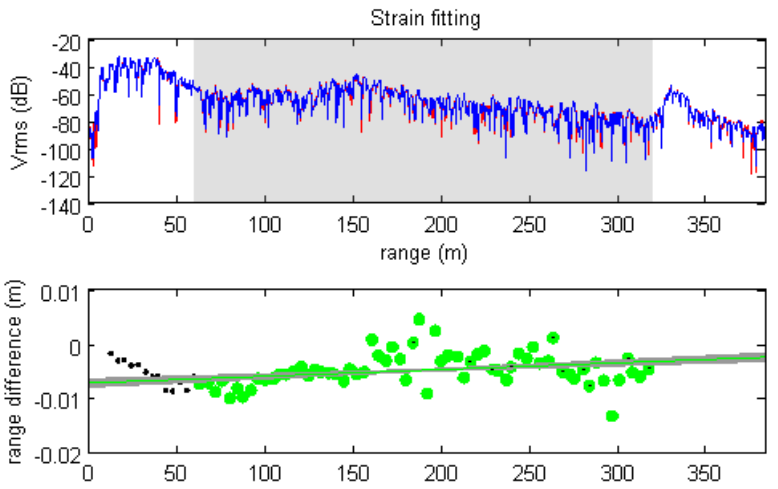
T11	320-350	65-320	338.1000/338.0899	10.7974	3.3852 (1.9133)	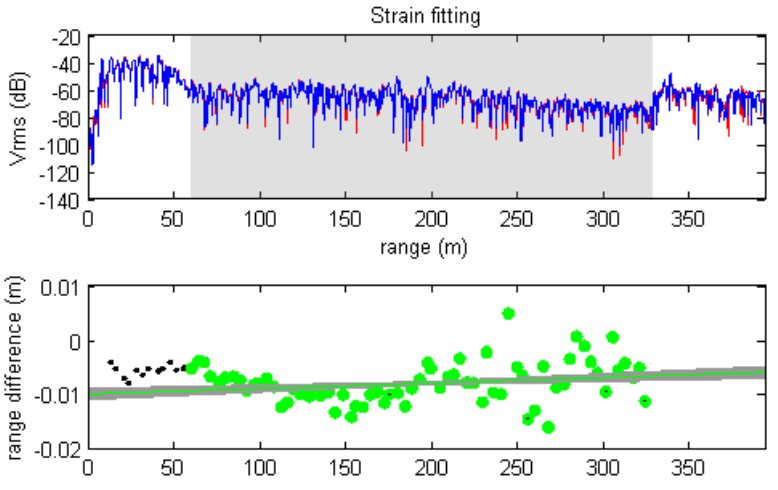

Camp	330-350	65-330	333.5822/ 333.8393	8.4243	5.0022 (2.3222)	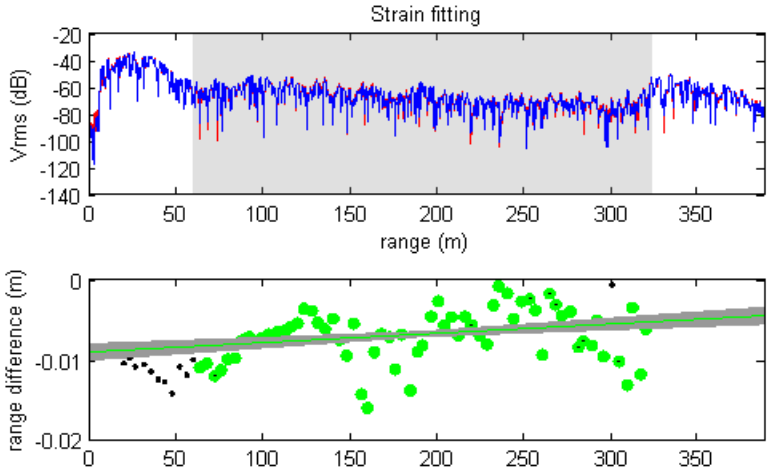
W1	330-350	65-330	341.9406/ 342.2168	7.7822	-5.5141 (8.6233)	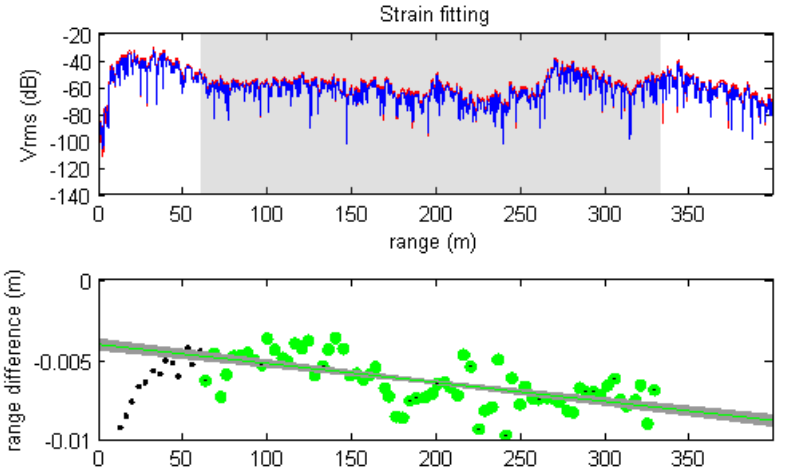

W2	310-330	65-310	320.6294/ 320.6226	7.7295	-4.8797 (3.8981)	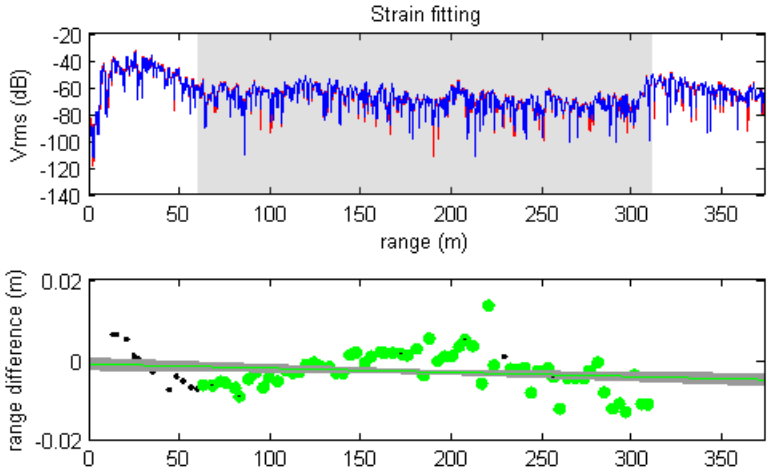
W3	330-350	65-330	339.4418/ 339.4387	5.8315	0.5542 (1.6634)	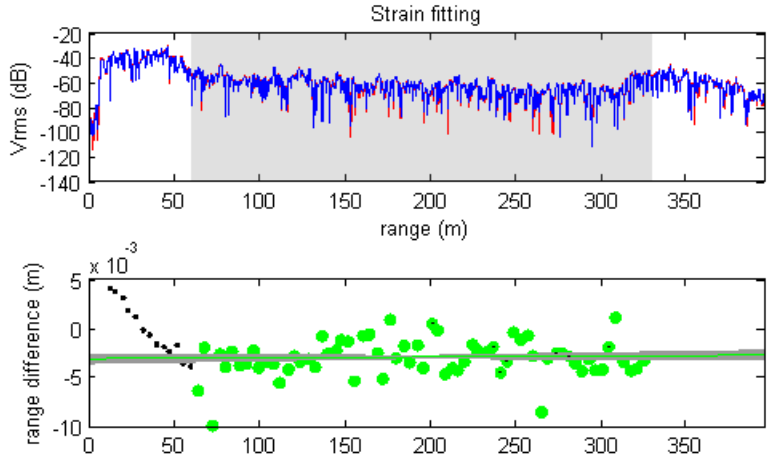

W4	310-320	65-310	3162173/316.2164	5.8216	-13 (1)	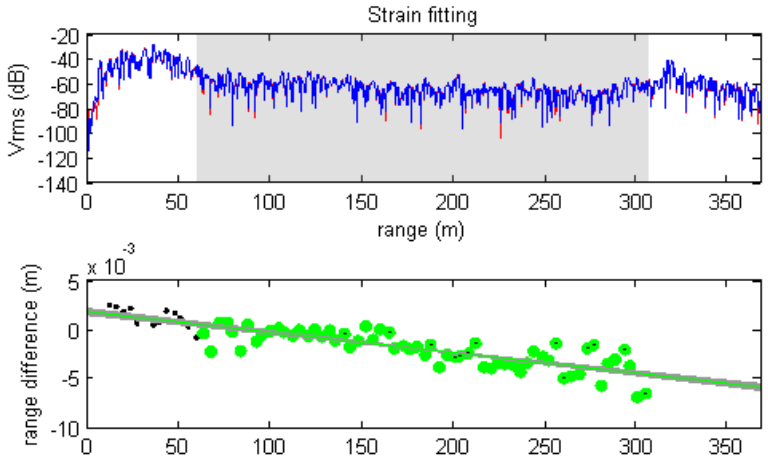
W5	330-350	65-330	342.9639/342.9777	5.8015	-17 (2)	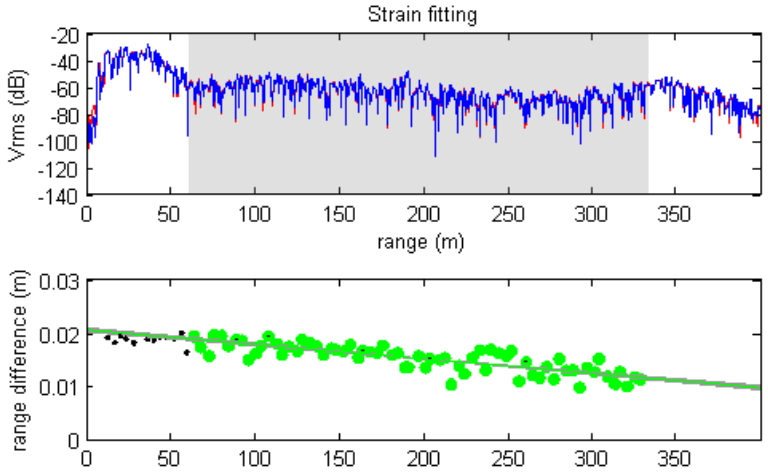

RE8	330-350	65-330	335.0319/ 335.0334	5.7699	-9.0259 (1.1028)	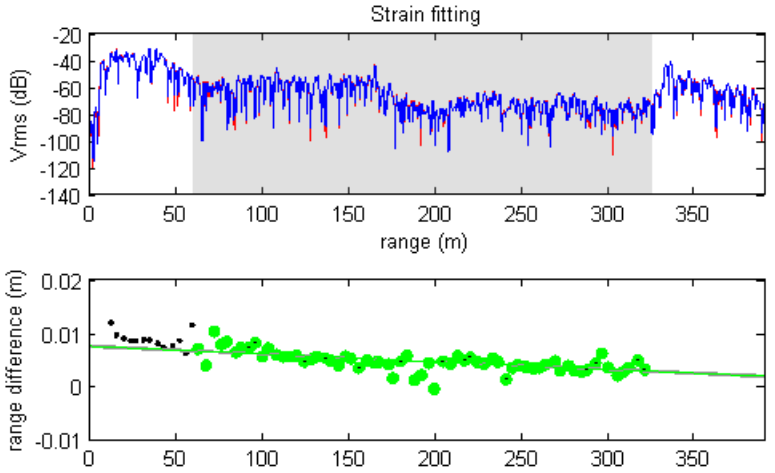
C	330-350	65-330	339.4391/ 339.4350	7.1588	-3.8183 (1.0171)	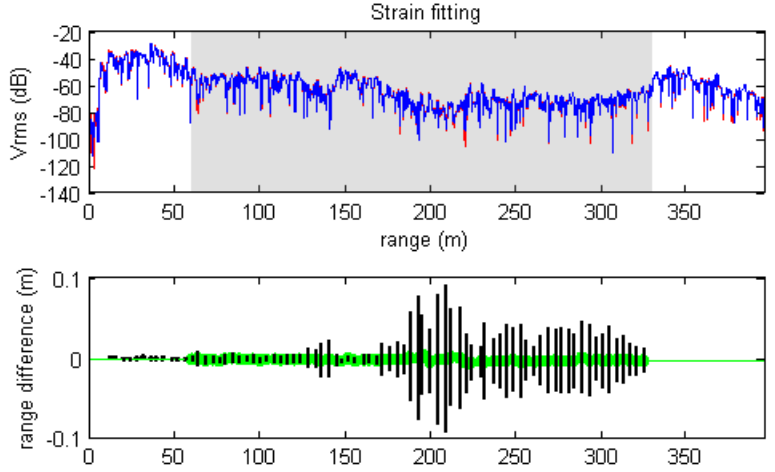

E1	310-330	65-310	326.2613/ 326.2562	7.2365	-6.4210 (2.1002)	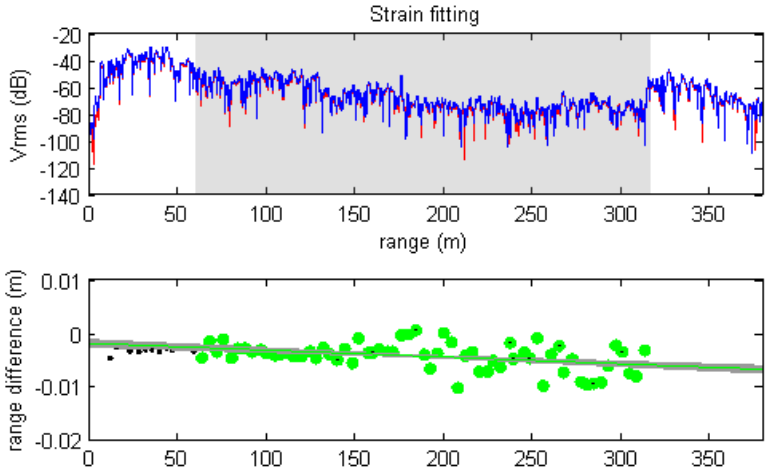
E7	330-350	65-330	345.9810/ 345.9806	7.3263	-5.9733 (1.0246)